DIFFUSION AND ION-EXCHANGE IN LOW-PERMEABILITY ROCKS: LABORATORY-BASED X-RAY METHODS

Charles Cadieux

Thesis submitted to the University of Ottawa
in partial fulfillment of the requirements for the Master of Science in Earth Sciences

Department of Earth and Environmental Sciences
Faculty of Science
University of Ottawa

PREFACE

This thesis, titled "Diffusion and ion-exchange in low-permeability rocks: laboratory-based X-ray methods", is submitted to the University of Ottawa in partial fulfillment of the requirements for the Master of Science in Earth Sciences. It is divided into 4 chapters. The first chapter is introductory; the rationale for the research is presented, an overview of the current state of knowledge is provided and the objectives and relevant concepts are defined. The next two chapters are research articles intended for publication, each on a different laboratory-based X-ray method developed to study diffusion and ion-exchange in low-permeability rocks. Chapter 2 is a study on improving an X-ray radiography method to quantify diffusion of iodide in granite. Chapter 3 is on a novel X-ray fluorescence spectroscopy method developed to study diffusion and ion-exchange of multiple solutes simultaneously in porous media. Chapter 4 is a conclusion to the thesis; principal results and their implications are summarized, and future outlook for this research topic is discussed. The appendices contain supplemental information and data that were out of the scope of the articles.

STATEMENT OF CONTRIBUTION

Conceptualisation, design of the two studies: Tom Al, Charles Cadieux, Samuel Morfin. Early testing of modified radiography method: Guadalupe Maldonado-Sànchez, S. Morfin. Further development of the radiography method and associated data acquisition: C. Cadieux, S. Morfin. Acquisition, analysis of through-diffusion data: Dominique Bower, S. Morfin. Preliminary testing of customized X-ray fluorescence (XRF) method: Birendra Sapkota, S. Morfin, C. Cadieux. Testing of XRF method and data acquisition for diffusion study: C. Cadieux, S. Morfin. Radiography and XRF diffusion data analysis and modelling: C. Cadieux. Figures and tables: C. Cadieux, T. Al. Drafts: C. Cadieux. Editing: T. Al, C. Cadieux.

ABSTRACT

Safe storage of radioactive wastes from nuclear power production represents a challenge faced by several jurisdictions. In recent decades, proposals for long-term storage into geological formations have sparked interest in solute migration through low-permeability materials. Diffusion and ion-exchange are key mechanisms that govern transport through rocks in which porewater is immobile, but there are challenges associated with studying these processes efficiently and accurately at the laboratory scale with current methods. In this research, an existing X-ray radiography technique was modified successfully to allow for the study of non-reactive tracer diffusion in a very low porosity (<0.5%), heterogenous granite from the Lac du Bonnet Batholith (Manitoba, Canada). Additionally, a novel energy-dispersive X-ray fluorescence (EDXRF) technique was developed to study simultaneous diffusion of non-reactive and reactive tracers in the Queenston Formation shale (Bruce nuclear site, Ontario, Canada). The two methods produced coherent tracer concentration profiles through the transient stage of diffusion and allowed for the successful estimation of an effective diffusion coefficient of 3.1×10^{-14} m^2/s for I in the granite and pore diffusion coefficients for I and Cs in the shale of $6.1 \pm 0.4\times10^{-11}$ m^2/s and $9.5 \pm 1.3\times10^{-11}$ m^2/s, respectively, as well as a cation exchange capacity of 1.8 ± 0.7 meq/100g and a selectivity coefficient for the exchange of Na^+ for Cs^+ of 2.3 ± 0.2 for the shale. The techniques that were developed represent additional tools for efficient, in-situ study of diffusion and ion-exchange in low-permeability rocks. There is potential for extending their scope to different applications, and surely to the study of additional tracers and materials.

ACKNOWLEDGMENTS

Several people have played a part in this journey. Their scientific, technical and moral support has been invaluable in achieving this goal. My heartfelt gratitude goes to all of you;

To Tom, for being a calm, interested and knowledgeable teacher. Your way of thinking, your way of helping, your words of encouragement and your unwavering patience throughout the years have had a strong impact on me.

À Sam, parce que deux têtes valent toujours mieux qu'une. Je n'aurais jamais pu surmonter seul tous les défis qui se sont présentés à nous au cours de ce projet. Ta passion et ta curiosité sont une réelle source d'inspiration.

To all the transient colleagues, and friends, who formed our lab group, for your help and support; Dom, Magda, Guadalupe, Birendra, Goli, Jilian, and to *Carla*, for being a beautiful, curious, and inspiring soul.

Aux employés dédiés du département et du « machine shop » pour leur aide; Lisa, Benoit et son équipe, Alain et Glenn.

À mes sœurs, mes parents, ma famille et mes amis – trop de belles personnes pour vous nommer toutes – pour vos encouragement et votre soutien inconditionnel.

À Éli et Vincent pour m'avoir tenu bonne compagnie et pour avoir abandonné un coin de la maison pendant plus d'un mois pour ma cause.

À Nick, pour m'avoir poussé, doucement, puis fermement, à écrire alors que je n'en avais plus envie; je n'en serais pas encore là sans toi.

CONTENTS

LIST OF FIGURES VIII
LIST OF TABLES X
NOTATION XI
CHAPTER 1 1
INTRODUCTION 1
1.1. BACKGROUND 1
1.1.2. Nuclear power in Canada 1
1.1.3. Deep Geological Repositories 2
1.1.4. State of knowledge overview 5
1.2. THEORETICAL FRAMEWORK 6
1.2.1. Diffusion 6
1.2.2. Reaction processes 10
1.2.3. X-rays 12
1.2.3.1. Wave theory 12
1.2.3.2. Quantum theory 12
1.2.3.3. X-ray Interactions 13
1.2.3.4. X-ray generation 14
1.2.3.5. X-ray radiography 14
1.2.3.6. Energy-dispersive X-ray fluorescence spectroscopy 15
1.3. RESEARCH OBJECTIVES 16
1.4. REFERENCES 17
CHAPTER 2 24
DIFFUSION OF IODIDE IN GRANITE: AN X-RAY RADIOGRAPHY METHOD 24
ABSTRACT 24
2.1. INTRODUCTION 25
2.1.1. Principles of X-ray radiography method 26
2.2. MATERIALS AND METHODS 29
2.2.1. Sample description 29
2.2.2. Sample preparation and characterization 30
2.2.3. Synthetic porewater and tracer solutions 31
2.2.4. Water-accessible porosity measurement 31
2.2.5. Diffusion cell design 32
2.2.6. X-ray radiography 33
2.2.7. Through-diffusion 36
2.3. RESULTS 38
2.3.1. Water-accessible porosity 38
2.3.2. Mineralogical characterization 38
2.3.3. X-ray Radiography 39
2.3.4. Through-diffusion 40
2.4. DISCUSSION 42
2.5. CONCLUSION 49
2.6. ACKNOWLEDGMENTS 49
2.7. REFERENCES 50
CHAPTER 3 56

XRF MEASUREMENT OF I AND CS DIFFUSION AND ION-EXCHANGE IN SHALE 56
ABSTRACT 56
3.1. INTRODUCTION 57
3.2. MATERIALS AND METHODS 60
3.2.1. Sample Description 60
3.2.2. Synthetic porewater and tracer solutions 61
3.2.3. Sample preparation 61
3.2.4. Mineralogy 62
3.2.5. Water-accessible porosity 62
3.2.6. Diffusion cells 63
3.2.7. Data acquisition 65
3.2.8. Calibration 66
3.2.9. Data analysis 69
3.3. RESULTS 71
3.3.1. Mineralogy 71
3.3.2. Porosity 72
3.3.3. Calibration and data Analysis 72
3.4. DISCUSSION 76
3.5. CONCLUSION 80
3.6. ACKNOWLEDGMENTS 81
3.7. REFERENCES 81
CHAPTER 4 86
CONCLUSION 86
4.1. REFERENCES 88
APPENDIX A 89
X-RAY RADIOGRAPHY DATA PROCESSING 89
A.1. INTRODUCTION 89
A.2. DATA PROCESSING 89
A.3. REFERENCES 94
APPENDIX B 95
STUDY OF DIFFUSION AND ION-EXCHANGE OF CESIUM IN GRANITE USING THE X-RAY RADIOGRAPHY METHOD 95
ABSTRACT 95
B.1. INTRODUCTION 95
B.2. METHODS 97
B.2.1. Sample description 97
B.2.2. Sample preparation and characterization 97
B.2.3. Synthetic porewater and tracer solutions 97
B.2.4. Water-accessible porosity measurement 97
B.2.5. Diffusion cell design 98
B.2.6. Data acquisition 98
B.2.7. Calibration 98
B.3. RESULTS AND DISCUSSION 100
B.3.1. Water-accessible porosity 100
B.3.2. Mineral characterization 100
B.3.3. Calibration 100

B.3.4. Cesium diffusion 102
B.4. CONCLUSION 106
B.5. REFERENCES 107
APPENDIX C 110
EDXRF INSTRUMENT PARAMETER OPTIMISATION 110
C.1. INTRODUCTION 110
C.2. RESULTS AND DISCUSSION 111
C.3. CONCLUSION 120
C.4. REFERENCES 121

LIST OF FIGURES

Fig. 1.1. Principles of X-ray fluorescence spectroscopy schematic. 16
Fig. 2.1. Schematic diagrams of the diffusion cells: top) radiography, bottom) TD. 33
Fig. 2.2. Experimental set up for acquisition of radiographic images. 34
Fig. 2.3. Schematic representation of the assembled apparatus for through-diffusion experiments. 37
Fig. 2.4. Lac du Bonnet granite thin section showing (A) plane-polarized light optical microscope image with biotite partly altered to chlorite and clay minerals in altered plagioclase, and (B) backscattered-electron image (BSE image) of pore space infilled with clay minerals. .. 39
Fig. 2.5. Relative concentration (C_x/C_0) profiles for iodide tracer in the Lac du Bonnet granite with fitted analytical solution. 40
Fig. 2.6. Flux (J_D) and mass accumulation (Q_t) data from a TD experiment with iodide in Lac du Bonnet granite, sample CS6. Error bars on the flux represent the maximum total analytical uncertainty. 41
Fig. 2.7. Flux (J_D) and mass accumulation (Q_t) data from a TD experiment with HTO in Lac du Bonnet granite, sample CS6. Error bars on the flux represent the maximum total analytical uncertainty. 41
Fig. 2.8. Data from a previous experiment without sample rotation showing the difference in X-ray attenuation ($\Delta\mu$) profiles during iodide diffusion in Lac du Bonnet Granite; Maldonado-Sánchez (2020). 44
Fig. 2.9. Comparison of D_e values from this study with those reported in the literature for I^- , Cl^- and HTO in crystalline rocks. The vertical bars with brackets represent min-max ranges, and the "x" represent averages. 47
Fig. 3. 1. Cross-section of a diffusion cell used in the experiments. 64
Fig. 3.2. Experimental XRF set up used to acquire diffusion data. 66
Fig. 3.3. Polished section of Queenston shale – [A] Optical image of the thin section (16.5 mm wide, 25.0 mm high) [B] BSE image of coarse matrix [C] Coarse matrix (higher magnification) [D] Fine matrix [E] Fine matrix (higher magnification). 72
Fig. 3.4. Spectral data in the energy region encompassing the I Kα and Cs Kα peaks for [A] the pressed pellet standards (each spectrum an average of three repeat measurements) and [B] in sample QS1 at a 7-mm distance from the influx boundary (plotted as 3-point moving averages). 73
Fig. 3.5. Calibration curves for I [A] and Cs [B] in pressed pellet standards relating X-ray intensity to the C_{pw} in the standards (+ symbols) and the scaled C_t in the samples (× symbols). 74
Fig. 3.6. Example diffusion profiles for I (A) and Cs (B) for sample QS1 at different measurement times after injection of the tracer solution. 75
Fig. 3.7. Spatial variations in ϕ_I for Queenston shale samples. 78
Fig. A1. Approximate location of the three regions of interest used for data processing on an example radiograph. 89
Fig. A2. Radiograph GSV profile (average from 3 radiographs) along the diffusion path at 5 times following iodide diffusion in sample CS2 and at time t = 0 (Ref). 90

Fig. A3. X-ray intensity (GSV) peak located in normalisation ROI [A] before normalisation and [B] after normalisation and log transformation. 91
Fig. A4. Example illustrating how a Δμ profile (in green) is obtained by subtracting the X-ray intensity (ln(GSV)) profile of a time-series (here 22h, in red) from a reference profile (in black) 92
Fig. A5: Optimized $\Delta\mu_0$ across the bottom part of the sample domain 93
Fig. B1. Cross-section of the "cup" calibration cell 99
Fig. B2. Calibration with the cup method relating difference in attenuation (Δμ) to [A] Cs C_{pw} in the standards and [B] Cs C_t in the samples. Values are averages (n=3) ± 1 S.D. error bars. 101
Fig. B3. Calibration with the pellet method relating difference in attenuation (Δμ) to [A] Cs C_{pw} in the standards and [B] Cs C_t in the samples. 101
Fig. B4. Calibration with the cup method relating difference in attenuation (Δμ) to [A] I C_{pw} in the standards and [B] I C_t in the samples. Values are averages (n=3) ± 1 S.D. error bars. 102
Fig. B5. Experimental (symbols) and modelled (lines) diffusion profiles for Cs at different measurement times after tracer injection based on the cup calibration. 103
Fig. B6. Estimated parameters (D_p, CEC, $\log k_{Na\_Cs}$) for Cs based on based-fit modelled diffusion profiles at different measurement times after tracer injection based on the cup calibration. 104
Fig. B7. Experimental diffusion profiles for Cs at different measurement times after tracer injection based on the pellet calibration. Profiles are an average (n=3) and dashed lines represent ± 1σ. 105
Fig. B8. Experimental diffusion profiles for I at different measurement times after tracer injection based on the cup calibration with previous best-fit modelled curves from Chapter 2. 106
Fig. C1. Change in I-Kα and Cs-Kα peak intensity and relative error on the intensity with voltage. 112
Fig. C2. Relative error on intensity as a function of peak intensity for Cs and I. 112
Fig. C3. Cs-Kα peak intensity and relative error on the intensity as a function of source current. 113
Fig. C4. Cs-Kα net peak area and relative error on intensity as a function of acquisition time. 114
Fig. C5. [A] Real and [B] schematic view of the relative position of the sample, detector and collimator used in the XRF diffusion experiments. 115
Fig. C6. Cs-Kα peak total count measured at 40-second intervals to evaluate source stability 116
Fig. C7. Spectral data in the energy region encompassing the I-Kα and Cs-Kα peaks acquired while using different Cu filter thicknesses and signal processing methods (plotted as 3-point moving averages). 117
Fig. C9. Net area of Cu-kα peak across the edge of a strip of copper. 118
Fig. C10. Mo-Kα and Ba-Kα peak intensity across the edge of the stainless steel ring placed at the bottom of the sample. The chosen first step for diffusion data acquisition is indicated by the red bar. 119
Fig. C11: Change in $\Sigma(e_i^2)$ as a function of x_1 value at three different D_p. 120

LIST OF TABLES

Table 2.1. Glossary of diffusion terms 28
Table 2.2. Composition of synthetic porewater and iodide tracer solution (mmol/kgw)..... 31
Table 2.3. Results obtained from the ϕ_w measurements..... 38
Table 2.4. Summary of diffusion-coefficient and rock-capacity-factor measurements for iodide and HTO (α_I and α_{HTO}) obtained by the TD method..... 42
Table 2.5. Compilation of ϕ_w and D_e values reported in the literature for I^- , Cl^- and HTO in crystalline rocks. 46
Table 3.1. Composition of SPW and tracer solutions (mol/L) used in XRF diffusion experiments. 61
Table 3.2. Results obtained from the porosity measurements..... 72
Table 3.3. Summary of D_{p_I} , D_{p_Cs}, CEC and $\log k_{Na\_Cs}$ in Queenston shale 76
Table 3.4. Average ϕ_I in Queenston shale samples. 78
Table 3.5. Compilation of ϕ_w , ϕ_I , ϕ_I/ϕ_w and D_{p-I} values reported in the literature..... 80
Table B1. Composition of synthetic porewater and cesium tracer solution (mmol/kgw)..... 97
Table B2. Summary of estimated parameters (D_p, CEC, $\log k_{Na\_Cs}$) for Cs based based on the cup calibration method. 104

NOTATION

$^{2}H_2O$	Deuterium water
$^{3}H_2O$	Tritiated water (HTO)
^{235}U	Uranium isotope enriched for use in nuclear reactors
^{238}U	Most naturally abundant and stable uranium isotope
BSE	Backscattered electron
C_0	Initial concentration, or solute concentration at the influx boundary (x = 0)
c	Speed of light
C	Solute concentration
CANDU	Canada Deuterium Uranium Reactor
CEC	Cation exchange coefficient
C_m	Modelled solute concentration
CPS	Counts per second
C_{pw}	Porewater-equivalent tracer concentration in standard
C_t	Equivalent aqueous tracer concentration in sample
CT	Computer tomography
C_x/C_0	Relative tracer concentration in the sample
D_0	Free-water diffusion coefficient
d	Diameter or; Material layer thickness
D	Diffusion coefficient or diffusivity
DPP	Digital pulse processing
DGR	Deep geological repository
D_a	Apparent diffusion coefficient
D_e	Effective diffusion coefficient
D_p	Pore diffusion coefficient
E	Photon energy
EDS	Energy-dispersive X-ray spectroscopy
EDXRF	Energy-dispersive X-ray fluorescence spectroscopy
ER	Edge response
erfc	Complementary error function
ESR	Effective spatial resolution
FPS	Frames per second
GSV	Grayscale value
H	Planck's constant
HTO	Tritiated water ($^{3}H_2O$)
I_0	Intensity of incident photon beam
I	Intensity of attenuated photon beam or; Electrical current intensity
ICP-MS	Inductively coupled plasma mass spectrometry
Int	X-ray fluorescence intensity
I_{ref}	Intensity of X-rays transmitted through the sample at time t = 0
I_t	Intensity of X-rays transmitted through the sample at time t > 0
J_d	Diffusive mass flux
J	Mass flux

k	Boltzmann's constant
K	Mass action constant or; Hydraulic conductivity
Kα	Characteristic energy of photon emitted from L- to K-shell electron transition
K_d	Distribution coefficient
kgw	Kilogram of water (kg H_2O)
L	Shortest distance between diffusion boundaries (sample length)
L_e	Effective solute transport path length within a porous medium
Logk	Selectivity coefficient
LSC	Liquid scintillation counting
Max	Maximum GSV
m_{dry}	Dry mass
m_g	Mass of grains
m_{sat}	Saturated mass
m_{sub}	Submerged mass
NEA	Nuclear Energy Agency
N_f	Normalisation factor
n_t	Number of moles of tracer
NWMO	Nuclear Waste Management Organization
OPG	Ontario Power Generation
P	Electrical power
Q_t	Accumulated tracer mass at time t in the low concentration reservoir
r	Particle radius
R_f	Retardation factor
ROI	Region of interest
RSD	Relative standard deviation
RTD	Rise time discrimination
S	Cross-section area of a sample or; Mass of solute sorbed
SEM	Scanning electron microscope
SNR	Signal-to-noise ratio
SPW	Synthetic porewater
t	Time
T	Temperature
TD	Through-diffusion
UFC	Used fuel container
UO_2	Uranium oxide
USGS	United States Geological Survey
V	Electrical potential difference (voltage)
V_I	X-ray interaction volume
V_{rock}	Bulk sample volume
V_s	Volume of standard
V_{voids}	Volume of voids
w_{SPW}	Mass fraction of solutes in synthetic porewater
x	Distance
XRF	X-ray fluorescence

GREEK CHARACTERS

α	Rock capacity factor
δ	Constrictivity
$\Delta\mu$	Change in linear attenuation
$\Delta\mu_0$	Change in linear attenuation at the influx boundary
ϕ_I	Iodide-accessible porosity
ϕ_s	Porosity of standard
ϕ_t	Solute specific porosity
ϕ_w	Water-accessible porosity
γ	Gamma ray
η	Dynamic viscosity
λ	Wavelength
μ	Linear attenuation coefficient
μ/ρ	mass attenuation coefficient
θ	Volumetric water content
ρ	Bulk density
ρ_g	Grain density
ρ_{SPW}	Density of synthetic porewater
σ	Standard deviation
$\Sigma(e_i^2)$	Sum of the square of the error
τ	Tortuosity
τ_f	Tortuosity factor

CHAPTER 1

INTRODUCTION

1.1. Background

1.1.1. Nuclear power in Canada

Conventional carbon-based energy production is an important source of anthropogenic greenhouse gas emissions contributing to global warming (Baird & Cann, 2012). Resulting social and economic impacts have brought climate change into the political discourse, driving the progression towards low-emission energy supplies. Nuclear fission has been used as a reliable energy source since the 1950's, following World War II. Nuclear reactors work by harnessing energy from induced radioactive decay. There are four main components to a reactor: fuel, a moderator, coolant, and control rods (Chaplin, 2014b). The fuel is a fissile material, or a radioactive material whose decay can be induced by a neutron. The moderator reduces the kinetic energy of the neutrons so that they can more readily induce fission of the fuel. The coolant circulates in the reactor and absorbs the heat from the fuel's decay, and the control rods absorb excess neutrons to slow down the fission chain reaction (Chaplin, 2014b).

Canada developed its own type of pressurized heavy-water reactor technology, the Canada Deuterium Uranium (CANDU) reactor. In CANDU reactors, deuterium water (^2H_2O) is used as a coolant and moderator, and natural uranium oxide (UO_2) is used as fuel. Natural uranium contains 0.7% of ^{235}U, a fissile isotope which can sustain neutron-induced fission chain reactions (Katz & Rabinowitch, 1951). The rest is made up of ^{238}U, which decays spontaneously at a very low rate. The fuel used in reactors consists of uranium dioxide (ceramic) pellets lined up in 0.5-m rods called "fuel elements", arranged in 28-, 37- or 43-element bundles. For a chain reaction to occur in the fuel, a critical mass of ^{235}U must be present in close proximity inside of

the reactor. Therefore, CANDU reactor cores house up to 7200 fuel bundles (37-element CANDU 9 design; Chaplin, 2014a) and contain up to 135,000 kg of uranium in total. Each fuel bundle has a lifespan of 12-18 months (Allan & Dormuth, 2001). The first CANDU reactor began operations in 1971, and as of 2023, there were 19 operable and 3 defunct reactors in Canada. Over time, Canada's used fuel inventory has grown to about 3.3 million bundles in 2023; a number projected to reach 5.6 million by the end of current (2023) reactor's lifetimes (Reily, 2023; Gobien & Ion, 2019; Heckman & Edward, 2020).

In a technical report produced for the NWMO, Heckman and Edward (2020) provide an inventory of important radionuclides contained in used nuclear fuel stored in Canada. This inventory is based on previous reference CANDU fuel calculations from a report by Ontario Power Generation (Tait et al., 2000). Whereas it starts as UO_2 pellets in Zircaloy cladding, by the end of its useful life, the fuel contains dozens of dose-contributing radioactive isotopes (actinides, fission products, neutron-activated impurities), in various quantities and with half-lives ranging from a few minutes to several million years (Heckman & Edward, 2020; Choi et al., 1999).

1.1.2. Deep Geological Repositories

Geological repositories are proposed by several countries to safely isolate wastes for long periods of time (NEA, 2008). Geological repositories consist of chambers carved in a geological formation in which wastes are placed and isolated with an engineered barrier system. Canada is working toward a plan for a geological waste repository in either crystalline or sedimentary rocks which would consist of chambers carved in the geological formation up to 500 m deep and connected to the surface through an access shaft and a ventilation shaft. During the operation of the repository, workers would load the chambers with the fuel bundles and monitor the site. This

operation would last approximately 70 years, after which the repository would be sealed by filling the shafts with various materials including concrete and bentonite. Monitoring of the repository would continue from the surface (Noronha, 2016).

There are two main engineered barriers isolating the used fuel in the proposed DGR. Used fuel containers (UFC) consist of a steel core covered with a layer of copper and can hold 48 used fuel bundles (Noronha, 2016). The steel core provides structural strength whereas the copper coating provides corrosion resistance. There are several recent studies investigating copper's corrosion resistance under conditions similar to those that would be found in a DGR (Noronha, 2016; Scully et al., 2016; Rashwan et al., 2022; Hall et al., 2021; Shrestha et al., 2021; King et al., 2017). The second engineered barrier is the bentonite buffer layer in which each UFC will be encased. This thick bentonite buffer provides a low permeability layer able to slow migration of solutes in the event of a failure of the UFC. There are numerous studies investigating fluid migration in bentonite as well as its swelling behaviour under the influence of heat generated by radioactive decay, porewater salinity, microbial activity, temperature and compaction (Acikel et al., 2019; Brachman et al., 2021; Briggs et al. 2017; Li et al., 2020; Graupner et al., 2018; Abootalebi & siemens, 2018; Idemitsu et al., 2016; Van Loon et al., 2007).

The geological formation hosting the repository acts as a third, natural barrier against radionuclide migration. In the event of failure or degradation of the engineered barriers, the geological formation should be capable of considerably slowing down the transport of solubilized radioisotopes because the level of radioactivity of the isolated spent nuclear fuel is expected to exceed natural uranium decay levels for at least one million years (Shoesmith, 2013). A suitable geological formation to host the repository would be elastic, isotropic, homogeneous, with a low permeability and minimal fractures (Noronha, 2016).

Intrusive igneous rocks typically have a low porosity, which results in poor pore connectivity and very low permeability. Therefore, intact crystalline rock formations are good candidates for a deep geological repository as they offer an impermeable barrier against solute migration. In Canada, Sweden and Finland, where Precambrian crystalline bedrock is extensive, transport properties of granites and diorite have been studied for nuclear waste storage purposes (eg. Canada : Vilks et al., 2003; Spiessl et al., 2008; Xiang et al., 2016b; Zheng et al., 2024; Sweden : Johansson et al., 1998; Widestrand et al., 2007; Schmeide et al., 2014; Finland : Muuri et al., 2016, 2017, 2018).

Sedimentary rock formations are often considered as potential hosts for a DGR. More specifically, clay-rich rocks such as Opalinus Clay (Van Loon et al., 2003; Wersin et al., 2004; Bossart et al., 2017), Callovo-Oxfordian Argillites (Melkior et al., 2004), Boom Clay (Henrion et al., 1985) and Upper-Ordovician shale and limestones (Cavé et al., 2009; Clark et al. 2013; Al et al., 2015) are of interest due to their low hydraulic conductivity and the capacity of ductile, clay-rich formations for self-healing of fractures (Urpi et al., 2019). Additionally, clay rocks typically have a high sorption capacity which slows the transport of positively charged solutes, making them ideal for long-term storage of radioactive waste (Van Loon & Mibus, 2015).

It is critical to understand the transport and reaction processes affecting solutes of interest in porous media to evaluate the suitability of geological formations for potential containment of radioactive elements. Specifically, the study of *diffusion* and *ion-exchange* is of interest, and the subject of this thesis, because those are the main processes controlling the concentration of solutes within low-porosity geological materials (Loomer et al., 2013).

1.1.3. State of knowledge overview

At the laboratory scale, matrix diffusion is commonly studied by measuring the flux of tracer through a sample during steady-state diffusion, a technique known as through-diffusion (TD). Conservative, or nonreactive tracers such as tritiated water (HTO) or anions (Cl^-, Br^-, I^-) are commonly used as they allow determination of diffusion coefficients that reflect the rock properties; primarily the pore-size distribution, pore connectivity and total pore volume. Conservative solute diffusion in sedimentary rocks is well documented (Boving and Grathwohl, 2001; Van Loon et al., 2003; Vilks & Miller, 2007; Descostes et al., 2008; Cavé et al., 2009; Xiang et al., 2013, 2016a). In conducting these experiments, it takes time (weeks to years) to reach a steady-state diffusion flux, particularly for reactive tracers that display relatively slow rates of transport (retardation) due to sequestration of solutes on the surface of mineral solids by processes such as ion exchange and mineral precipitation. Faster experimental outcomes can be achieved by monitoring tracer migration in a sample during the early transient-period of diffusion, a technique known as in-diffusion. This is commonly done with non-destructive measurement techniques such as autoradiography (Johansson et al., 1998; Lee et al., 2012), radiography (Tidwell et al. 2000; Cavé et al., 2009; Nunn et al., 2018), γ-spectroscopy (Idemitsu et al., 1992; Widestrand et al., 2007; Muuri et al., 2018) and X-ray CT (Nakashima, 2000; Agbogun et al., 2013). However, such studies in intact crystalline rocks are lacking, likely due to the added complexity of acquiring spatial distributions of tracer concentration in heterogeneous material of very low porosity. For example, Maldonado-Sànchez (2020) tested the X-ray Radiography method to study diffusion of iodide in intact granite and found that large image registration errors due to heterogeneous mineral distributions in the rock led to low signal-to-noise ratios (SNR) and an inability to distinguish the signal from the diffusing tracer.

Knowledge of the retardation effect from reactive tracers is critical for a complete understanding of radionuclide transport in rocks. Reactions such as ion-exchange are commonly studied independently from diffusive transport using batch experiments where a known mass of disaggregated rock powder is mixed with tracer solutions of varying initial concentration to estimate the distribution coefficient (K_d) of the adsorbing tracer species. For a simple linear isotherm (Eq. 1.1), the mass of solute sorbed (S) is a linear function of the initial solute concentration (C) with a slope equal to K_d:

$$S = K_d \cdot C \qquad [1.1]$$

These batch sorption experiments are used to quantify the affinity of reactive tracers (e.g. cations such as Cs^+) with the rock powder or with single minerals (Poinssot et al., 1999; Bostick et al., 2002; Van Loon et al., 2005; Fuller et al., 2015; Muuri et al., 2016). However, disaggregation of rocks creates significant new mineral surface area compared to that exposed in the pores of intact rocks, so sorption studies on intact rocks are of interest because the experimental conditions are closer to in situ conditions and can therefore yield more representative results. Loomer et al. (2013) used the X-ray radiography method (Cavé et al., 2009) in conjunction with multicomponent reactive transport modelling to study the diffusion and sorption of Cs^+ in intact shale. However, it's not possible to study diffusion of multiple tracers simultaneously with the radiography method.

1.2. Theoretical framework

1.2.1. Diffusion

The transport of solutes in porous geologic media is generally controlled by three main processes: advection, mechanical dispersion and molecular diffusion. Advection is the transport

of solutes with flowing groundwater. Mechanical dispersion is the gradual spreading of solutes that occurs due to velocity variations that exist along different flow paths in the pore space. Both of these processes are dependent on the flow of groundwater. In porous media where porewater is immobile due to poor pore connectivity, small pore size or low hydraulic gradient, molecular diffusion is the dominant mode of solute transport (Boving and Grathwohl, 2001; Spiessl et al., 2008; Agbogun et al., 2013).

Molecular diffusion in a groundwater context is the molecular-scale random movement (Brownian motion) of solutes (dissolved ions or molecules) in water, that at the macro scale results in migration of solutes from regions of high concentration to regions of low concentration. The collective motion of an infinite number of particles is analogous to thermal conduction in solids and is represented by Fick's law of diffusion (Narasimhan, 1999).

Fick's first law (Eq. 1.2) states that the flux of diffusing solute is proportional to the solute concentration gradient scaled by a constant:

$$J_i = -D \cdot \frac{\partial C}{\partial x_i} \qquad [1.2]$$

where J_i is the diffusing mass flux ($kg \cdot m^{-2} \cdot s^{-1}$), C is the concentration of diffusing solute in water ($kg \cdot m^{-3}$) over a distance x (m) along the diffusion direction i, $\partial C/\partial x$ is the concentration gradient along i, and the constant D is the diffusion coefficient, or diffusivity ($m^2 \cdot s^{-1}$). This law is valid for ideal, steady-state conditions; systems for which D is constant and $\partial C/\partial x$ does not change in time. However, steady-state conditions are rarely attained given the constant fluctuations in natural systems.

Fick's second law of diffusion applies to non-steady-state (transient) systems; it relates the change in solute concentration with time t (s) in a unit volume of porous media to the

variable flux of solute into the volume. Equation 1.3 is a simplified form describing Fick's second law for diffusion in one dimension:

$$\frac{\partial C}{\partial t} = -D \cdot \frac{\partial^2 C}{\partial x^2} \quad [1.3]$$

For a specific solute in a bulk liquid solvent, the diffusion coefficient is a function of the diffusing solute radius, the temperature, and the viscosity of the fluid in which the solute is moving, and can be approximated by the Stokes-Einstein-Sutherland equation (1.4):

$$D = \frac{kT}{6\pi r\eta} \quad [1.4]$$

where k is Boltzmann's constant ($J \cdot K^{-1}$), T is the temperature (K), r is the solute radius (m) and η is the dynamic viscosity of the solvent (Pa·s). This relationship is only valid in infinite dilution conditions for large spherical particles; it breaks down at the molecular scale (Costigliola et al., 2019; Baer et al., 2024) and D generally has to be determined experimentally when studying natural systems.

For a solute diffusing in a liquid contained in a porous medium, such as in groundwater, the diffusion coefficient is lower than the diffusion coefficient in pure water, taking into account the 3-dimensional geometry of the pore space (1.5):

$$D_p = D_0 \cdot \frac{\delta}{\tau} \quad [1.5]$$

or

$$D_p = D_0 \cdot \tau_f \quad [1.5.1]$$

where D_p is the pore diffusion coefficient ($m^2 \cdot s^{-1}$), D_0 is the free-water diffusion coefficient ($m^2 \cdot s^{-1}$), δ is the constrictivity, τ is the tortuosity and τ_f is the tortuosity factor ($0 < \tau_f \leq 1$), a common term grouping δ and τ.

Fick's second law can be solved for different geometries (boundary conditions). For example, the following analytical solution (Eq. 1.6) (Crank, 1975) can be used:

$$C_i(x,t) = C_0 \, erfc \frac{x}{\sqrt{D_p t}} \quad [1.6]$$

given the boundary conditions:

$$C(x,t) = 0 \begin{cases} t = 0 \\ x > 0 \end{cases}$$

$$C(x,t) = C_0 \begin{cases} t \geq 0 \\ x = 0 \end{cases}$$

$$C(x,t) = 0 \begin{cases} t \geq 0 \\ x = L \end{cases}$$

where C_i is the solute concentration ($mol \cdot L^{-1}$) at distance x and time t, C_0 is the constant solute concentration at the influx boundary ($mol \cdot L^{-1}$), erfc is the complementary error function, and L is the length of the domain of interest for diffusion (m).

The effective diffusion coefficient (D_e) is used to account for the reduced water volume available for diffusion in a porous medium (Eq. 1.7):

$$D_e = D_p \cdot \phi_t \quad [1.7]$$

where ϕ_t is the solute-specific porosity.

1.2.2. Reaction processes

For certain solutes, reaction processes at the solid-water interface also have to be considered when describing transport. For reactive tracers, the apparent diffusion coefficient (D_a) is sometimes used (Eq. 1.8):

$$D_a = \frac{D_p}{R_f} \quad [1.8]$$

where R_f is the retardation factor that accounts for the decrease in the diffusion transport rate due to the loss of tracer mass from the water as it reacts with the porous medium (Eq. 1.9):

$$R_f = 1 + \frac{\rho}{\theta} \cdot K_d \quad [1.9]$$

where ρ is the bulk density ($g \cdot cm^{-3}$) , θ is the volumetric water content and K_d is the partition coefficient (determined by batch sorption experiments).

Mineral surfaces generally possess an electrostatic charge which can be due to deprotonation and protonation reactions or mineral lattice imperfections and elemental substitutions that result in a net charge (Stumm, 1992). In solution, the surface charge is balanced by ions that accumulate at or near the charged mineral surface - a process called *physical adsorption*. The zone extending from the mineral surface in which the surface charge is balanced by accumulating ions (cations or anions) is called the *diffuse layer*.

Ions associated with the mineral surfaces can be desorbed and replaced by ions in solution depending on their relative affinity with the solid phase and their relative solubility in the liquid phase in a process called *ion-exchange*. The equilibrium of these exchange reactions

(Eq. 1.10) can be described with regular mass action expressions (Eq. 1.10.1) (Stumm, 1992; Appelo & Postma, 2004):

$$A + B\text{-}X \rightarrow A\text{-}X + B \quad [1.9]$$

$$K_{A/B} = \frac{[A\text{-}X][B]}{[B\text{-}X][A]} \quad [1.9.1]$$

where $K_{A/B}$ is the equilibrium constant for the exchange reaction, A-X and B-X are ions on exchange sites at the solid surface, A and B are exchangeable monovalent cations. Activities are denoted by the square brackets. Unlike ions in solution, there is no way to determine the activity of ions on exchange sites, so it is not possible to define a true thermodynamic equilibrium constant, as in Eq. 1.9. Instead, an ion-exchange *selectivity coefficient* ($\log k_{A/B}$) can be defined with the activity of ions on exchange sites approximated by their equivalent fraction (Gaines-Thomas approximation; Parkhurst & Appelo, 2013). Equation 1.9 describes the tendency of a solute, A, in solution to replace an adsorbed species, B, on the mineral surface. Because Na^+ is typically abundant in saline waters such as in the Michigan Basin, it is expected to dominate the adsorption sites at the solid-water interface. Hence, it is common to report the selectivity coefficient for the exchange of Na^+ by various cations of interest to quantify the relative adsorption tendency of different species.

The amount of cations adsorbed onto mineral surfaces that are available for exchange with a species in solution is called the *cation exchange capacity* (CEC) and is typically expressed in moles (equivalents) of exchangeable cations per mass of solid. The CEC is a function of the mineral structure, its specific surface area in contact with water and its net surface charge, which is usually dependant on pH (Appelo & Postma, 2004).

1.2.3. X-rays

1.2.3.1. Wave theory

In classical physics, X-rays are defined as electromagnetic radiation comprised of an electric and a magnetic field that oscillate perpendicular to each other (Martz et al., 2016) and propagate normal to their oscillation at the speed of light (in a vacuum). X-rays are on the high-energy end of the electromagnetic spectrum, relative to, say, radio waves, visible light or infrared radiation. Their short wavelengths, which are usually measured in A (10^{-10} m) (Morelhão, 2016) correlate to their high energy through the Planck-Einstein relation (Eq. 1.11):

$$E = \frac{hc}{\lambda} \qquad [1.11]$$

where E is the photon energy (J), h is Planck's constant (J·s), c is the speed of light ($m \cdot s^{-1}$) and λ is the radiation wavelength (m).

1.2.3.2. Quantum theory

Quantum theory describes the particulate nature of electromagnetic radiation; treating light as a beam of photons (Morelhão, 2016), or indivisible packets of energy called quanta. The quantum model defines the state of an electron around the atom with four quantum numbers: n, ℓ, m_ℓ and m_s (Zschornack, 2007). The principal quantum number "n" gives information about the main shell in which the electron is located. The subshell of the electron is described by the azimuthal quantum number "ℓ" , which gives information about the orbital angular momentum of the electron. The magnetic quantum number "m_ℓ" gives information about the projection/orientation of the orbital. Finally, the spin quantum number "m_s" has two possible values, +½ and -½ for each orbital orientation (m_ℓ) (Zschornack, 2007).

Due to the discrete nature of the atom, an electron can only have certain discrete energy values, which are determined by the quantum states (the possible combinations of shell, subshell, angular momentum and spin) (Zschornack, 2007). The Pauli exclusion principle states that no two electrons in the same atom can have the same energy level.

1.2.3.3. X-ray Interactions

Photons can be annihilated or created by interacting with matter. Photoelectric absorption is an important type of interaction during which a lower-shell electron is ejected from an atom after absorbing the energy of a photon (Buzug, 2008). Photoelectric absorption can happen when the energy of the impinging photon is higher than the binding energy of the electron (Zschornack, 2007). During this process, an outer-shell electron will decrease in energy to fill the gap left by the ejected electron. Excess energy from the outer-shell electron is released radiatively in the form of a photon with an energy equal to the difference between the outer- and inner-shell electron's respective energy. This radiative release of energy is called fluorescence. Fluorescence releases characteristic X-rays, because the difference in energy between the different electronic transitions, and therefore the energy of fluorescence photons, is singular to each element. Pair production is another X-ray absorption mechanism that is more important for X-rays of higher energy (Buzug, 2008).

Additionally, interaction with matter can lead to diffraction or scattering of X-ray radiation. There are two types of scattering: elastic and inelastic. Rayleigh scattering or coherent scattering, is a type of elastic scattering during which an impinging photon is diffracted (changes direction) without losing significant energy (Buzug, 2008). Compton scattering or incoherent scattering is a type of inelastic scattering during which a photon loses part of its energy to the

ejection of an outer-shell electron. The diffracted photon has an energy equal to the difference between the initial photon energy and the binding energy of the electron (Buzug, 2008).

1.2.3.4. X-ray generation

X-rays can be produced by the acceleration or deceleration of charged particles (Martz et al., 2016). In a typical X-ray tube, a cathode (often a tungsten filament) is heated to generate electrons by thermionic emission, which are directed to a target anode (often an angled piece of tungsten) (Poludniowski et al., 2022). The high electric potential between the cathode and anode directs the electrons towards the cathode and, as they penetrate the target, they collide with its atoms and decelerate, emitting X-ray radiation called “Bremsstrahlung”, or braking radiation. Each bremsstrahlung photon has an energy equal to the loss of kinetic energy of the electron that produced it (Poludniowski et al., 2022). This results in a continuous spectrum of photon energies, or a polychromatic X-ray beam. Increasing the electric potential (voltage) between the cathode and the anode increases the kinetic energy of the electrons, resulting in photons of higher maximum energy, whereas a higher current (more electrons) results in a higher X-ray beam intensity as more photons are being produced. The X-ray beam can be “hardened” by filtering with materials such as aluminium or copper to remove low-energy X-rays from the beam.

1.2.3.5. X-ray radiography

X-ray radiography is an imaging technique wherein the sample is placed between an X-ray source and an imaging detector to produce a radiograph, or X-ray image of the sample. Any matter placed in the beam path can result in absorption or diffraction of X-rays, leading to attenuation of the beam intensity. Attenuation is highest for low energy X-rays going through denser material composed of high-atomic number elements. In the simplified case of a

monochromatic beam of X-rays of initial intensity (I_0) going through a layer of thickness *d* of a singe element with an attenuation coefficient μ, the attenuated beam intensity (I) is given by the Beer-Lambert law (Eq. 1.12):

$$I = I_0 e^{-\mu d} \quad [1.12]$$

For a multi-element material (Eq. 1.12.1), attenuation coefficients and thicknesses add up such that:

$$I = I_0 \cdot e^{-\sum_i (\mu_i d_i)} \quad [1.12.1]$$

A detector is used to measure the intensity of the X-rays that are transmitted through the sample. Flat panel detectors (rather than photographic film) are now commonly used in X-ray radiography. These digital detectors consist of a 2-dimensional array of cells that each contain a scintillator element (commonly CsI), which produces light when X-rays collide with it. A photosensitive diode (commonly amorphous Si) underneath reacts with the light and produces an electrical signal which is converted to a digital signal that is recorded as an X-ray event. Each cell represents a pixel of the final radiograph image, and each X-ray event that gets registered during the set exposure time increases the gray scale value (GSV) of a pixel. The result is a two-dimensional GSV image of the sample, where highly attenuating features present in the sample appear darker, and less attenuating features appear lighter.

1.2.3.6. Energy-dispersive X-ray fluorescence spectroscopy

X-ray fluorescence spectroscopy is a technique that makes use of a semiconductor radiation detector to measure the number and energy of the fluorescence X-rays produced when a sample is hit with an X-ray beam. Semi-conductor detectors (also called solid state detectors) contain a semi-conductor material (commonly Si) that is ionized by incident X-rays and builds

up an electric charge proportional to each incident X-ray energy. The electric charge is converted to a digital signal and counted to produce a spectrum of the total number of X-ray events recorded as a function of their energy. Characteristic X-ray energy peaks appear based on the elemental composition of the target (Fig. 2). The intensity of the characteristic peaks is proportional to the amount of each corresponding element contained in the sample. With the use of a proper calibration, spectral data can be interpreted to determine the concentration of different elements in a sample.

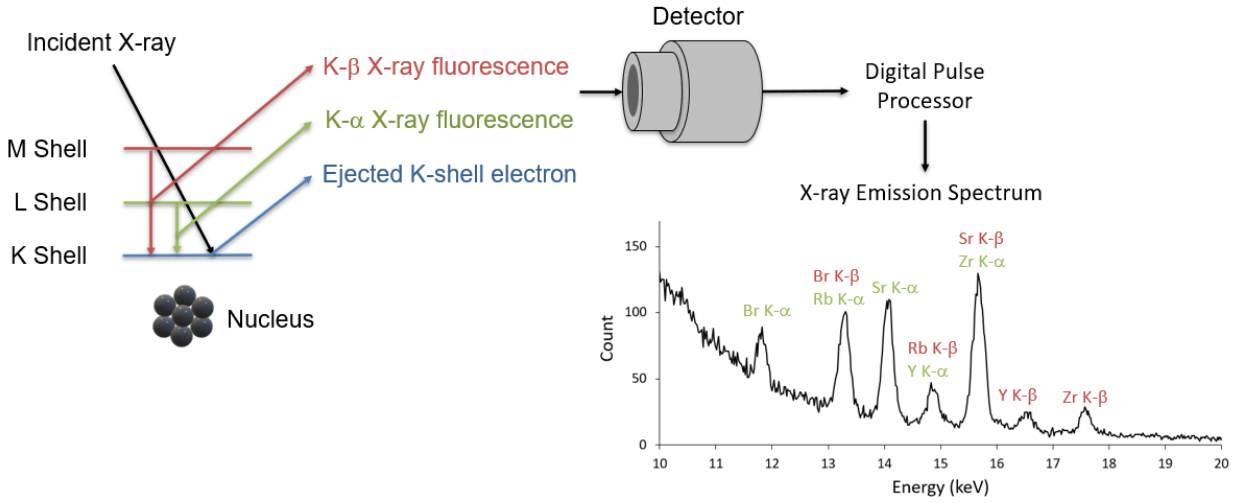

Fig. 1.1. Principles of X-ray fluorescence spectroscopy schematic.

1.3. Research Objectives

The objectives of this research are to:

- Modify the X-ray radiography technique described by Cavé et al. (2009) to minimize sensitivity to image registration errors
- Test the modified X-ray radiography technique to estimate the pore diffusion coefficient (D_p) of intact granite samples.
- Compare the results from radiography against measurements conducted by TD.

- Develop a customized X-Ray fluorescence (XRF) instrument set up to acquire concentration profiles of solutes in intact low porosity media, including a calibration method that can be used for reactive tracers.
- Apply the XRF method to estimate simultaneous diffusion coefficients for iodide and cesium in shale samples.
- Obtain in-situ estimates of cesium ion-exchange properties for the shale samples.

1.4. References

Abootalebi, P., & Siemens, G. (2018). Thermal properties of engineered barriers for a Canadian deep geological repository. *Canadian Geotechnical Journal*, *55*(6), 759-776. https://doi.org/10.1139/cgj-2017-0150

Acikel, A. S., Rowe, R. K., Brachman, R. W. I., Baral, A., & Su, G. (2019). The impact of multi-component hypersaline wetting on soluble and exchangeable cations and water retention behaviour of MX80 bentonite. *Applied Clay Science*, *180*, Article 105174. https://doi.org/10.1016/j.clay.2019.105174

Agbogun, H. M. D., Al, T. A., & Hussein, E. M. (2013). Three-dimensional imaging of porosity and tracer concentration distributions in a dolostone sample during diffusion experiments using X-ray micro-CT. *Journal of contaminant hydrology*, *145*, 44-53. https://doi.org/10.1016/j.jconhyd.2012.11.008

Al, T. A., Clark, I. D., Kennell, L., Jensen, M., & Raven, K. G. (2015). Geochemical evolution and residence time of porewater in low-permeability rocks of the Michigan Basin, Southwest Ontario. *Chemical Geology*, *404*, 1-17. https://doi.org/10.1016/j.chemgeo.2015.03.005

Allan, C.J., & Dormuth, K.W. (2001). The back end of the fuel cycle and CANDU (IAEA-CSP-6/C). International Atomic Energy Agency (IAEA)

Appelo, C. A. J., & Postma, D. (2004). *Geochemistry, groundwater and pollution*. CRC press. https://doi.org/10.1201/9781439833544

Baer, A., Wawra, S. E., Bielmeier, K., Uttinger, M. J., Smith, D. M., Peukert, W., ... & Smith, A. S. (2024). The Stokes–Einstein–Sutherland Equation at the Nanoscale Revisited. *Small*, *20*(6), Article 2304670. https://doi.org/10.1002/smll.202304670

Bossart, P., Jaeggi, D., & Nussbaum, C. (2017). Experiments on thermo-hydro-mechanical behaviour of Opalinus Clay at Mont Terri rock laboratory, Switzerland. *Journal of Rock*

Mechanics and Geotechnical Engineering, *9*(3), 502-510. https://doi.org/10.1016/j.jrmge.2016.11.014

Bostick, B. C., Vairavamurthy, M. A., Karthikeyan, K. G., & Chorover, J. (2002). Cesium adsorption on clay minerals: An EXAFS spectroscopic investigation. *Environmental Science & Technology*, *36*(12), 2670-2676. https://doi.org/10.1021/es0156892

Boving, T. B., & Grathwohl, P. (2001). Tracer diffusion coefficients in sedimentary rocks: correlation to porosity and hydraulic conductivity. *Journal of Contaminant Hydrology*, *53*(1-2), 85-100. https://doi.org/10.1016/S0169-7722(01)00138-3

Brachman, R. W., Rowe, R. K., Baral, A., Hosney, M. S., Su, G., Nguyen, T. S., ... & Lange, K. (2021). Bentonite swelling characteristics with a hypersaline multi-component pore fluid. *Canadian Geotechnical Journal*, *58*(3), 367-376. https://doi.org/10.1139/cgj-2019-0558

Briggs, S., McKelvie, J., Sleep, B., & Krol, M. (2017). Multi-dimensional transport modelling of corrosive agents through a bentonite buffer in a Canadian deep geological repository. *Science of The Total Environment*, *599*, 348-354. https://doi.org/10.1016/j.scitotenv.2017.04.242

Buzug, T. M. (2008). Computed tomography. Springer Berlin, Heidelberg. https://doi.org/10.1007/978-3-540-39408-2

Cavé, L., Al, T., Xiang, Y., & Vilks, P. (2009). A technique for estimating one-dimensional diffusion coefficients in low-permeability sedimentary rock using X-ray radiography: Comparison with through-diffusion measurements. *Journal of contaminant hydrology*, *103*(1-2), 1-12. https://doi.org/10.1016/j.jconhyd.2008.08.001

Choi, J. W., Ko, W. I., & Kang, C. H. (1999). Reference spent fuel and its characteristics for a deep geological repository concept development. *Nuclear Engineering and Technology*, *31*(6), 23-38.

Clark, I. D., Al, T., Jensen, M., Kennell, L., Mazurek, M., Mohapatra, R., & Raven, K. G. (2013). Paleozoic-aged brine and authigenic helium preserved in an Ordovician shale aquiclude. *Geology*, *41*(9), 951-954. https://doi.org/10.1130/G34372.1

Chaplin, R. (2014). Genealogy of CANDU Reactors. In Garland, J. W. (Ed.), The Essential CANDU, A Textbook on the CANDU Nuclear Power Plant Technology, University Network of Excellence in Nuclear Engineering (UNENE), ISBN 0-9730040. Retrieved from https://www.unene.ca/education/candu-textbook on 02/2023.

Chaplin, R. (2014). Introduction to nuclear reactors. In Garland, J. W. (Ed.), The Essential CANDU, A Textbook on the CANDU Nuclear Power Plant Technology, University Network of Excellence in Nuclear Engineering (UNENE), ISBN 0-9730040. Retrieved from https://www.unene.ca/education/candu-textbook on 02/2023.

Costigliola, L., Heyes, D. M., Schrøder, T. B., & Dyre, J. C. (2019). Revisiting the Stokes-Einstein relation without a hydrodynamic diameter. *The Journal of chemical physics*, *150*(2). https://doi.org/10.1063/1.5080662

Descostes, M., Blin, V., Bazer-Bachi, F., Meier, P., Grenut, B., Radwan, J., ... & Tevissen, E. (2008). Diffusion of anionic species in callovo-oxfordian argillites and oxfordian limestones (Meuse/Haute–Marne, France). *Applied Geochemistry*, *23*(4), 655-677. https://doi.org/10.1016/j.apgeochem.2007.11.003

Fuller, A. J., Shaw, S., Ward, M. B., Haigh, S. J., Mosselmans, J. F. W., Peacock, C. L., ... & Burke, I. T. (2015). Caesium incorporation and retention in illite interlayers. *Applied Clay Science*, *108*, 128-134. https://doi.org/10.1016/j.clay.2015.02.008

Graupner, B. J., Shao, H., Wang, X. R., Nguyen, T. S., Li, Z., Rutqvist, J., ... & Garitte, B. (2018). Comparative modelling of the coupled thermal–hydraulic-mechanical (THM) processes in a heated bentonite pellet column with hydration. *Environmental earth sciences*, *77*, 1-16. https://doi.org/10.1007/s12665-018-7255-3

Gobien, M. and M. Ion. 2019. *Nuclear fuel waste projections in Canada* - 2019 update. Nuclear Waste Management Organization (NWMO). Technical report NWMO-TR-2019-14. Available at <www.nwmo.ca>.

Hall, D. S., Behazin, M., Binns, W. J., & Keech, P. G. (2021). An evaluation of corrosion processes affecting copper-coated nuclear waste containers in a deep geological repository. *Progress in Materials Science*, *118*, Article 100766. https://doi.org/10.1016/j.pmatsci.2020.100766

Heckman, K., & Edward, J. (2020). *Radionuclide inventory for reference CANDU fuel bundles.* Nuclear Waste Management Organization (NWMO). Technical report NWMO-TR-2020-05. Available at <www.nwmo.ca>.

Henrion, P. N., Monsecour, M., Fonteyne, A., Put, M., & De Regge, P. (1985). Migration of radionuclides in Boom Clay. *Radioact. Waste Manage. Nucl. Fuel Cycle*, *6*(3-4), 313-359.

Idemitsu, K., Furuya, H., Hara, T., & Inagaki, Y. (1992). Migration of cesium, strontium and cobalt in water-saturated inada granite. *journal of nuclear science and technology*, *29*(5), 454-460. https://doi.org/10.1080/18811248.1992.9731551

Idemitsu, K., Kozaki, H., Yuhara, M., Arima, T., & Inagaki, Y. (2016). Diffusion behavior of selenite in purified bentonite. *Progress in Nuclear Energy*, *92*, 279-285. https://doi.org/10.1016/j.pnucene.2015.08.012

Johansson, H., Siitari-Kauppi, M., Skålberg, M., & Tullborg, E. L. (1998). Diffusion pathways in crystalline rock—examples from Äspö-diorite and fine-grained granite. *Journal of Contaminant Hydrology*, *35*(1-3), 41-53. https://doi.org/10.1016/S0169-7722(98)00114-4

Katz JJ, Rabonowitch E (1951) *The chemistry of uranium part I: the element, its binary and related compounds*. McGraw-Hill Book Company Inc.

King, F., Chen, J., Qin, Z., Shoesmith, D., & Lilja, C. (2017). Sulphide-transport control of the corrosion of copper canisters. *Corrosion Engineering, Science and Technology*, *52*(sup1), 210-216. https://doi.org/10.1080/1478422X.2017.1300363

Lee, C. P., Wu, M. C., Tsai, T. L., Wei, H. J., Men, L. C., & Lin, T. Y. (2012). Comparative study on retardation behavior of Cs in crushed and intact rocks: two potential repository host rocks in the Taiwan area. *Journal of Radioanalytical and Nuclear Chemistry*, *293*(2), 579-586. https://doi.org/10.1007/s10967-012-1684-3

Li, Z., Su, G., Zheng, Q., & Nguyen, T. S. (2020). A dual-porosity model for the study of chemical effects on the swelling behaviour of MX-80 bentonite. *Acta Geotechnica*, *15*, 635-653. https://doi.org/10.1007/s11440-019-00762-5

Loomer, D. B., Scott, L., Al, T. A., Mayer, K. U., & Bea, S. (2013). Diffusion–reaction studies in low permeability shale using X-ray radiography with cesium. *Applied geochemistry*, *39*, 49-58. https://doi.org/10.1016/j.apgeochem.2013.09.019

Maldonado-Sànchez, G. (2020). *Measuring Diffusion Coefficients in Low-Porosity Rocks by X-Ray Radiography*. [Master's thesis, Université d'Ottawa / University of Ottawa] http://dx.doi.org/10.20381/ruor-25659

Martz, H. E., Logan, C. M., Schneberk, D. J., & Shull, P. J. (2016). *X-ray Imaging: fundamentals, industrial techniques and applications*. CRC Press. https://doi.org/10.1201/9781315375199

Morelhão, S. L. (2016). *Computer simulation tools for x-ray analysis: scattering and diffraction methods.* Springer Cham. https://doi.org/10.1007/978-3-319-19554-4

Melkior, T., Mourzagh, D., Yahiaoui, S., Thoby, D., Alberto, J. C., Brouard, C., & Michau, N. (2004). Diffusion of an alkaline fluid through clayey barriers and its effect on the diffusion properties of some chemical species. *Applied Clay Science*, *26*(1-4), 99-107. https://doi.org/10.1016/j.clay.2003.10.006

Muuri, E., Ikonen, J., Matara-Aho, M., Lindberg, A., Holgersson, S., Voutilainen, M., Siitari-Kauppi, M., Martin, A., (2016). Behavior of Cs in Grimsel granodiorite: sorption on main minerals and crushed rock. *Radiochimica Acta*, *104*(8), 575-582. https://doi.org/10.1515/ract-2016-2574

Muuri, E., Matara-aho, M., Puhakka, E., Ikonen, J., Martin, A., Koskinen, L., & Siitari-Kauppi, M. (2018). The sorption and diffusion of 133Ba in crushed and intact granitic rocks from the Olkiluoto and Grimsel in-situ test sites. *Applied Geochemistry*, *89*, 138-149. https://doi.org/10.1016/j.apgeochem.2017.12.004

Muuri, E., Siitari-Kauppi, M., Matara-aho, M., Ikonen, J., Lindberg, A., Qian, L., & Koskinen, L. (2017). Cesium sorption and diffusion on crystalline rock: Olkiluoto case

study. *Journal of Radioanalytical and Nuclear Chemistry*, *311*, 439-446. https://doi.org/10.1007/s10967-016-5087-8

Nakashima, Y. (2000). The use of X-ray CT to measure diffusion coefficients of heavy ions in water-saturated porous media. *Engineering Geology*, *56*(1-2), 11-17. https://doi.org/10.1016/S0013-7952(99)00130-1

Narasimhan, T. N. (1999). Fourier's heat conduction equation: History, influence, and connections. *Reviews of Geophysics*, *37*(1), 151-172. https://doi.org/10.1029/1998RG900006

NEA (2008), Moving Forward with Geological Disposal of Radioactive Waste, OECD Publishing.

Noronha, J. (2016). *Deep geological repository conceptual designs report: crystalline/sedimentary rock environment*. Nuclear Waste Management Organization (NWMO). Technical report NWMO-APM-REP-00440-0015-R001. Available at <www.nwmo.ca>.

Nunn, J. A., Xiang, Y., & Al, T. A. (2018). Investigation of partial water saturation effects on diffusion in shale. *Applied Geochemistry*, *97*, 93-101. https://doi.org/10.1016/j.apgeochem.2018.08.004

Parkhurst, D.L., and Appelo, C.A.J., 2013, Description of input and examples for PHREEQC version 3—A computer program for speciation, batch-reaction, one-dimensional transport, and inverse geochemical calculations: U.S. Geological Survey Techniques and Methods, book 6, chap. A43, 497 p., available only at http://pubs.usgs.gov/tm/06/a43/

Poinssot, C., Baeyens, B., & Bradbury, M. H. (1999). Experimental and modelling studies of caesium sorption on illite. *Geochimica et cosmochimica Acta*, *63*(19-20), 3217-3227. https://doi.org/10.1016/S0016-7037(99)00246-X

Poludniowski, G., Omar, A., & Andreo, P. (2022). *Calculating X-ray Tube Spectra: Analytical and Monte Carlo Approaches*. CRC Press. https://doi.org/10.1201/9781003058168

Rashwan, T. L., Asad, M. A., Molnar, I. L., Behazin, M., Keech, P. G., & Krol, M. M. (2022). Exploring the governing transport mechanisms of corrosive agents in a Canadian deep geological repository. *Science of The Total Environment*, *828*, 153944. https://doi.org/10.1016/j.scitotenv.2022.153944

Reily, t. (2023) *Nuclear Fuel Waste Projections in Canada* – 2023 Update. Nuclear Waste Management Organization (NWMO). Technical report NWMO-TR-2023-09. Available at <www.nwmo.ca>.

Shoesmith, D. W. The chemistry/electrochemistry of spentnuclear fuel as a wasteform. In Uranium: Cradle to Grave; Burns, P. C.,Sigmon, G. E., Eds.; Short Course Series 43; Mineralogical Associationof Canada, 2013; pp 337−368.

Schmeide, K., Gürtler, S., Müller, K., Steudtner, R., Joseph, C., Bok, F., & Brendler, V. (2014). Interaction of U (VI) with Äspö diorite: A batch and in situ ATR FT-IR sorption study. *Applied geochemistry*, *49*, 116-125. https://doi.org/10.1016/j.apgeochem.2014.05.003

Scully, J.R., Feron, D., & Hanninen, H. (2016). *Review of the NWMO copper corrosion program*. Nuclear Waste Management Organization (NWMO). Technical report NWMO-TR-2016-11. Available at <www.nwmo.ca>.

Shrestha, R., Černoušek, T., Stoulil, J., Kovářová, H., Sihelská, K., Špánek, R., ... & Steinová, J. (2021). Anaerobic microbial corrosion of carbon steel under conditions relevant for deep geological repository of nuclear waste. *Science of The Total Environment*, *800*, 149539. https://doi.org/10.1016/j.scitotenv.2021.149539

Spiessl, S. M., MacQuarrie, K. T. B., & Mayer, K. U. (2008). Identification of key parameters controlling dissolved oxygen migration and attenuation in fractured crystalline rocks. *Journal of Contaminant Hydrology*, *95*(3-4), 141-153. https://doi.org/10.1016/j.jconhyd.2007.09.002

Stumm, W. (1992). *Chemistry of the solid-water interface: processes at the mineral-water and particle-water interface in natural systems*. John Wiley & Son Inc. https://doi.org/10.5555/19931974135

Tait, J.C., H. Roman and C.A. Morrison. 2000. *Characteristics and radionuclide inventories of used fuel from OPG nuclear generating stations* - Volume 1 - Main Report. Ontario Power Generation Report 06819-REP-01200-10029-R00.

Tidwell, V. C., Meigs, L. C., Christian-Frear, T., & Boney, C. M. (2000). Effects of spatially heterogeneous porosity on matrix diffusion as investigated by X-ray absorption imaging. *Journal of Contaminant Hydrology*, *42*(2-4), 285-302. https://doi.org/10.1016/S0169-7722(99)00087-X

Urpi, L., Rinaldi, A. P., Rutqvist, J., & Wiemer, S. (2019). Fault stability perturbation by thermal pressurization and stress transfer around a deep geological repository in a clay formation. *Journal of Geophysical Research: Solid Earth*, *124*(8), 8506-8518. https://doi.org/10.1029/2019JB017694

Van Loon, L. R., Baeyens, B., & Bradbury, M. H. (2005). Diffusion and retention of sodium and strontium in Opalinus clay: Comparison of sorption data from diffusion and batch sorption measurements, and geochemical calculations. *Applied Geochemistry*, *20*(12), 2351-2363. https://doi.org/10.1016/j.apgeochem.2005.08.008

Van Loon, L. R., Glaus, M. A., & Müller, W. (2007). Anion exclusion effects in compacted bentonites: towards a better understanding of anion diffusion. *Applied Geochemistry*, *22*(11), 2536-2552. https://doi.org/10.1016/j.apgeochem.2007.07.008

Van Loon, L. R., & Mibus, J. (2015). A modified version of Archie's law to estimate effective diffusion coefficients of radionuclides in argillaceous rocks and its application in safety

analysis studies. *Applied Geochemistry*, *59*, 85-94. https://doi.org/10.1016/j.apgeochem.2015.04.002

Van Loon, L. R., Soler, J. M., & Bradbury, M. H. (2003). Diffusion of HTO, 36Cl− and 125I− in Opalinus Clay samples from Mont Terri: Effect of confining pressure. *Journal of Contaminant Hydrology*, *61*(1-4), 73-83. https://doi.org/10.1016/S0169-7722(02)00114-6

Vilks, P., Cramer, J. J., Jensen, M., Miller, N. H., Miller, H. G., & Stanchell, F. W. (2003). In situ diffusion experiment in granite: phase I. *Journal of contaminant hydrology*, *61*(1-4), 191-202. https://doi.org/10.1016/S0169-7722(02)00135-3

Vilks, P. Miller, N. H. (2007). *Evaluation of Experimental Protocols for Characterizing Diffusion in Sedimentary Rocks*. Nuclear Waste Management Organization (NWMO). Technical report NWMO-TR-2007-11. Available at <www.nwmo.ca>.

Wersin, P., Van Loon, L. R., Soler, J. M., Yllera, A., Eikenberg, J., Gimmi, T., ... & Boisson, J. Y. (2004). Long-term diffusion experiment at Mont Terri: first results from field and laboratory data. *Applied Clay Science*, *26*(1-4), 123-135. https://doi.org/10.1016/j.clay.2003.09.007

Widestrand, H., Byegård, J., Cvetkovic, V., Tullborg, E. L., Winberg, A., Andersson, P., & Siitari-Kauppi, M. (2007). Sorbing tracer experiments in a crystalline rock fracture at Äspö (Sweden): 1. Experimental setup and microscale characterization of retention properties. *Water Resources Research*, *43*(10). https://doi.org/10.1029/2006WR005277

Xiang, Y., Al, T., & Mazurek, M. (2016). Effect of confining pressure on diffusion coefficients in clay-rich, low-permeability sedimentary rocks. *Journal of contaminant hydrology*, *195*, 1-10. https://doi.org/10.1016/j.jconhyd.2016.10.004

Xiang Yan, Loomer, D., & Al, T. (2016). Improvements in methodologies for radiographic measurement of diffusion properties in low-permeability rocks, and development of methods for pH measurement in brines. Nuclear Waste Management organization (NWMO). Technical report NWMO-TR--2016-16. Available at <www.nwmo.ca>.

Xiang, Y., Al, T., Scott, L., & Loomer, D. (2013). Diffusive anisotropy in low-permeability Ordovician sedimentary rocks from the Michigan Basin in southwest Ontario. *Journal of contaminant hydrology*, *155*, 31-45. https://doi.org/10.1016/j.jconhyd.2013.09.002

Zheng, Z., Guido Garcia, F., Liu, J., Nagasaki, S., & Yang, T. (2024). Sorption of U (VI) on MX-80 Bentonite and Granite in Ca-Na-Cl Saline Solutions. *Nuclear Technology*, 1-12. https://doi.org/10.1080/00295450.2023.2300900

Zschornack, G. H. (2007). *Handbook of X-ray Data*. Springer Science & Business Media. https://doi.org/10.1107/S0108767307011506

CHAPTER 2

DIFFUSION OF IODIDE IN GRANITE: AN X-RAY RADIOGRAPHY METHOD

CHARLES CADIEUX, SAMUEL MORFIN, GUADALUPE MALDONADO-SÁNCHEZ, DOMINIQUE BOWER, TOM AL

Department of Earth and Environmental Sciences, University of Ottawa, Ottawa, ON, K1N 6N5, Canada

Abstract

Deep geological repositories for radioactive waste disposal are key for the long-term viability of nuclear energy. Granites are of interest because they provide a low-permeability and low-diffusivity barrier against solute migration via advection and diffusion. X-ray radiography has already been used to measure diffusion coefficients, but the low porosity and the heterogeneity of crystalline rocks such as granite pose challenges. Because X-ray radiography is a difference-imaging technique, alignment (registration) of the reference and time-series images has an important effect on the measured signal. Here, we present modifications to this method that allow measurement of diffusion properties of granite with <0.5 % porosity by rotating the cylindrical samples on their vertical axis during image acquisition. It was found that rotating the samples allows for integrated images to be acquired, eliminating the need for horizontal registration and reducing the overall error associated with image registration. The modified X-ray radiography technique was used succesfully to estimate the effective diffusion coefficient (D_e) for iodide (range: 2.7×10^{-14} – 3.6×10^{-14} $m^2\cdot s^{-1}$, average: 3.1×10^{-14} $m^2\cdot s^{-1}$) and compare the results with through-diffusion measurements (range: 6.9×10^{-14} – 1.0×10^{-13} $m^2\cdot s^{-1}$, average: $8.7 \pm 1.7\times10^{-14}$ $m^2\cdot s^{-1}$) in an intact, 0.35 % porosity crystalline rock (Lac du Bonnet granite, Manitoba, Canada).

2.1. Introduction

Over the past decades, most countries with nuclear power generation capacities have shown interest in the use of deep geological repositories to store nuclear waste (NEA, 2008). Granite, and other low porosity and low permeability crystalline rocks, are of interest because they could provide a natural barrier against radionuclide transport. In Canada, pore structure and solute transport within crystalline rocks have been studied for this purpose since the 70's (Wadden & Katsube, 1982). Quantification of transport and sorption processes is crucial for determining if a rock formation is suitable to isolate waste on long timescales.

It is well-known that diffusion is the dominant solute transport mechanism in unfractured crystalline and clay-rich sedimentary rocks of low permeability (Boving & Grathwohl, 2001; Spiessl et al., 2008; Agbogun et al., 2013). The through-diffusion (TD) method is one of the most common approaches to study matrix diffusion and it is based on measurements of tracer flux through a sample during steady-state diffusion. Through-diffusion is well-established and is commonly used with conservative tracers such as tritiated water (HTO) or anions (Cl^-, Br^-, I^-) to study diffusion in sedimentary rocks (Boving & Grathwohl, 2001; Van Loon et al., 2003; Vilks & Miller, 2007; Descostes et al., 2008; Cavé et al., 2009; Xiang et al., 2013, 2016). Out-diffusion and in-diffusion experiments are also commonly used, wherein the flux of tracer out or into a sample, or the tracer concentrations within a sample, are measured to estimate diffusion properties (Shackelford 1991; Van Loon et al., 2005; Waber et al., 2011). In-diffusion experiments commonly aim to measure concentration profiles of tracers in the pore fluid of a sample at specific times during transient diffusion using methods such as autoradiography (Johansson et al., 1998; Lee et al., 2012), radiography (Tidwell et al. 2000; Cavé et al., 2009), γ-spectroscopy (Idemitsu et al., 1992; Widestrand et al., 2007; Muuri et al., 2018), X-ray CT

(Nakashima, 2000; Agbogun et al., 2013) and destructive sampling with sectioning techniques. The TD method, and others that require the establishment of steady-state diffusion (Shackelford, 1991), are well suited for measurements using conservative tracers, but the experimental duration can be very long (years) when reactive tracers are involved (Jakob et al., 2009).

The X-ray radiography technique is the focus of this study. Radiography has proven useful to quantify diffusion in various rocks at the laboratory scale (Cavé et al., 2009). The fast and non-destructive nature of X-ray-based techniques, as well as their high spatial and temporal resolution are advantageous in studying the behaviour of tracers in porous media, particularly during the transient stage of diffusion (Tidwell & Glass, 1994; Nakashima, 2000). X-ray radiography has been used previously to study diffusion in clay-rich sedimentary rocks such as shale (Cavé et al., 2009; Loomer et al., 2013a; Nunn et al., 2018) and argillaceous limestone (Xiang et al., 2013), as well as dolomite (Tidwell et al., 2000) and fractured granite with porosities ranging from ~ 3 % to 15 % (Altman et al., 2004). However, we are not aware of any diffusion studies conducted with X-ray radiography on intact, low-porosity crystalline rocks.

2.1.1. Principles of X-ray radiography method

The radiography method measures the diminished intensity of X-rays (attenuation) as the beam is transmitted through a sample. For diffusion studies, it is based on the attenuation of X-rays caused by a tracer that is diffusing in the pore fluid of the rock, and its principles are described by Cavé et al. (2009). Mainly, the change in attenuation at points along the diffusion path $(\Delta\mu)_x$ due to the presence of a tracer is obtained by subtracting time-series radiographs (acquired during the diffusion of the tracer) from a reference radiograph of the sample (acquired before the start of diffusion). For one-dimensional diffusion, this spatially resolved parameter is defined as:

$$(\Delta\mu)_x = \ln (I_{ref})_x - \ln (I_t)_x \quad [2.1]$$

where I_{ref} is the intensity of X-rays transmitted through the sample in the reference image that is acquired when t = 0, and I_t is the intensity of X-rays transmitted through the sample in the time-series images (t > 0), both at distance x along the one-dimensional diffusion path. This is effectively a blank subtraction method that eliminates the constant attenuation caused by the porous media, leaving only the change in attenuation caused by the changing tracer concentration over time in the pores.

The relative tracer concentration along the diffusion path (C_x/C_0) and the pore diffusion coefficient (D_p) for a conservative tracer (here iodide) are obtained by fitting the time- and spatially-resolved X-ray attenuation profiles to an analytical solution of Fick's second law (Crank 1975) using a least-squares regression, similar to what was done in previous work (Cavé et al., 2009; Xiang et al., 2013; Loomer et al., 2013a; Nunn et al., 2018). Important terms related to diffusion are defined in Table 1.

The use of this technique for low-porosity rocks with heterogeneous mineral distributions such as granite presents challenges. Misalignment of the reference and time-series images during subtraction is a common source of error (Nunn, 2018); this problem can cause errors of up to 5 % on C_x/C_0 when working with low-porosity samples (Cavé et al., 2009). In experiments using granite, image registration errors (misalignment) have led to a signal-to-noise ratio that is prohibitively low (Maldonado-Sánchez, 2020).

The objectives of this study are to:

- Modify the X-ray radiography technique described by Cavé et al. (2009) to minimize sensitivity to image registration errors.

- Test the modified radiography method to estimate the D_p of intact granite samples.
- Compare the results from radiography against measurements conducted by TD.

Table 2.1. Glossary of diffusion terms

Symbol	Name	Definition	Equation
D_e	Effective Diffusion Coefficient	The diffusion coefficient for a specific solute in a porous medium that accounts for the 3-dimensional geometry of the pore space, including tortuosity, constrictivity and diffusion-accessible porosity. It is the product of the *tracer-accessible porosity* ϕ_t, the *tortuosity factor* τ_f, and the *free-water diffusion coefficient* D_0.	$D_e = \phi_t \times \tau_f \times D_0$
D_0	Free-Water Diffusion Coefficient	The diffusion coefficient for a specific solute in bulk aqueous solution (no porous media) at 25 °C.	
D_p	Pore Diffusion Coefficient	The diffusion coefficient for a specific solute in porous medium that accounts for the 3-dimensional geometry of the pore space, including its tortuosity and constrictivity. It is the product of the *tortuosity factor* τ_f and the *free-water diffusion coefficient* D_0.	$D_p = \tau_f \cdot D_0$
τ	Tortuosity	A geometric factor that accounts for the effective transport path length for solute transport within a porous medium (L_e) compared to the shortest straight-line transport path length (L) between two points. Note that $\tau > 1$.	$\tau = (L_e / L)^2$
τ_f	Tortuosity Factor	An empirical factor that combines the *tortuosity* τ and the *constrictivity* δ to describe the geometric properties of the porous medium that influence diffusive transport. Note that $\tau_f < 1$.	$\tau_f = \delta / \tau$

2.2. Materials and methods

2.2.1. Sample description

Granitic samples used in this study were sourced from the Cold Spring Granite Company Quarry located approximately 12 km south of Lac du Bonnet, Manitoba, Canada. The quarry is on the Lac Du Bonnet batholith which lies in the Winnipeg River plutonic complex of the English River gneiss belt in the western Superior Province (Martin et al., 1990). The batholith is dated to be of late Archean age (2680 ± 90 Ma) (Farquharson, 1974) and is comprised of sparsely fractured pink porphyritic granite underlain by large domains of massive gray granite (Stevenson et al. 1996) with uniform medium to coarse grains (Martin et al., 1990; McCrank, 1985). The Lac du Bonnet granite has undergone three types of alteration: deuteric (lasting at least 100 Ma); hydrothermal (for about 2000 Ma); and low temperature (for about 450 Ma as erosion brought the granite near the surface) (Gascoyne & Cramer, 1987; McLaughlin 1992).

The mineralogy of the granite is consistent with its alteration history. McCrank (1985) described the mineralogy as 25-50 % plagioclase, which is frequently altered to carbonate, sericite and muscovite, 21-41 % quartz, 15-35 % microcline and 0-17 % biotite, which is variably replaced by chlorite or muscovite. X-ray microprobe analysis identified illite as the dominant clay mineral in fracture zones and this clay mineral also occurs as an alteration product on feldspar surfaces (Gascoyne & Kamineni, 1992).

Previous work indicates that the porosity ranges from 0.2-0.6 % with an average value of 0.39 % above 450 m and a higher average of 0.48 % below depths of 450 m due to stress-induced microcracks (Stevenson et al., 1996) and permeability values determined from seepage tests in open boreholes range from 3×10^{-17} m^2 to 1×10^{-21} m^2 at depths above 400 m (Stevenson et al., 1996).

2.2.2. Sample preparation and characterization

The granitic samples used in this study were obtained from two 101.6 mm diameter core segments. Samples from one segment were used for radiography experiments and samples from the second for TD experiments. For radiography, two 20-mm-thick disks were cut from the core using a water-cooled diamond saw, and five 20-mm long × 20-mm diameter cylinder-shaped subcores were obtained from the larger disks using a drill press equipped with a water-cooled diamond bit. The procedure was the same for samples prepared for TD, except the disks cut from the 101.6 mm core were 10 mm thick instead of 20 mm, and the subcores had final dimensions of 10-mm long × 25.4-mm diameter. The subcores were prepared for diffusion measurements by lapping with silicon carbide (60/80 grit) and water to remove mechanical damage from sawing and ensure the ends of the cylinders were perpendicular to the core axes. Two of the 20-mm long subcores were used for diffusion experiments with radiography; one with iodide tracer and the second with cesium tracer. The cesium diffusion results were inconclusive; they are presented and discussed in Appendix B. The three remaining 20-mm long subcores were used for water-accessible porosity (ϕ_w) measurements. Three of the 10-mm long subcores (CS6, CS7 and CS8) were used for TD measurements and the offcuts were used for ϕ_w measurements.

A polished thin section was prepared from the offcuts adjacent to the diffusion (radiography) samples. The thin section was carbon-coated and mineralogical data adjacent to the diffusion path were acquired with an optical microscope and by SEM-EDS at an accelerating voltage of 20 kV on a JEOL 6610LV series instrument equipped with an Oxford Inca EDS elemental analysis system at the University of Ottawa.

2.2.3. Synthetic porewater and tracer solutions

A synthetic porewater (SPW) designed to represent saline water in rocks of the Canadian Shield was used to saturate the samples. The iodide tracer solution was derived from the SPW, replacing NaCl in the SPW with a higher NaI concentration (2 mol/kgw) (Table 1). In solution, iodide undergoes photochemical oxidation, which leads to the formation of volatile I_2 through the following reaction (Miyake & Tsunogai, 1963, Rançon 1988, Truesdale, 2007):

$$2I^- + ½\ O_2 + H_2O + h\nu \rightarrow I_2 + 2OH^- \quad [2.2]$$

During the experiments, I^- oxidation was inhibited by addition of thiosulfate, an I_2 reducing agent (Rançon, 1988):

$$2Na_2S_2O_3 + I_2 \rightarrow 2NaI + Na_2S_4O_6 \quad [2.3]$$

Table 2.2. Composition of synthetic porewater and iodide tracer solution (mmol/kgw).

Solute	SPW	I^- tracer
I^-	0	2000
Na^+	147.5	2020
Ca^{2+}	100	100
Mg^{2+}	2.5	2.5
K^+	0.57	0.57
Cl^-	341.27	193.77
$SO4^{2-}$	5.9	5.9
$S_2O_3^{2-}$	0	10

2.2.4. Water-accessible porosity measurement

Water-accessible porosity (ϕ_w) values were determined using an established method (Al et al., 2010; Loomer et al., 2013b), which is consistent with that of Blum (1997) and Emerson (1990) and has been used in previous studies (Xiang et al., 2013; Loomer et al., 2013a). The granite samples were delivered in a partially dried condition, so they were dried completely at

105 °C, while monitoring the sample mass periodically over 36 days until a final stable dry mass was recorded. The samples were then saturated in SPW following procedures reported by Xiang et al. (2016) prior to measuring the saturated mass and submerged mass. To summarize, saturation is achieved in a vacuum chamber with samples first being subjected to repeated cycles of vacuum and pure CO_2 gas, allowing air from the pores to be replaced by soluble CO_2. The samples are then immersed in SPW, still under vacuum, and the sample mass is monitored over time until a stable mass is achieved.

2.2.5. Diffusion cell design

For the X-ray radiography experiment, the saturated samples were mounted on acrylic pedestals above solution reservoirs equipped with fluid injection ports (Fig. 2.1, top). Thin disks of felt fabric were placed underneath and on top of the sample in order to maintain saturation by capillarity and thereby prevent formation of gas bubbles at the inlet and outlet diffusion boundaries. An aluminum cap with an injection hole was placed on top of each sample. A thin layer of silicone gel was applied on the outer surface of the samples and the aluminum caps with a fine brush to prevent diffusion of tracer along the periphery. Plastic heat-shrink tubing and two heat-shrink clamps were used to tightly seal the peripheral surface. The lower reservoir and the felt at the top of the sample were saturated with SPW and the diffusion cells were stored in an airtight container with an open vessel of SPW in order to maintain an equilibrium vapour pressure and prevent evaporation.

For the TD experiment, diffusion cells like those described by Xiang et al. (2013) were used (Fig. 2.1, bottom). The cells are comprised of a clamped sample-containment sleeve and two end plates held together with a set of bolts. Each end plate is connected to a solution reservoir via plastic tubing.

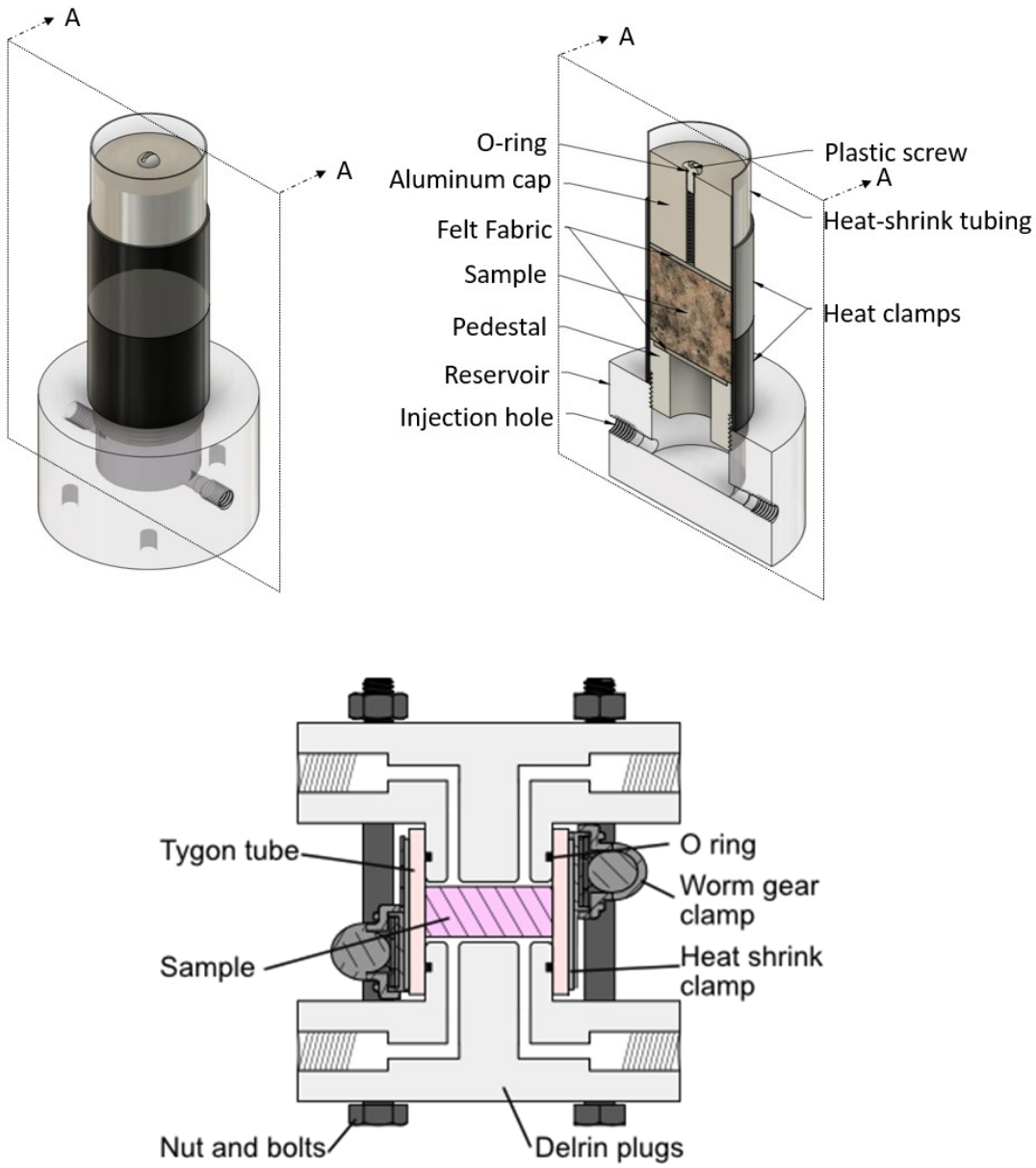

Fig. 2.1. Schematic diagrams of the diffusion cells: top) radiography, bottom) TD.

2.2.6. X-ray radiography

At time t = 0, SPW in the reservoir below the sample was replaced by tracer solution. Time-series radiographs were acquired at approximately 24-hour intervals for four days, and then at intervals of two to three days for the remainder of the experiment. Radiographs were acquired with an X-ray CT system (Pinnacle X-ray Systems, Atlanta, Georgia) equipped with a Varian® NDI-160/22 source coupled to a Gulmay® CPL series (CP2-1402) 3000 W generator

and a Varian PaxScan®1313DX amorphous-silicon flat-panel imaging detector. Each image consists of an average of 180 frames acquired at 6 frames per second (FPS), for a total acquisition time of 30 seconds. In order to eliminate image-registration errors from lateral misalignment between the reference and time-series images, the sample was rotated through 720 degrees on its vertical axis during all image acquisitions. The X-ray source (60 kV and 21 mA) was filtered with 3.3 mm of aluminum to minimize beam hardening effects.

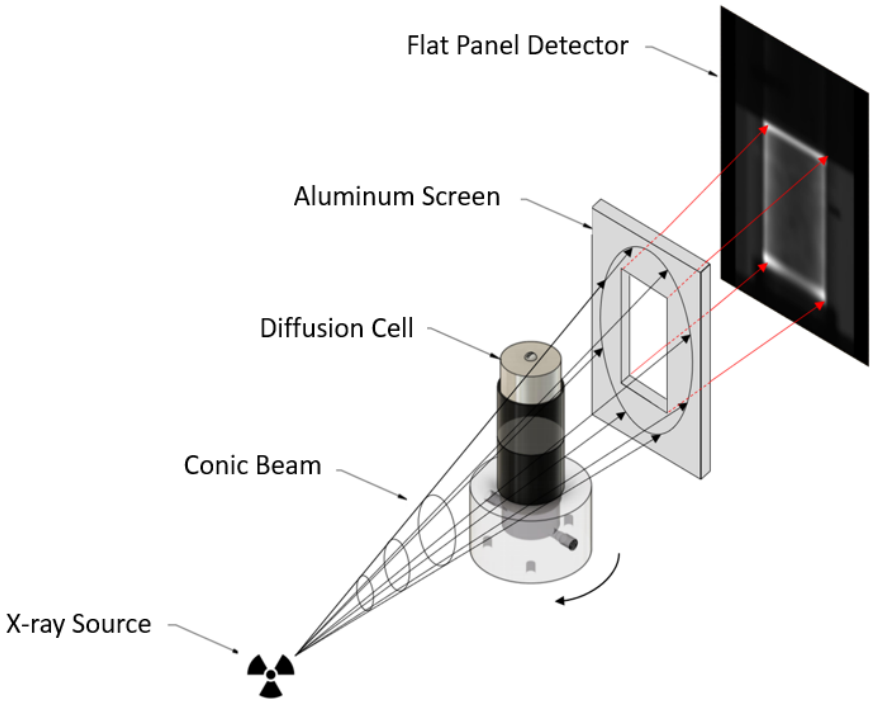

Fig. 2.2. Experimental set up for acquisition of radiographic images.

Grayscale images (16 bit) were analyzed in ImageJ (Rasband, 2018) using the method described by Cavé et al. (2009) (details in Appendix A). The grayscale values (GSV) of each row of pixels in the reference and time-series radiographs were averaged to produce one-dimensional profiles representing the transmitted X-ray intensity at points along the sample length, $(I_t)_x$. Tracer X-ray attenuation ($\Delta\mu$) profiles were obtained by subtracting each time-series profile from the reference profile (Eq. 2.1). The average X-ray attenuation (μ) of an area on top of the sample,

which was not impacted by diffusion, was used as an internal standard to normalise the data and control for X-ray source intensity variations.

As reported by Cavé et al. (2009) and Loomer et al. (2013a), the D_p for iodide was determined using a least-squares regression fit approach with an analytical solution to Fick's second law (Crank, 1975):

$$\frac{C_{(x,t)}}{C_0} = \mathrm{erfc}\left[\frac{x}{2 \cdot \sqrt{D_p \cdot t}}\right] \quad [2.4]$$

valid for the following boundary conditions:

$$C(x,t) = 0 \begin{cases} t = 0 \\ x > 0 \end{cases}$$

$$C(x,t) = C_0 \begin{cases} t \geq 0 \\ x = 0 \end{cases}$$

$$C(x,t) = 0 \begin{cases} t \geq 0 \\ x = L \end{cases}$$

where $C_{(x,t)}$ is the concentration of the tracer at position x (m) along the diffusion path and at time t (s) since the start of diffusion and C_0 is the constant concentration of the tracer at the influx boundary.

Loomer et al. (2013a) used a calibration curve to determine the absolute concentration of iodide in the pores based on the $\Delta\mu$ values. In this study, it was not possible to conduct a calibration that could accurately account for beam hardening in the sample (see Appendix B). Alternatively, the $\Delta\mu$ value corresponding to the position of the tracer influx boundary where $C/C_0 = 1$ ($\Delta\mu_0$) was determined using least squares fitting of the profiles (details in Appendix A) and then the relative tracer concentrations (C_x/C_0) corresponding to each $\Delta\mu_x$ was determined based on the optimized $\Delta\mu_0$ value (Eq. 2.5):

$$\frac{C_x}{C_0} = \frac{\Delta\mu_x}{\Delta\mu_0} \quad [2.5]$$

2.2.7. Through-diffusion

The TD experiment procedures closely follow those outlined by Xiang et al. (2013). Briefly, three samples were cut from Lac du Bonnet granite core (Cold Spring Quarry) with a drill and lapped to remove surface imperfections. The subcores were saturated in SPW under vacuum, as described in Xiang et al. (2016). The samples were loaded in the diffusion cells and pressure-tested to ensure both sides of the samples were fully isolated. The cells were connected to solution reservoirs on each end of the samples via polyethylene tubing and a peristaltic pump ensured constant circulation of the solutions (Fig. 2.3). At t=0, one reservoir was spiked with tracer (iodide or tritiated water, HTO) to start the diffusion experiment. This effectively creates one high-tracer-concentration reservoir and one low-concentration reservoir to drive diffusion across each sample for the duration of the experiment. At specific time intervals, the solution in the low-concentration reservoir was removed and replaced with fresh SPW to preserve boundary conditions. The solutions collected from the low-concentration reservoirs were analyzed to determine the tracer concentration using inductively-coupled-plasma mass spectrometry (ICP-MS) for iodide or liquid scintillation counting (LSC) for HTO. The experiment was conducted for approximately 30 days beyond the onset of steady-state conditions.

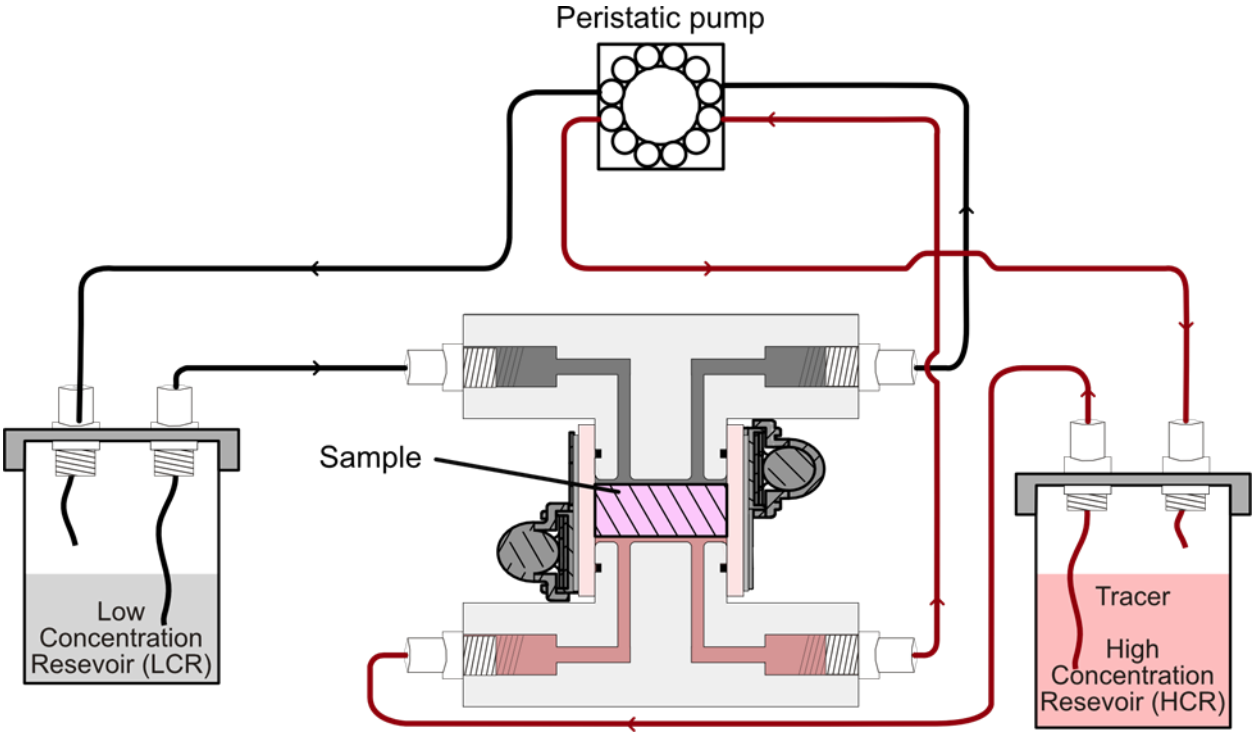

Fig. 2.3. Schematic representation of the assembled apparatus for through-diffusion experiments.

The data analysis was performed as outlined by Van Loon et al. (2003) by linear regression analysis of the steady-state accumulation data:

$$Q_t = \frac{C_0 \cdot S \cdot D_e}{L} \cdot t - \frac{C_0 \cdot \alpha \cdot S \cdot L}{6} \quad [2.6]$$

where Q_t is the accumulated tracer mass at time t (mol or Bq) in the low concentration reservoir, C_0 is the concentration or activity in the high-concentration reservoir, S is the cross-section area of the sample (m^2), L is the diffusion path length (m), t is time (s) since start of diffusion, D_e is the effective diffusion coefficient ($m^2 \cdot s^{-1}$) and α is the rock capacity factor. When steady-state diffusion is reached, the Q_t becomes a linear function of time and the unknown parameters D_e and α can be estimated from the slope (a) and the intercept (b) of the linear regression, respectively:

$$D_e = \frac{a \cdot L}{S \cdot C_0} \quad [2.6.1]$$

$$\alpha = -\frac{b \cdot 6}{S \cdot L \cdot C_0} \quad [2.6.2]$$

Additionally, D_e can be estimated based on the measured tracer diffusion flux (J_d):

$$D_e = \frac{J_d \cdot L}{(C_0 - C)} \quad [2.7]$$

2.3. Results

2.3.1. Water-accessible porosity

Results of three ϕ_w measurements conducted on subsamples from the core segment used for radiography indicate values that range from 0.31-0.40 %, with an average of 0.35 ± 0.05 % (Table 2.3). Three replicate measurements from a sample of the core segment used for TD measurements returned a value of 0.42 % (Table 3).

Table 2.3. Results obtained from the ϕ_w measurements.

	ϕ_w (%)	
Sample	Radiography Samples	TD Sample
1	0.40	
2	0.31	
3	0.35	
1		0.43
1		0.41
1		0.41
Average ± 1σ	0.35 ± 0.05	0.42 ± 0.01

2.3.2. Mineralogical characterization

Optical-microscopy and SEM analyses of thin sections indicate that the mineralogical composition is similar to that described by McCrank (1985) and Gascoyne and Kamineni, (1992), dominated by, in decreasing order, plagioclase, quartz, microcline and biotite. The presence of secondary porosity and alteration minerals is of particular interest to studies of solute

diffusion, and optical microscopy examinations show evidence of sericitization and a relatively high biotite content, which is partially to near-completely replaced by chlorite or muscovite (Fig. 2.4A). Additional SEM work indicates the presence of clay minerals infilling some of the pore space (Fig. 2.4B).

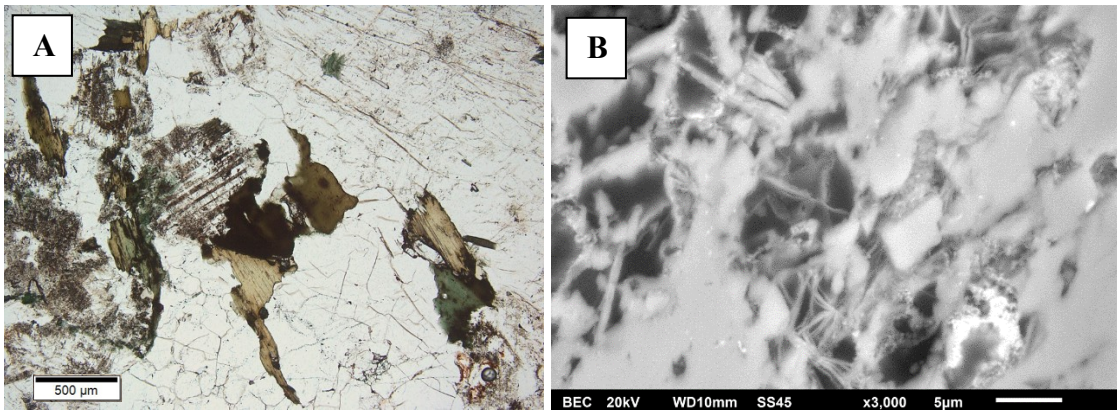

Fig. 2.4. Lac du Bonnet granite thin section showing (A) plane-polarized light optical microscope image with biotite partly altered to chlorite and clay minerals in altered plagioclase, and (B) backscattered-electron image (BSE image) of pore space infilled with clay minerals.

2.3.3. X-ray Radiography

X-ray radiographs of the granite sample were acquired during the transient phase of the diffusion experiment with the iodide tracer. Relative concentration profiles derived from the radiographs are presented in Fig. 2.5, with the left side of the figure corresponding to the tracer-influx boundary which is in contact with the tracer solution. Data are not available for the first and last 2 mm of the sample domain because these regions are affected by blurring due to the low spatial resolution of the X-ray beam. The dotted symbols represent the experimental relative iodide concentration data at five different times after the start of the diffusion experiment. The solid lines represent the best-fit regression model from Fick's second law of diffusion (Eq 2.2) for each of the measurement times. The data generally reflect expectations for diffusive

transport, but there are deviations from the model curves, especially at low concentrations. The D_p values obtained by fitting the model to the data are listed on the figure for each measurement time and the average D_p is 2.4 ± 0.3 × 10^{-11} m^2/s.

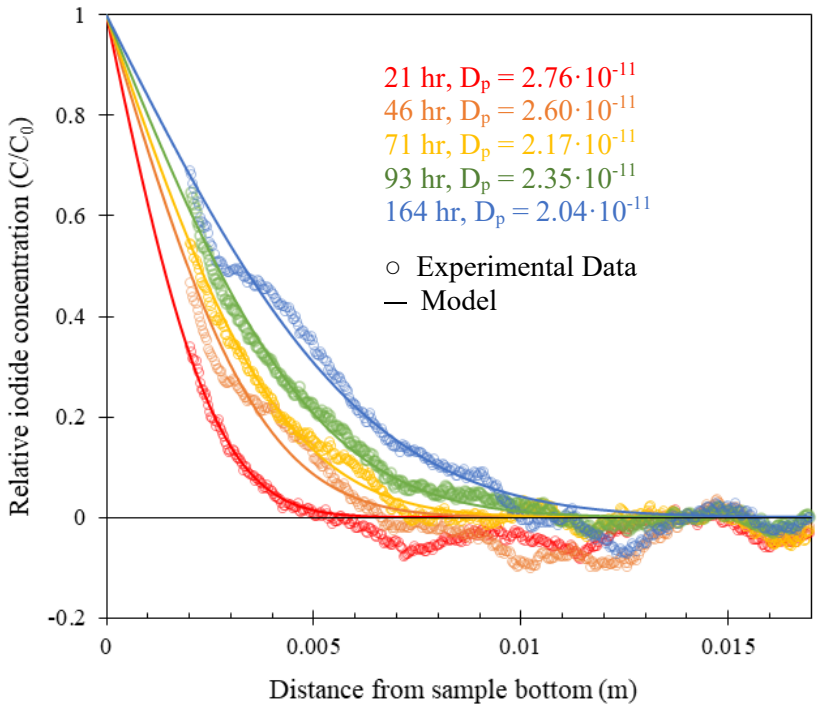

Fig. 2.5. Relative concentration (C_x/C_0) profiles for iodide tracer in the Lac du Bonnet granite with fitted analytical solution.

2.3.4. Through-diffusion

Through-diffusion experiments with the Lac du Bonnet granite were conducted with iodide and HTO. As an example, the measured diffusion flux across the sample and the mass accumulation in the low concentration reservoir for one of the samples (CS6) are presented in Fig. 2.6 and Fig. 2.7 for iodide and HTO, respectively. The vertical lines separate the transient-state diffusion period from the steady-state period. Steady-state is reached at approximately 12 and 16 days for iodide and HTO, respectively. The steady-state mass accumulation measurements and the diffusive mass flux data (J_D) allow calculation of D_e and α, which are

summarized in Table 4. Average D_e values of $8.7 \pm 1.7 \cdot 10^{-14}$ m^2/s and $1.9 \pm 0.2 \cdot 10^{-13}$ m^2/s were calculated for iodide and HTO, respectively. Average rock capacity factors of 0.13 ± 0.01 % and 0.48 ± 0.05 % were calculated for iodide and HTO, respectively.

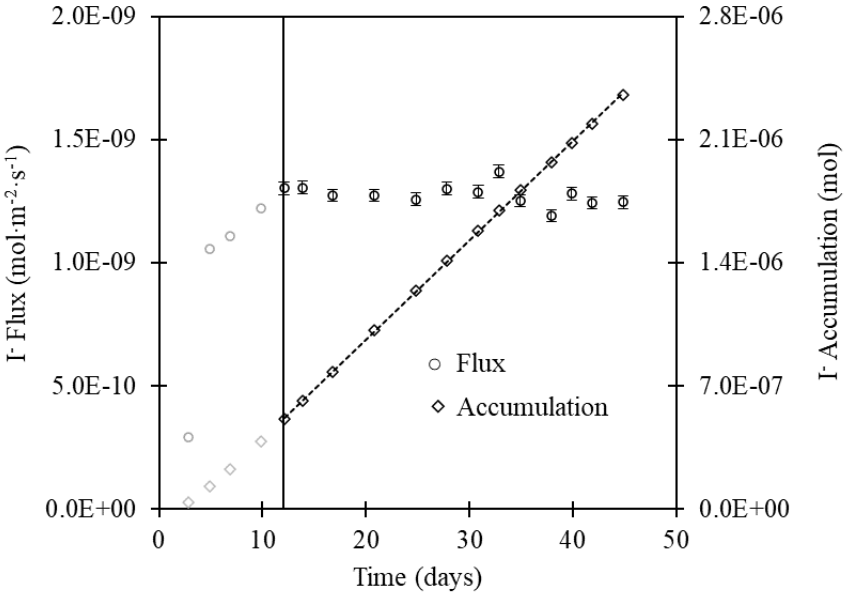

Fig. 2.6. Flux (J_D) and mass accumulation (Q_t) data from a TD experiment with iodide in Lac du Bonnet granite, sample CS6. Error bars on the flux represent the maximum total analytical uncertainty.

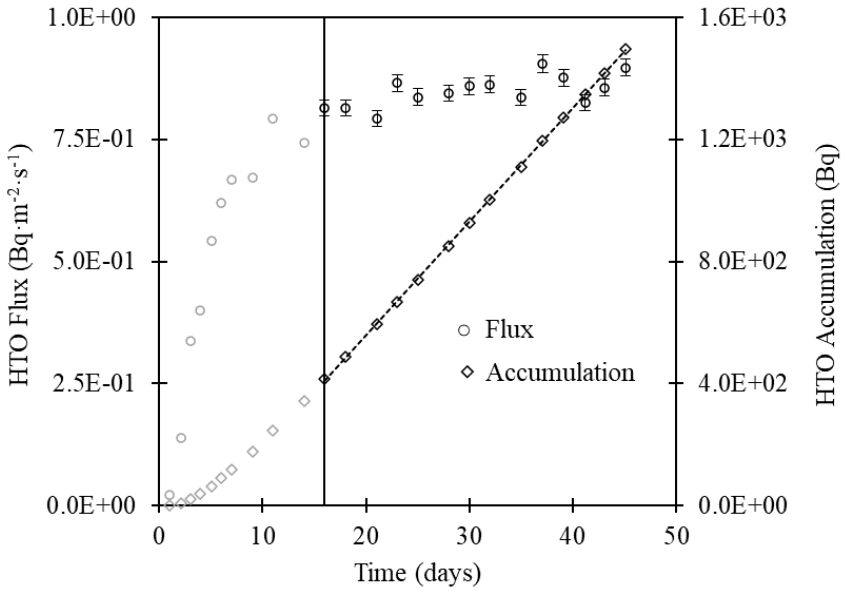

Fig. 2.7. Flux (J_D) and mass accumulation (Q_t) data from a TD experiment with HTO in Lac du Bonnet granite, sample CS6. Error bars on the flux represent the maximum total analytical uncertainty.

Table 2.4. Summary of diffusion-coefficient and rock-capacity-factor measurements for iodide and HTO (α_I and α_{HTO}) obtained by the TD method.

	$D_{e\text{-}I}$ (m^2/s)	$D_{e\text{-}HTO}$ (m^2/s)	α_I (%)	α_{HTO} (%)
CS6	9.0E-14	1.8E-13	0.12	0.43
CS7	1.0E-13	2.2E-13	0.14	0.52
CS8	6.9E-14	1.8E-13	0.12	0.51
Average ± 1σ	$8.7 \pm 1.7\times10^{-14}$	$1.9 \pm 0.2\times10^{-13}$	0.13 ± 0.01	0.48 ± 0.05

2.4. Discussion

The ϕ_w values (Table 2.3) align well with porosity reported in the literature for Lac du Bonnet granite. Maldonado-Sánchez (2020) measured a comparable porosity of 0.4 ± 0.1 % for drill-core samples; Mclaughlin et al. (1998) report an average porosity of 0.36 % based on the work of Katsube and Hume (1987); Stevenson et al. (1996) used a porosity of 0.3 % in their hydrogeological model based on information from previous studies (Chernis and Robertson, 1987; Drury, 1987; Katsube and Hume, 1987) and Fujikawa et al. (1993) used a porosity of 0.2 % reported by Noronha et al. (1990).

The rock capacity factor is a function of ϕ_t, the dry bulk density of the rock (ρ; $g\cdot cm^{-3}$) and the distribution coefficient for sorbing species (K_d; $cm^3\cdot g^{-1}$), and is defined according to Eq. 2.8:

$$\alpha = \phi_t - \rho K_d \quad [2.8]$$

For iodide and HTO, which are generally conservative tracers, $K_d = 0$ and the rock capacity factor, $\alpha = \phi_t$ (Van Loon et al., 2005). Comparison between ϕ_w (Table 2.3) and α_I and α_{HTO} values (Table 2.4) indicates the proportion of the total pore space that is accessible to diffusion of each tracer. The average α_{HTO} value (0.48 ± 0.05 %) is close, but slightly higher, than the maximum ϕ_w value (0.42 ± 0.01 %), but these measurements were not conducted on the

same rock sample so the difference could be explained by heterogeneity in the rock. Nonetheless, this indicates that the total pore space is available for the diffusion of HTO, which is expected because of the similarity between the $^{1}H_2O$ and $^{3}H_2O$ molecules. The average α_I value (0.13 ± 0.01 %) is, however, significantly lower than ϕ_w and α_{HTO}. The ratio of iodide- over HTO-accessible porosity (α_I/α_{HTO}) is 26 %, indicating that only about a quarter of the pore space is available for I^- diffusion and that the remaining 74 % is depleted in I^-. The saturated pore space adjacent to negatively charged mineral surfaces attracts cations, creating a layer, referred to as the diffuse double layer (DDL), that is depleted in anions. This anion-exclusion phenomenon commonly occurs in clay rocks (Van Loon et al., 2003; Wersin et al., 2004; Cavé et al., 2009; Altmann et al., 2012), although studies on intact (Soler et al., 2015) and crushed (Štamberg et al., 2014) granite have also reported some ion-exclusion effects. Nonetheless, anion-exclusion in the Lac du Bonnet granite is more important than expected considering the relatively low abundance of clays in the pores (when compared to clay rocks for example).

One of the goals of this study was to modify the X-ray radiography technique described by Cavé et al. (2009) to minimize sensitivity to image registration errors. In fine-grained, homogenous limestones with a porosity of 2 %, Cavé et al. (2009) noted that instrumental and registration error in measurements could lead to errors of up to 5 % in determination of relative tracer concentration. Maldonado-Sánchez (2020) applied the radiography method, as described by Cavé et al. (2009), to Lac du Bonnet granite with a porosity of 0.4 % and a medium to coarse-grained matrix that is heterogeneous at the measurement scale (10s of mm). The results demonstrated that the registration error becomes prohibitively high, completely masking the diffusion signal (Fig. 2.8). The principal innovation in the present study is the introduction of sample rotation during data acquisition which leads to effective elimination of horizontal

registration errors and significant improvement in the measured diffusion profiles as can be seen by comparing data in Fig. 2.5 with that in Fig. 2.8. In the current study, vertical registration was unnecessary because the position of a selected reference intensity peak in the profiles did not vary by more than one pixel, likely due to precautions taken to avoid moving the sample and stage motors between measurements.

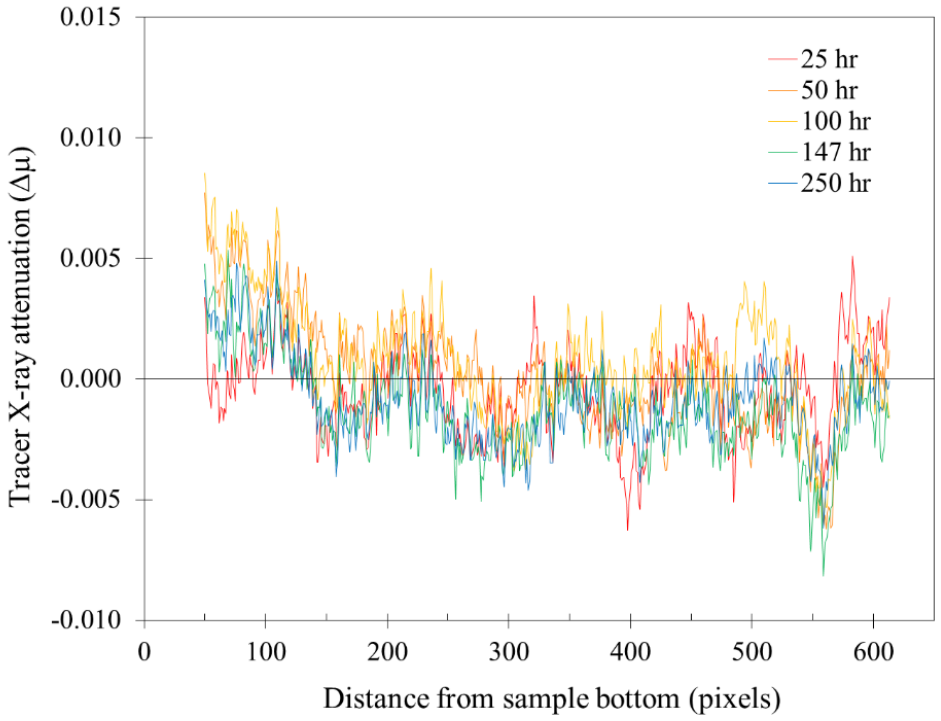

Fig. 2.8. Data from a previous experiment without sample rotation showing the difference in X-ray attenuation (Δμ) profiles during iodide diffusion in Lac du Bonnet Granite; Maldonado-Sánchez (2020).

Through-diffusion is an established method for determining diffusion coefficients and can serve as a benchmark to compare the results of the radiography technique. Cavé et al. (2009) and Loomer et al. (2013a) found very good agreement between radiography and TD results for iodide diffusion in sedimentary rocks. The radiography method provides D_p, and the TD technique provides D_e. To compare the diffusion coefficient estimates of the two techniques, D_p

values obtained from radiography were transformed to D_e values according to the relationships in Table 2.1 by multiplying with α_I determined from the TD experiments (Table 2.4).

The D_e determined for iodide in the Lac du Bonnet granite with the modified radiography method is 3.1×10^{-14} m^2/s, which is 64 % lower than the average value obtained with the TD experiments (8.7×10^{-14} m^2/s; Table 2.4). This difference could be attributable to heterogeneity in the size and distribution of pores in the granite suggesting that the sample measured by radiography may have a slightly lower porosity and/or pore connectivity (lower τ_f). Effective diffusion coefficients for I^-, Cl^- and HTO found in the literature for crystalline rocks are summarized in Table 2.5. The studies selected for comparison were all conducted on granite and tonalite with low porosity (<1 %) using the TD method. For anions I^- and Cl^-, the range of reported values span slightly more than one order of magnitude from 1.0×10^{-14} m^2/s (Siitari-Kaupi et al., 1997) to 2.8×10^{-13} m^2/s (Skagius & Neretnieks, 1986), fully encompassing the range of D_e values obtained with the radiography and TD methods in this study (Fig. 2.9). The D_e values measured for iodide in the Lac du Bonnet granite using the radiography technique are within the range of values reported by Siitari-Kaupi et al. (1997) for Cl^- in tonalite using TD, whereas the values from the TD method in this study are better represented by the range reported by Skagius and Neretnieks (1986) for I^- in granite. The range of D_e values reported by Jokelainen et al. (2009) for Cl^- in granite is higher than the values found for I^- in the Lac du Bonnet granite in this study. The range of D_e values found in the literature is quite large, probably due to heterogeneity in sample properties. In comparison, the difference between the values obtained in this study with the radiography and TD methods is relatively small, lending further confidence to the X-ray method and its application for estimating diffusion in low-porosity crystalline rocks.

Table 2.5. Compilation of ϕ_w and D_e values reported in the literature for I^- , Cl^- and HTO in crystalline rocks.

	ϕ_w (%)	D_e (m^2/s)
This Study, I^- in Granite (Radiography)	0.3 – 0.4 (0.35)	2.7×10^{-14} – 3.6×10^{-14} (3.1×10^{-14})
This Study, I^- in Granite (TD)	0.41 – 0.43 (0.42)	6.9×10^{-14} – 1.0×10^{-13} (8.7×10^{-14})
Siitari-Kaupi et al. (1997), Cl^- in Tonalite	0.2 – 0.3	1.0×10^{-14} – 5.0×10^{-14} (3.0×10^{-14})
Skagius and Neretnieks (1986), I^- in Granite	0.07 – 0.64	4.1×10^{-14} – 4.4×10^{-13}
Jokelainen et al. (2009), Cl^- in Granite	(0.4)	1.3×10^{-13} – 2.8×10^{-13} (1.9×10^{-13})
This Study, HTO in Granite	0.41 – 0.43 (0.42)	1.8×10^{-13} – 2.2×10^{-13} (1.9×10^{-13})
Jokelainen et al. (2009), HTO in Granite	(0.4)	5.3×10^{-13} – 1.3×10^{-12} (8.2×10^{-13})
Siitari-Kaupi et al. (1997), HTO in Tonalite	0.2 – 0.3	3.0×10^{-14} – 1.5×10^{-13} (9.0×10^{-14})

Values in brackets are averages

Although the range of D_e values determined by TD for HTO in this study is broadly comparable to that for iodide, the mean D_e for HTO is almost twice as high as the mean D_e for iodide (Table 2.4). This indicates that HTO diffuses faster through the samples compared to iodide. The τ_f is lower for anions because a portion of the pore space is unavailable to them, resulting in lower diffusivity for negatively charged solutes (Appello & Wersin, 2007). Negatively charged clay particles in the connected pores of the granite, as shown in Fig. 2.3B, contribute to the decreased α_I and τ_f, whereas the entire pore volume is accessible for HTO diffusion. The range of D_e values found for HTO in this study compares well those reported by Siitari-Kaupi et al. (1997) but is lower than the values reported by Jokelainen et al. (2009) (Table 2.5, Fig. 2.9).

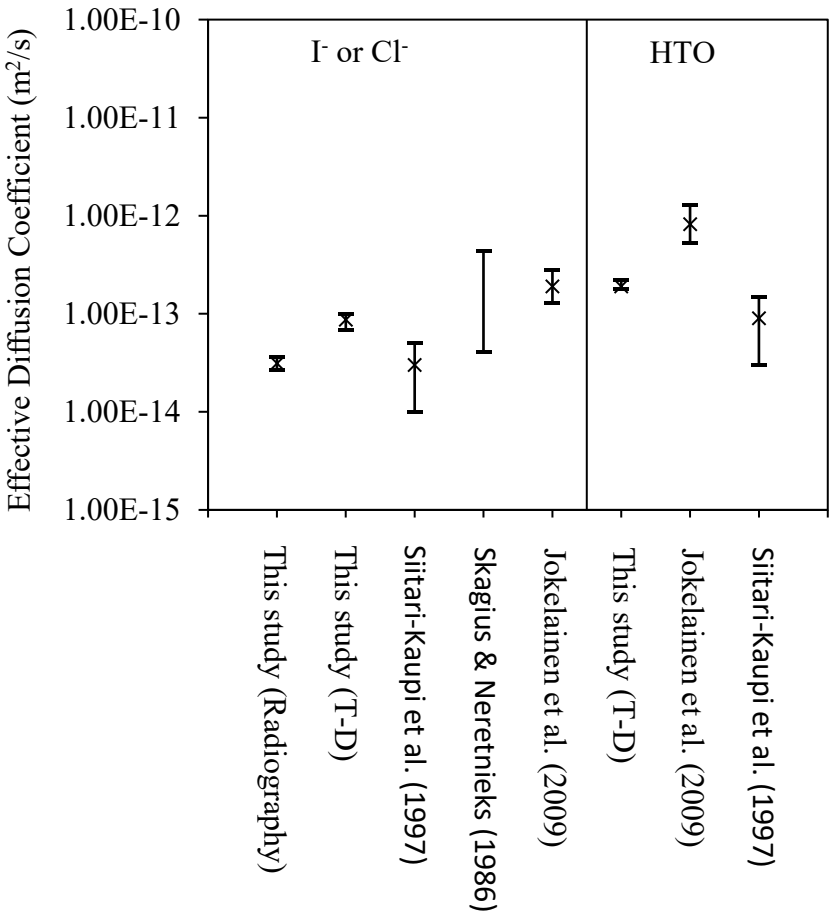

Fig. 2.9. Comparison of D_e values from this study with those reported in the literature for I^- , Cl^- and HTO in crystalline rocks. The vertical bars with brackets represent min-max ranges, and the "x" represent averages.

The modified X-ray radiography method allows for the quantification of solute diffusion in low-porosity, heterogeneous material. However, several factors can affect the repeatability of the experiment and the precision of the results obtained with this method. Voltage fluctuations caused by instability in the electrical grid are common and cause X-ray source variations that affect the intensity of the beam and thereby, the data quality. In this study, the use of a power conditioner minimized the impact of this problem. Furthermore, the intensity of the X-ray beam is affected by the temperature of the source. As the source warms up during use, the beam intensity increases, causing drift in the data. Most of the beam instability effects can be corrected

during data processing steps and noise in the data can be decreased by calibrating the flat-panel detector before acquiring data. The position of the sample relative to the X-ray source and detector affects the precision of repeat measurements at different times, as is a requirement for the difference-imaging method. To limit movements, the base of the diffusion cell was fixed to a motor-controlled rotating stage using a three pin system during data acquisition and the position of the stage, X-ray source and detector were not changed for the duration of the experiment. The sample was also held in place on the diffusion cell using heat-shrink clamps and the cell was handled as little as possible during the experiment to prevent movement.

The scope of this study was limited to testing modifications of the laboratory-based X-ray radiography method (Cavé et al., 2009) in order to apply it to more heterogeneous and less porous materials (compared to shales and limestones). The results obtained were in good agreement with TD test results. However, Ikonen et al. (2016) pointed out that in a granite similar to the one used in this study, about half of the connected porosity determined in the laboratory was due to stress-release in the samples. Stress-induced microcracks in granites have been studied before (Morrow & Lockner, 1997) and their potential to affect porewater chemistry and transport properties has been documented (Waber et al., 2011). A lower in-situ porosity would be associated with a lower τ_f and should result in slower solute transport by diffusion. Therefore, it should be kept in mind that measurements obtained using the radiography method, like other laboratory-based measurements, likely overestimate diffusion coefficients compared to in-situ conditions.

2.5. Conclusion

The X-ray radiography technique was modified to include rotation of the cylindrical samples on the vertical axis during image acquisition, providing horizontally integrated images that eliminate the need for horizontal registration and reduce the error associated with difference imaging. This modification has proven useful in measuring diffusion in heterogenous rocks which would otherwise be challenging to study with the radiography techniques due to the complexity of image registration. The modified technique was tested by applying it in an iodide diffusion experiment with the Lac du Bonnet granite (Manitoba, Canada). The method produced coherent iodide concentration profiles through the transient stage of diffusion and allowed for the successful estimation of a D_e of 3.1×10^{-14} m^2/s. This radiography estimate is 64 % lower than the average D_e obtained form TD measurements (8.7×10^{-14} m^2/s) on a different rock with similar mineralogical and textural characteristics. This difference in D_e values is relatively small compared to the range of values reported in the literature for similar rock types, thus lending confidence to the X-ray method and its application for estimating diffusion in low-porosity crystalline rocks. Future work could aim at expanding the use of this method to study the diffusion of other tracers in heterogeneous rocks or low-porosity materials.

2.6. Acknowledgments

This research was supported by NWMO/NSERC Collaborative Research and Development Grant CRDPJ/ 477852-2014.

2.7. References

Agbogun, H. M. D., Al, T. A., & Hussein, E. M. (2013). Three-dimensional imaging of porosity and tracer concentration distributions in a dolostone sample during diffusion experiments using X-ray micro-CT. *Journal of contaminant hydrology*, *145*, 44-53. https://doi.org/10.1016/j.jconhyd.2012.11.008

Al, T., Xiang, Y., Cavé, L., & Loomer, D. (2010). Measurement of diffusion properties by X-ray radiography and by through-diffusion techniques using iodide and tritium tracers: core samples from OS-1 and DGR-2. In *Technical Report TR-07-17 Revision 3, May 2010. Prepared by University of New Brunswick for Intera Engineering Ltd.*.

Altman, S. J., Uchida, M., Tidwell, V. C., Boney, C. M., & Chambers, B. P. (2004). Use of X-ray absorption imaging to examine heterogeneous diffusion in fractured crystalline rocks. *Journal of contaminant hydrology*, *69*(1-2), 1-26. https://doi.org/10.1016/S0169-7722(03)00153-0

Altmann, S., Tournassat, C., Goutelard, F., Parneix, J. C., Gimmi, T., & Maes, N. (2012). Diffusion-driven transport in clayrock formations. *Applied Geochemistry*, *27*(2), 463-478. https://doi.org/10.1016/j.apgeochem.2011.09.015

Appelo, C. A. J., & Wersin, P. (2007). Multicomponent diffusion modeling in clay systems with application to the diffusion of tritium, iodide, and sodium in opalinus clay. *Environmental science & technology*, *41*(14), 5002-5007. https://doi.org/10.1021/es0629256

Blum, P. (1997). Physical properties handbook: a guide to the shipboard measurement of physical properties of deep-sea cores. ODP Tech Note 26.

Boving, T. B., & Grathwohl, P. (2001). Tracer diffusion coefficients in sedimentary rocks: correlation to porosity and hydraulic conductivity. *Journal of Contaminant Hydrology*, *53*(1-2), 85-100. https://doi.org/10.1016/S0169-7722(01)00138-3

Cavé, L., Al, T., Xiang, Y., & Vilks, P. (2009). A technique for estimating one-dimensional diffusion coefficients in low-permeability sedimentary rock using X-ray radiography: Comparison with through-diffusion measurements. *Journal of contaminant hydrology*, *103*(1-2), 1-12. https://doi.org/10.1016/j.jconhyd.2008.08.001

Chernis, P.J. and P.B. Robertson. (1987). Natural and stress-relief microcracks in the Lac du Bonnet granite. In Geotechnical studies at Whiteshell Research Area (RA-3). CANMET Report, Canada Energy Mines and Resources, Katsube, T.J. and J.P. Hume, Editors, March 1987.

Crank, J. (1975). *The mathematics of diffusion*. Oxford university press.

Descostes, M., Blin, V., Bazer-Bachi, F., Meier, P., Grenut, B., Radwan, J., ... & Tevissen, E. (2008). Diffusion of anionic species in callovo-oxfordian argillites and oxfordian

limestones (Meuse/Haute–Marne, France). *Applied Geochemistry*, *23*(4), 655-677. https://doi.org/10.1016/j.apgeochem.2007.11.003

Drury, M. (1987). Thermophysical properties of rock samples from WNRE boreholes. In Geotechnical studies at Whiteshell Research Area (RA-3). CANMET Report, Canada Energy Mines and Resources, Katsube, T.J. and J.P. Hume, Editors, March 1987.

Emerson, D.W. (1990). Notes on mass properties of rocks – density, porosity, permeability. *Exploration Geophysics*, *21*, 209-216. https://doi.org/10.1071/EG990209

Farquharson, R. B. (1975). Revised Rb–Sr Age of the Lac du Bonnet Quartz Monzonite, southeastern Manitoba. *Canadian Journal of Earth Sciences*, *12*(1), 115-118. https://doi.org/10.1139/e75-012

Fujikawa, Y., Fukui, M., Drew, D. J., & Vandergraaf, T. T. (1993). Analysis of the migration of instantaneously injected cesium in artificial fractures of Lac du Bonnet granite, Manitoba, Canada. *Journal of contaminant hydrology*, *14*(3-4), 207-232. https://doi.org/10.1016/0169-7722(93)90025-N

Gascoyne, M., & Cramer, J. J. (1987). History of actinide and minor element mobility in an Archean granitic batholith in Manitoba, Canada. *Applied Geochemistry*, *2*(1), 37-53. https://doi.org/10.1016/0883-2927(87)90059-X

Gascoyne, M., & Kamineni, D. C. (1992). Groundwater chemistry and fracture mineralogy in the Whiteshell Research Area: supporting data for the geosphere and biosphere transport models. Atomic Energy of Canada Ltd Technical Record, TR-516/COG-92-94. Internal report, available from SDDO, AECL, Chalk River Laboratories.

Idemitsu, K., Furuya, H., Hara, T., & Inagaki, Y. (1992). Migration of cesium, strontium and cobalt in water-saturated inada granite. *journal of nuclear science and technology*, *29*(5), 454-460. https://doi.org/10.1080/18811248.1992.9731551

Ikonen, J., Sardini, P., Jokelainen, L. *et al.* The tritiated water and iodine migration in situ in Grimsel granodiorite. Part I: determination of the diffusion profiles. *J Radioanal Nucl Chem* **310**, 1041–1048 (2016). https://doi.org/10.1007/s10967-016-4890-6

Jakob, A., Pfingsten, W., & Van Loon, L. (2009). Effects of sorption competition on caesium diffusion through compacted argillaceous rock. *Geochimica et Cosmochimica Acta*, *73*(9), 2441-2456. https://doi.org/10.1016/j.gca.2009.01.028

Johansson, H., Siitari-Kauppi, M., Skålberg, M., & Tullborg, E. L. (1998). Diffusion pathways in crystalline rock—examples from Äspö-diorite and fine-grained granite. *Journal of Contaminant Hydrology*, *35*(1-3), 41-53. https://doi.org/10.1016/S0169-7722(98)00114-4

Jokelainen, L., Ikonen, J., Read, D., Hellmuth, K. H., & Siitari-Kauppi, M. (2009). The diffusion of tritiated water, chloride and uranium through granite. *Scientific Basis for Nuclear Waste Management XXXIII, MRS Proceedings*, *1193*, 461-468.

Katsube, T.J. and J.P. Hume. 1987. Pore structure characteristics of granitic rock samples from Whiteshell Research Area. In Geotechnical studies at Whiteshell Research Area (RA-3). CANMET Report, Canada Energy Mines and Resources, Katsube, T.J. and J.P. Hume, Editors, March 1987.

Lee, C. P., Wu, M. C., Tsai, T. L., Wei, H. J., Men, L. C., & Lin, T. Y. (2012). Comparative study on retardation behavior of Cs in crushed and intact rocks: two potential repository host rocks in the Taiwan area. *Journal of Radioanalytical and Nuclear Chemistry*, *293*(2), 579-586. https://doi.org/10.1007/s10967-012-1684-3

Loomer, D. B., Scott, L., Al, T. A., Mayer, K. U., & Bea, S. (2013). Diffusion–reaction studies in low permeability shale using X-ray radiography with cesium. *Applied geochemistry*, *39*, 49-58. https://doi.org/10.1016/j.apgeochem.2013.09.019

Loomer, D., Xiang, Y., & Al, T. (2013). *Investigations of Methods for Quantifying Diffusive Transport Processes in Sedimentary Rock*. Nuclear Waste Management Organization (NWMO). Technical Report NWMO TR-2013-18. Available at <www.nwmo.ca>.

Martin, C. D. (1990). Characterizing in situ stress domains at the AECL Underground Research Laboratory. *Canadian Geotechnical Journal*, *27*(5), 631-646. https://doi.org/10.1139/t90-077

McCrank, G. F. D. (1985). *A geological survey of the Lac du Bonnet batholith, Manitoba* (No. AECL-7816). Atomic Energy of Canada Ltd.

McLaughlin, R. M. (1995). *Boron and strontium isotope study of fluids situated in fractured and unfractured rock of the Lac du Bonnet Batholith, eastern Manitoba* (Doctoral dissertation, McMaster University). http://hdl.handle.net/11375/5789

Miyake, Y., & Tsunogai, S. (1963). Evaporation of iodine from the ocean. *Journal of Geophysical Research*, *68*(13), 3989-3993. https://doi.org/10.1029/JZ068i013p03989

Morrow, C. A., & Lockner, D. A. (1997). Permeability and porosity of the Illinois UPH 3 drillhole granite and a comparison with other deep drillhole rocks. *Journal of Geophysical Research: Solid Earth*, *102*(B2), 3067-3075. https://doi.org/10.1029/96JB03178

Muuri, E., Matara-aho, M., Puhakka, E., Ikonen, J., Martin, A., Koskinen, L., & Siitari-Kauppi, M. (2018). The sorption and diffusion of 133Ba in crushed and intact granitic rocks from the Olkiluoto and Grimsel in-situ test sites. *Applied Geochemistry*, *89*, 138-149. https://doi.org/10.1016/j.apgeochem.2017.12.004

Nakashima, Y. (2000). The use of X-ray CT to measure diffusion coefficients of heavy ions in water-saturated porous media. *Engineering Geology*, *56*(1-2), 11-17. https://doi.org/10.1016/S0013-7952(99)00130-1

NEA (2008), Moving Forward with Geological Disposal of Radioactive Waste, OECD Publishing.

Noronha, C.J., Gureghian, A.B., Vandergraaf, T.T. and Brandstetter, A., (1990). Large block migration experiments interval test case 9. Battelle Memorial Inst., Off. Waste Technol. Dev., Willowbrook, IL, BMI-OWTD-7.

Nunn, J. (2018). *Investigations of partial gas saturation on diffusion in low-permeability sedimentary rocks* (Doctoral dissertation, Université d'Ottawa/University of Ottawa). http://dx.doi.org/10.20381/ruor-22649

Nunn, J. A., Xiang, Y., & Al, T. A. (2018). Investigation of partial water saturation effects on diffusion in shale. *Applied Geochemistry*, *97*, 93-101. https://doi.org/10.1016/j.apgeochem.2018.08.004

Rançon, D. (1988). Comparative study of radioactive iodine behavior in soils under various experimental and natural conditions. *Radiochimica Acta*, *44*(1), 187-194. https://doi.org/10.1524/ract.1988.4445.1.187

Rasband, W.S., 2018. ImageJ, U. S. National Institutes of Health, Bethesda, Maryland, USA, Available online at <https://imagej.net>.

Shackelford, C. D. (1991). Laboratory diffusion testing for waste disposal—A review. *Journal of Contaminant Hydrology*, *7*(3), 177-217. https://doi.org/10.1016/0169-7722(91)90028-Y

Siitari-Kauppi, M., Lindberg, A., Hellmuth, K.H., Timonen, J., Väätäinen, K., Hartikainen, J., Hartikainen, K., (1997). The effect of microscale pore structure on matrix diffusion—a site-specific study on tonalite. *Journal of contaminant hydrology*, *26* (1–4), 147– 158. https://doi.org/10.1016/S0169-7722(97)00011-9

Skagius, K., & Neretnieks, I. (1986). Porosities and diffusivities of some nonsorbing species in crystalline rocks. *Water Resources Research*, *22*(3), 389-398. https://doi.org/10.1029/WR022i003p00389

Soler, J. M., Landa, J., Havlova, V., Tachi, Y., Ebina, T., Sardini, P., ... & Martin, A. J. (2015). Comparative modeling of an in situ diffusion experiment in granite at the Grimsel Test Site. *Journal of contaminant hydrology*, *179*, 89-101. https://doi.org/10.1016/j.jconhyd.2015.06.002

Spiessl, S. M., MacQuarrie, K. T. B., & Mayer, K. U. (2008). Identification of key parameters controlling dissolved oxygen migration and attenuation in fractured crystalline rocks. *Journal of Contaminant Hydrology*, *95*(3-4), 141-153. https://doi.org/10.1016/j.jconhyd.2007.09.002

Štamberg, K., Palágyi, Š., Videnská, K., & Havlová, V. (2014). Interaction of 3 H+(as HTO) and 36 Cl−(as Na 36 Cl) with crushed granite and corresponding fracture infill material investigated in column experiments. *Journal of Radioanalytical and Nuclear Chemistry*, *299*, 1625-1633. https://doi.org/10.1007/s10967-013-2870-7

Stevenson DR, Kozak ET, Davison CC, Gascoyne M, Broadfoot RA (1996) Hydrogeologic characteristics of domains of sparsely fractured rock in the granitic Lac du Bonnet

Batholith, southeastern Manitoba, Canada. Atomic Energy of Canada Limited Report, AECL-11558, COG-96-117, Atomic Energy of Canada Limited.

Tidwell, V. C., & Glass, R. J. (1994). X ray and visible light transmission for laboratory measurement of two-dimensional saturation fields in thin-slab systems. *Water Resources Research*, *30*(11), 2873-2882. https://doi.org/10.1029/94WR00953

Tidwell, V. C., Meigs, L. C., Christian-Frear, T., & Boney, C. M. (2000). Effects of spatially heterogeneous porosity on matrix diffusion as investigated by X-ray absorption imaging. *Journal of Contaminant Hydrology*, *42*(2-4), 285-302. https://doi.org/10.1016/S0169-7722(99)00087-X

Truesdale, V. W. (2007). On the feasibility of some photochemical reactions of iodide in seawater. *Marine Chemistry*, *104*(3-4), 266-281. https://doi.org/10.1016/j.marchem.2006.12.003

Van Loon, L. R., Baeyens, B., & Bradbury, M. H. (2005). Diffusion and retention of sodium and strontium in Opalinus clay: Comparison of sorption data from diffusion and batch sorption measurements, and geochemical calculations. *Applied Geochemistry*, *20*(12), 2351-2363. https://doi.org/10.1016/j.apgeochem.2005.08.008

Van Loon, L. R., Soler, J. M., & Bradbury, M. H. (2003). Diffusion of HTO, 36Cl− and 125I− in Opalinus Clay samples from Mont Terri: Effect of confining pressure. *Journal of Contaminant Hydrology*, *61*(1-4), 73-83. https://doi.org/10.1016/S0169-7722(02)00114-6

Waber, H. N., Gimmi, T., & Smellie, J. A. T. (2011). Effects of drilling and stress release on transport properties and porewater chemistry of crystalline rocks. Journal of hydrology, 405(3-4), 316-332. https://doi.org/10.1016/j.jhydrol.2011.05.029

Wadden, M., & Katsube, T. J. (1982). Radionuclide diffusion rates in igneous crystalline rocks. *Chemical Geology*, *36*(1-2), 191-214. https://doi.org/10.1016/0009-2541(82)90046-8

Wersin, P., Van Loon, L. R., Soler, J. M., Yllera, A., Eikenberg, J., Gimmi, T., ... & Boisson, J. Y. (2004). Long-term diffusion experiment at Mont Terri: first results from field and laboratory data. *Applied Clay Science*, *26*(1-4), 123-135. https://doi.org/10.1016/j.clay.2003.09.007

Widestrand, H., Byegård, J., Cvetkovic, V., Tullborg, E. L., Winberg, A., Andersson, P., & Siitari-Kauppi, M. (2007). Sorbing tracer experiments in a crystalline rock fracture at Äspö (Sweden): 1. Experimental setup and microscale characterization of retention properties. *Water Resources Research*, *43*(10). https://doi.org/10.1029/2006WR005277

Xiang, Y., Al, T., & Mazurek, M. (2016). Effect of confining pressure on diffusion coefficients in clay-rich, low-permeability sedimentary rocks. *Journal of contaminant hydrology*, *195*, 1-10. https://doi.org/10.1016/j.jconhyd.2016.10.004

Xiang, Y., Al, T., Scott, L., & Loomer, D. (2013). Diffusive anisotropy in low-permeability Ordovician sedimentary rocks from the Michigan Basin in southwest Ontario. *Journal of contaminant hydrology*, *155*, 31-45. https://doi.org/10.1016/j.jconhyd.2013.09.002

CHAPTER 3

X-RAY FLUORESCENCE MEASUREMENT OF IODIDE AND CESIUM DIFFUSION AND ION-EXCHANGE IN SHALE

CHARLES CADIEUX, SAMUEL MORFIN, BIRENDRA SAPKOTA, TOM AL

Department of Earth and Environmental Sciences, University of Ottawa, Ottawa, ON, K1N 6N5, Canada

Abstract

Clay-rich rocks are of interest for safe and long-term geological storage solutions for radioactive wastes because of their low permeability and high sorption capacity, which slow down solute migration. Non-destructive X-ray methods have been used to measure diffusion coefficients and sorption properties, but they typically have relatively high detection limits and are limited to studying one ion at a time. Here we present a novel energy dispersive X-ray fluorescence (EDXRF) method that allows for relatively low concentrations, multi-ionic tracers to be studied. The EDXRF method is based on X-ray fluorescence emission by aqueous tracers when they are irradiated as they diffuse through a porous media. The X-ray emission intensity is indicative of tracer concentration, which is determined through calibration, allowing for rapid estimation of diffusion coefficients for multiple ions simultaneously. This method was used successfully to detect simultaneous transport of conservative (0.1M iodide) and reactive (0.1M cesium) ions in sedimentary rock with 11% porosity (Queenston Formation shale, Bruce nuclear site, Ontario, Canada). Transport modelling coupled with parameter estimation software was used to obtain pore diffusion coefficients for iodide and cesium of $6.1 \pm 0.4 \times 10^{-11}$ $m^2 \cdot s^{-1}$ and $9.5 \pm 1.3 \times 10^{-11}$ $m^2 \cdot s^{-1}$, respectively, as well as selectivity coefficient ($\log k_{Na\_Cs}$) of 1.8 ± 0.7 and cation exchange capacity (CEC) of 2.3 ± 0.2 meq/100g for cesium. The Dp values for I and Cs

are similar to those found in literature for the same rock formation, but the logkNa_Cs, and especially the CEC, are different than values from a previous study with the Queenston shale.

3.1. Introduction

As the quantity of radioactive waste derived from nuclear power production increases, research on safe and long-term geological storage solutions garners more interest. Clay and clay-rock formations such as the Boom Clay (Henrion et al., 1985) in Belgium or the Opalinus Clay (Wersin et al., 2004) in Switzerland are often considered as potential hosts for deep geological repositories (DGR) and have been studied extensively because their low permeability and high sorption capacity hinders solute transport. Low permeability is a key attribute for potential host rocks because it limits or prevents groundwater flow and resulting solute transport by advection. However, even in rocks with extremely low permeability, transport by diffusion is still possible so evaluating the suitability of a site to isolate radioactive waste requires quantification of diffusion and sorption properties of the potential host rocks.

Through-diffusion is a common method used to study diffusion at the laboratory scale (Boving & Grathwohl, 2001; Van Loon et al., 2003; Vilks & Miller., 2007; Descotes et al., 2008; Cavé et al., 2009; Xiang et al., 2016). The through-diffusion method, and others that require the establishment of steady-state diffusion (Shackelford, 1991), are well-suited for measurements using non-reactive tracers, but the experimental duration can be very long (years) when reactive (sorbing) tracers are involved (Jakob et al., 2009). With reactive tracers it can be advantageous to measure diffusion coefficients during the transient period by using non-destructive imaging techniques such as computed tomography (Nakashima, 2000) and X-ray radiography (Altman et al., 2004; Cavé et al., 2009; Xiang et al., 2013; Loomer et al., 2013a; Nunn et al., 2018).

Sorption of aqueous solutes on the surface of solids is typically studied using batch reaction experiments where sorption isotherms are produced by monitoring the decrease in solute concentration as disaggregated rock powders are suspended in solutions of varying initial solute concentration to estimate the distribution coefficient (K_d). For a simple linear isotherm (Eq. 3.1), the mass of solute sorbed (S) is a linear function of the initial solute concentration (C) with a slope equal to K_d:

$$S = K_d \cdot C \quad [3.1]$$

Based on these tests, Bradbury and Beayens (2000), building on previous work by Poinssot et al. (1999), proposed a three-site cation exchange model for cesium (Cs) on illite; presumed to be largely responsible for the sorption capacity of argillaceous rocks. Sorption of cations on illite and other minerals has since been studied extensively using batch sorption experiments (Bostick et al., 2002; Van Loon et al., 2005; Fuller et al., 2015; Muuri et al., 2016). However, sorption studies on intact rocks rather than disaggregated samples are of interest because the experimental conditions are closer to in situ conditions and can therefore yield more representative results. In intact rocks, the K_d for specific tracers can be determined using through-diffusion measurements by solving an analytical solution of the diffusion equation, as done by Van Loon et al. (2005) for Na and Sr in Opalinus Clay.

The X-ray radiography method that was developed to study diffusion of non-reactive iodide (I) (Cavé et al., 2009) offers a faster way to estimate transport parameters during the transient diffusion period. Loomer et al. (2013a) used this method to monitor Cs^+ diffusion in intact shale and used the multicomponent reactive transport code MIN3P (Mayer et al., 2002; Bea et al., 2011) to fit the experimental data and determine the porewater diffusion coefficient (D_{p_Cs}), cation exchange capacity (CEC) and selectivity coefficient ($\log k_{Cs\_Na}$) for exchange of

Na^+ for Cs^+ on exchange sites. In contrast with the K_d approach to sorption modelling, the reactive-transport modelling approach using CEC and selectivity coefficients is preferred because it can be implemented in equilibrium geochemical codes that allow for a wide range of reaction processes (e.g. dissolution/precipitation, ion exchange, surface complexation). Simulation of ion exchange in a thermodynamic framework is possible, provided provision is made for assigning activity coefficients for sorbed species. For example, MIN3P and the USGS equilibrium geochemical code PHREEQC use equivalent fractions, known as the Gaines-Thomas convention (Loomer et al., 2013a; Parkhurst & Appelo, 2013). The non-destructive X-ray radiography method used by Loomer et al. (2013) has proved to be effective for quantifying ion exchange of reactive tracers in intact clay rocks. However, one disadvantage of this technique is that it uses a flat-panel detector that counts total X-ray events without discriminating between their energies. The use of an energy-dispersive X-ray spectroscopy (EDS) technique such as X-ray fluorescence (XRF) spectrometry can produce element-specific diffusion data, allowing for monitoring the transport of multiple elements simultaneously in intact rock samples.

Commercially available XRF instruments are not designed for time-series, spatially resolved analysis of intact rock samples. Common benchtop or standalone XRF instruments are specialized in acquiring spectral data from small fusion discs or pressed pellets, both of which require prior crushing and milling of samples. In principle, an XRF data acquisition system is capable of providing spatially resolved tracer concentration measurements in an intact rock, which could then be processed as outlined by Cavé et al. (2009) for non-reactive tracers or Loomer et al. (2013a) for reactive tracers. A customized XRF technique that can be used for non-destructive diffusion studies needs to meet several requirements:

- The acquisition geometry should allow for a relatively large sample to be analyzed.

- The detection limit should be low enough to detect small masses of solutes diffusing inside of a low-porosity rock.
- A reliable calibration method is required to transform the spectral data into relative tracer concentrations.
- The instrument should allow for spatially resolved measurements with mm resolution and high repeatability.

The objectives of this study are to:

- Develop a customized XRF measurement system to acquire concentration profiles of solutes in intact low-porosity geologic media.
- Apply the XRF method to estimate diffusion coefficients for I and Cs simultaneously in shale samples.
- Obtain in-situ estimates of Cs ion-exchange properties (CEC and $\log k_{Cs\_Na}$) for the shale samples.

3.2. Materials and methods

3.2.1. Sample Description

The shale used in this study was sourced from borehole DGR4 located at the Bruce nuclear site, Ontario Canada (Intera, 2011). The Bruce site is located at the northeast margin of the Michigan Basin, on an approximately 850 m thick sedimentary sequence of Paleozoic sandstone, carbonates, shale, and minor evaporites (Al et al., 2015). The diffusion samples were collected at 491 m-depth from the Ordovician Queenston Formation shale. The grey-green shale is composed of clay minerals (50–60%), carbonates (30–40%) and quartz (approximately 10%)

(Xiang et al., 2013). Hydraulic packer testing of the Ordovician shale (Beauheim et al., 2014) indicates very low hydraulic conductivity (K) in the range 10^{-16} to 10^{-14} m s^{-1}).

3.2.2. Synthetic porewater and tracer solutions

The natural porewater of the Queenston Formation has a high ionic strength consistent with halite-saturated Silurian evaporated seawater origin (Brennan & Lowenstein, 2002; Lowenstein et al., 2003; Clark et al., 2013). A synthetic porewater (SPW), similar to the shale SPW reported by Xiang et al. (2013), was used to saturate the samples intended for porosity measurements ("Full strength"; Table 3.1), but the Na content of the SPW used for the diffusion experiments was decreased ("NaCl 1.5 mol; Table 3.1) to prevent halite precipitation. A multi-tracer solution (Table 3.1) used to analyze simultaneous diffusion of multiple elements was prepared by replacing NaCl and $CaCl_2$ by NaI, CsCl and $SrCl_2$. Oxidation of I^- to volatile I_2 (Truesdale, 2007) in the tracer solution was inhibited by addition of 0.5 mL of thiosulfate solution (1M $Na_2S_2O_3$), an I_2 reducing agent (Rançon, 1988).

Table 3.1. Composition of SPW and tracer solutions (mol/L) used in XRF diffusion experiments.

	Full strength	NaCl 1.5 mol	Tracer
Na	2.4	1.5	1.4
K	0.5	0.5	0.5
Ca	1.202	1.202	1.102
Mg	0.25	0.25	0.25
Cl	5.802	4.902	4.802
S(6)	0.001	0.001	0.001
I	0	0	0.1
Cs	0	0	0.1
Sr	0	0	0.1

3.2.3. Sample preparation

The shale samples used in this study were obtained from a 101.6 mm diameter and 30 mm thick disk-shaped core section. Three 30-mm-long × 20-mm-diameter cylinder-shaped subcores were obtained from the larger disk using a drill press equipped with a diamond bit. The

fragile shale core disk was placed on a soft piece of fabric during drilling and compressed air was used to cool the bit and clear the cuttings. The subcores were prepared for diffusion measurements by sanding with 400 grit sandpaper to flatten the ends of the cylinders and ensure they were perpendicular to the core axes.

3.2.4. Mineralogy

Offcuts from the drilling of sub cores were used for preparation of polished thin sections. Thin sections were prepared parallel to the diffusion direction and normal to bedding. Initial grinding to flatten the section was done with water and polishing was completed with mineral oil to prevent dissolution of soluble minerals. The thin section was carbon-coated and rock-structure and mineralogical data along the diffusion path were acquired with SEM-EDS at the University of Ottawa. The SEM-EDS analyses were performed at an accelerating voltage of 20 kV on a JEOL 6610LV series instrument equipped with an Oxford Inca EDS elemental analysis system.

3.2.5. Water-accessible porosity

Offcuts from the drilling of sub cores were used for water-accessible porosity (ϕ_w) measurements following an established method (Al et al., 2010; Loomer et al., 2013a,b; Xiang et al., 2013), which is consistent with that of Blum (1997) and Emerson (1990). The shale samples were delivered in a partially saturated condition, so they were dried at 105 °C, while monitoring the sample mass periodically over 8 days until a final stable dry mass was recorded. The samples were then clamped between 2 disks of acrylic, with the force exerted perpendicular to bedding to prevent expansion while they were re-saturated by enclosing them in a sealed chamber containing a dish of deionized water to allow transfer of water vapour into the pore space. They were maintained in this condition until they were visibly wet at the surface, at which point they

were immersed in SPW under vacuum for 7 days prior to measuring the saturated mass and submerged mass, which were used to calculate the volume of voids (Eq. 3.2), the bulk rock volume (Eq. 3.3) in order to determine ϕ_w (Eq. 3.4):

$$V_{voids} = \frac{m_{sat} - m_{dry}}{(1 - w_{SPW})\rho_{SPW}} \quad [3.2]$$

where V_{voids} is the volume of voids in the sample (cm^3), m_{sat} is the mass of the saturated sample (g), m_{dry} is the mass of the dry sample (g), w_{SPW} is the mass fraction of solutes in the SPW and ρ_{SPW} is the density of the SPW ($g \cdot cm^{-3}$),

$$V_{rock} = \frac{m_{sat} - m_{sub}}{\rho_{SPW}} \quad [3.3]$$

where V_{rock} is the bulk sample volume (cm^3) and m_{sub} is the mass of the submerged saturated sample (g).

$$\phi w = \frac{V_{voids}}{V_{rock}} \quad [3.4]$$

3.2.6. Diffusion cells

For the XRF experiment, the cylindrical samples were saturated as described above for (ϕ_w) measurements and then mounted on an acrylic pedestal above a solution reservoir equipped with two injection holes (Fig. 3.1). The diffusion influx boundary of the rock core was in direct contact with the solution except for a 2-mm wide peripheral rim on the pedestal. A thin disk of felt fabric was placed on top of the samples to maintain saturation with SPW by capillarity at the upper boundary. An aluminum cap containing a threaded hole to allow injection of SPW was placed on top of each sample. The injection hole was closed with a nylon screw except to add

fresh SPW every 1-3 days during the diffusion experiment. A thin layer of silicone sealant was brushed on the peripheral surface of the rock cores and the aluminum cap and then plastic heat-shrink tubing was used to tightly seal the peripheral surfaces and hold the sample and aluminum cap assembly on the pedestal. The silicone sealant prevented diffusion pathways between the rock sample and the heat-shrink tubing. A tight-fitting metal ring was slipped over the outer surface of the heat-shrink tubing to seal the tubing against an o-ring on the outer surface of the pedestal. The metal also served as a positioning reference during X-ray measurements. Following assembly, the solution reservoir and the felt at the top of the sample were saturated with SPW and the diffusion cells were stored in an airtight container containing an open vessel of SPW in order to maintain an equilibrium vapour pressure and prevent evaporation.

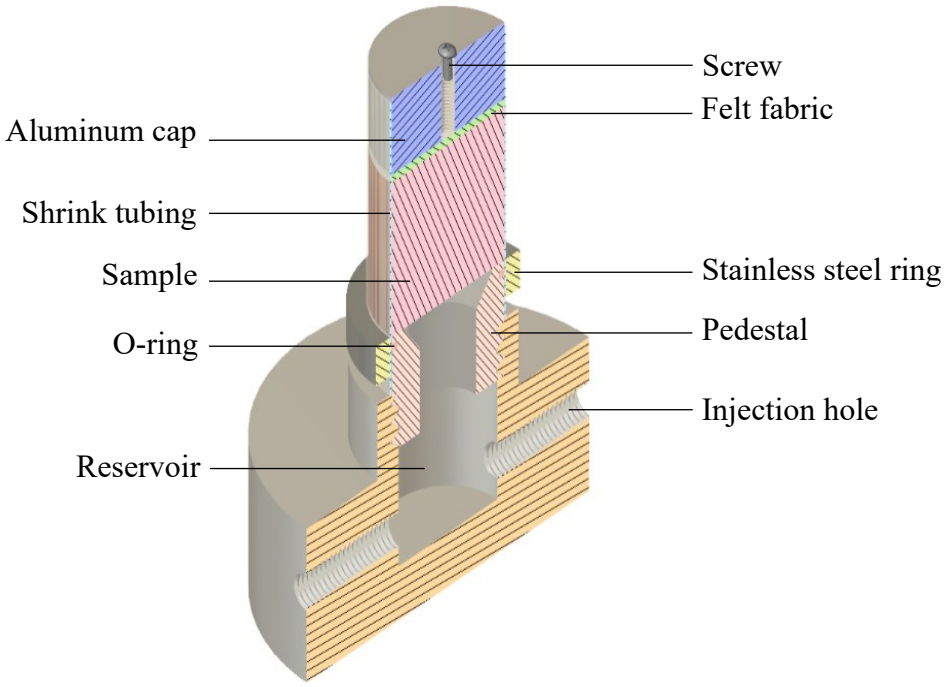

Fig. 3. 1. Cross-section of a diffusion cell used in the experiments.

3.2.7. Data acquisition

At time t = 0, SPW in the reservoir below the sample was replaced by tracer solution, which was then refreshed every 1-3 days during the experiment. The XRF measurements were conducted using a custom-built instrument from Pinnacle X-ray Systems (Atlanta, Georgia) equipped with a 3 kW X-ray source (Varian NDI-160-22) (Fig. 3.2) coupled to a Gulmay® CPL series (CP2-1402) 3000 W generator. Spectrometry measurements were conducted with a thermoelectrically-cooled solid-state silicon drift detector (1 mm thick XR100 FastSDD® from Amptek®) and a PX5 Digital Pulse Processor – Multi-channel Analyzer (DPP-MCA). The X-ray beam was collimated with a 1 mm aperture and the detector was equipped with a 25 mm^2 external multilayer collimator (eMLC2 from Amptek®). The effective spatial resolution (ESR) for the measurements was determined using an edge response (ER) technique as outlined by Agbogun et al. (2013). Briefly, the technique involves acquiring data in a line profile across the boundary of a sharp discontinuity. In this study, a copper (Cu) strip placed on the sample served as the contrasting material, and the ESR was found to be 1.1 mm, corresponding to an ER rise from 5% to 98% of the maximum Cu fluorescence signal. The detector energy scale was calibrated on the Sr Kα (14.17 keV) and Ba Kα (31.19 keV) lines, both of which are naturally occurring in the Queenston shale. The samples were mounted on a Velmex rotational stage (B5990TS) and a Velmex BiSlide (PK245-01AA) which, respectively, allow rotation, as well as vertical and horizontal motion in a plane orthogonal to the X-ray beam. Starting at the base of the sample, spectra were acquired over a 180 second counting period while the sample rotated three times around its vertical axis. The stage was then lowered by 1 mm and the process repeated until spectra had been acquired along the entire height of the sample. The X-ray beam (80 kV and 20 mA) was hardened with a 0.63-mm Cu filter (see Appendix C for details).

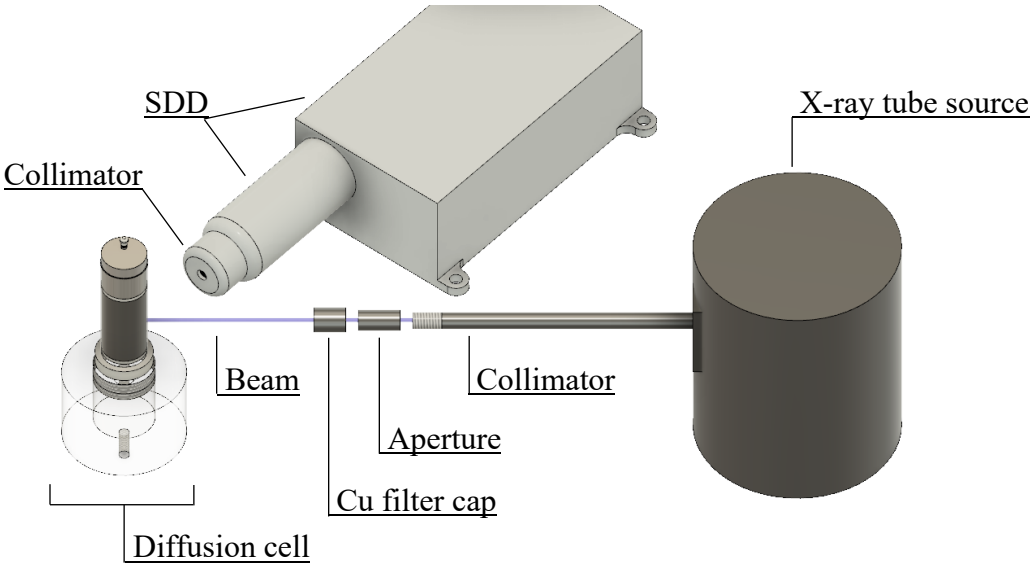

Fig. 3.2. Experimental XRF set up used to acquire diffusion data.

3.2.8. Calibration

Standards were prepared using a conventional pressed-pellet approach for XRF calibration. Queenston Formation shale from a similar depth as the sample used in the diffusion experiments was crushed and dried in the oven at 105 °C before being pulverized in a ball mill. Salts containing the diffusion tracers Cs and Sr (CsCl and $SrCl_2$) were mixed quantitatively with pulverized shale, paraffin binder was added (10% w/w) and then compacted into solid pellets using a 25-tonne hydraulic press to make standards of variable, known concentrations. The standards were analyzed using the same instrument parameters and geometry used for the diffusion experiment. Amptek® XRS-FP2 software was used to produce calibration curves relating tracer-specific X-ray peak intensities (counts/second, or CPS) to tracer porewater-equivalent concentrations (C_{pw}) in the standards, which can be calculated with Eq. 3.5:

$$C_{pw} = \frac{n_t}{V_{voids}} \quad [3.5]$$

where n_t is the number of moles of tracer (mol) in the standard. The V_{voids} is calculated according to Eq. 3.6 using the porosity of the standard (ϕ_s, Eq. 3.6.1):

$$V_{voids} = \phi_s \cdot V_s \quad [3.6]$$

$$\phi_s = 1 - \frac{m_g / \rho_g}{V_s} \quad [3.6.1]$$

where V_s is the total standard volume (cm^3), m_g is the mass of pulverized rock grains (g) and ρ_g is the grain density ($g \cdot cm^{-3}$).

In order to determine the equivalent aqueous concentration of tracer in the samples (C_t) corresponding to the C_{pw} in the standards, a scaling factor has to be applied to account for the bulk density and porosity difference between the standards and the intact rock samples.

There are two attenuation coefficients commonly considered when describing the attenuation of X-rays in materials, the linear attenuation coefficient (μ) and the mass attenuation coefficient (μ/ρ) – ρ being the material density. The former is a measure of photon attenuation per unit distance in the material (commonly cm^{-1}) and the latter is a measure of attenuation per unit mass (commonly cm^2/g). Given that the elemental (mineralogic) constituents of the standards and the samples are essentially the same (other than the paraffin binder), μ/ρ of the mineral constituents in the standards (μ_s/ρ_s) should be the same as those of the intact rock (diffusion samples) (μ_r/ρ_r) (Eq. 3.7):

If $$\frac{\mu_s}{\rho_s} = \frac{\mu_r}{\rho_r} \quad [3.7]$$

then $$\frac{\mu_s}{\mu_r} = \frac{\rho_s}{\rho_r} \quad [3.7.1]$$

and $$\mu_r = \frac{\mu_s}{(\rho_s \,/\, \rho_r)} \quad [3.7.2]$$

Calibration requires that a given fluorescence intensity from the sample be equated with the same fluorescence and corresponding known tracer concentration in the standard, and fluorescence intensity is directly proportional to photon attenuation in the materials. Given that μ is a measure of the attenuation per unit distance in a sample, this means that for an equivalent attenuation in both the standard and the sample, the X-ray path length is a factor of (ρ_s/ρ_r) shorter in the rock sample, and it follows that, in three-dimensions, the X-ray interaction volume (V_I) is smaller in the rock sample also by the same factor. Therefore, because μ/ρ is the same in the standards and the intact rock samples, but V_I is smaller in the rock samples, the C_{pw} must be scaled by a factor of **(ρ_r/ρ_s)**.

The standards and the rock samples also have different porosities, and because the C_{pw} is calculated relative to ϕ_s (Eq. 3.5 and 3.6), it must be scaled by a factor of **(ϕ_s/ϕ_w)** to account for the porosity difference and determine C_t.

The density and porosity scaling factors are combined in Eq. 3.8 to derive the corresponding C_t :

$$C_t = C_{pw} \cdot \frac{\rho_r}{\rho_s} \cdot \frac{\phi_s}{\phi_r} \quad [3.8]$$

3.2.9. Data analysis

Amptek® XRS-FP2 software was used to obtain tracer-specific X-ray peak intensity values from the spectral data acquired during tracer diffusion. The pressed-pellet standards were used to derive C_t values for I and Cs in the samples from the fluorescence intensities. As shown by Cavé et al. (2009) and Loomer et al. (2013a), the pore diffusion coefficient (D_p) for I was determined using a least-squares regression fit approach with an analytical solution to Fick's second law (Crank, 1975):

$$\frac{C_{(x,t)}}{C_0} = \operatorname{erfc}\left[\frac{x}{2 \cdot \sqrt{D_p \cdot t}}\right] \quad [3.9]$$

valid for the following boundary conditions:

$$C(x,t) = 0 \begin{cases} t = 0 \\ x > 0 \end{cases}$$

$$C(x,t) = C_0 \begin{cases} t \geq 0 \\ x = 0 \end{cases}$$

$$C(x,t) = 0 \begin{cases} t \geq 0 \\ x = L \end{cases}$$

where C is the concentration of the tracer at position x (m) along the diffusion path and at time t (s) since the start of diffusion; C_0 is the constant concentration of the tracer at the influx boundary, L is the sample length (m); and D_p is the pore diffusion coefficient (m^2/s), which, by including constrictivity (δ) and tortuosity (τ) terms, accounts for the 3-dimensional variations in pore size and orientation of the pore spaces and interconnecting pore throats (Eq. 3.10):

$$D_p = D_0 \cdot \frac{\delta}{\tau} \quad [3.10]$$

or $$D_p = D_0 \cdot \tau_f \quad [3.10.1]$$

where D_0 is the free-water diffusion coefficient ($m \cdot s^{-2}$) and τ_f is the tortuosity factor. The bottom of the samples (x = 0), which was masked by the stainless steel ring, was also identified using a least-squares regression fit approach.

The multicomponent reactive transport code MIN3P (Mayer et al., 2002; Bea et al., 2011) was used to simulate the coupled processes of Cs diffusion and ion exchange following the method described by Loomer et al. (2013a). Briefly, the parameter estimation code, PEST v.17 (Doherty, 2010) was used to iteratively change the reactive transport code's parameters to obtain the best fit between simulated and experimental Cs concentrations. The one-dimensional transport domain was divided into 1-mm cells along the sample length to match the 1-mm increments for XRF spectral acquisition. Three parameters were optimized simultaneously: D_{p_Cs}, $\log k_{Na\_Cs}$ and CEC. The measured ϕ_w was used in modelling because it is generally assumed to be fully accessible to cations. The hydraulic head was set to 0 at both boundaries (no advective transport). The D_p cannot be adjusted directly in MIN3P and instead, τ_f can be adjusted and used to re-calculate D_p (Eq. 3.10.1). The samples were treated as homogeneous material and initial values for τ_f, CEC and $\log k_{Na\_Cs}$ were assigned to the model domain and then optimized with PEST for all selected time-series datasets simultaneously to obtain estimates of these transport and ion-exchange parameters for Cs in each sample.

3.3. Results

3.3.1. Mineralogy

Shales are often considered to be homogenous rocks in terms of mineralogy and grain size. However in this case, an optical image (Fig. 3.3A) from a thin section reveals noticeable vertical veining as well as some dark and light horizontal bands. Analysis by SEM-EDS confirms that the brown veins consist of a dense matrix of calcite with clays infilling the large intergranular porosity (Fig. 3.3B, 3.3C). The surrounding areas are much finer in texture and comprised of a higher proportion of clays, likely mostly illite, as well as some calcite and dolomite grains (Figure 3.3D, 3.3E). Compositional differences between the various horizontal bands in the fine matrix could not be confirmed with SEM analysis alone. Pore space in the shale is indicated by the black areas in the backscattered electron (BSE) images. Only the largest pores (down to a few μm in diameter) are resolved in the BSE images. Some of the largest voids may result from plucking of mineral grains during grinding and polishing as well as cracking during drilling. Microporosity in clays and other minerals could be important but it cannot be resolved with SEM.

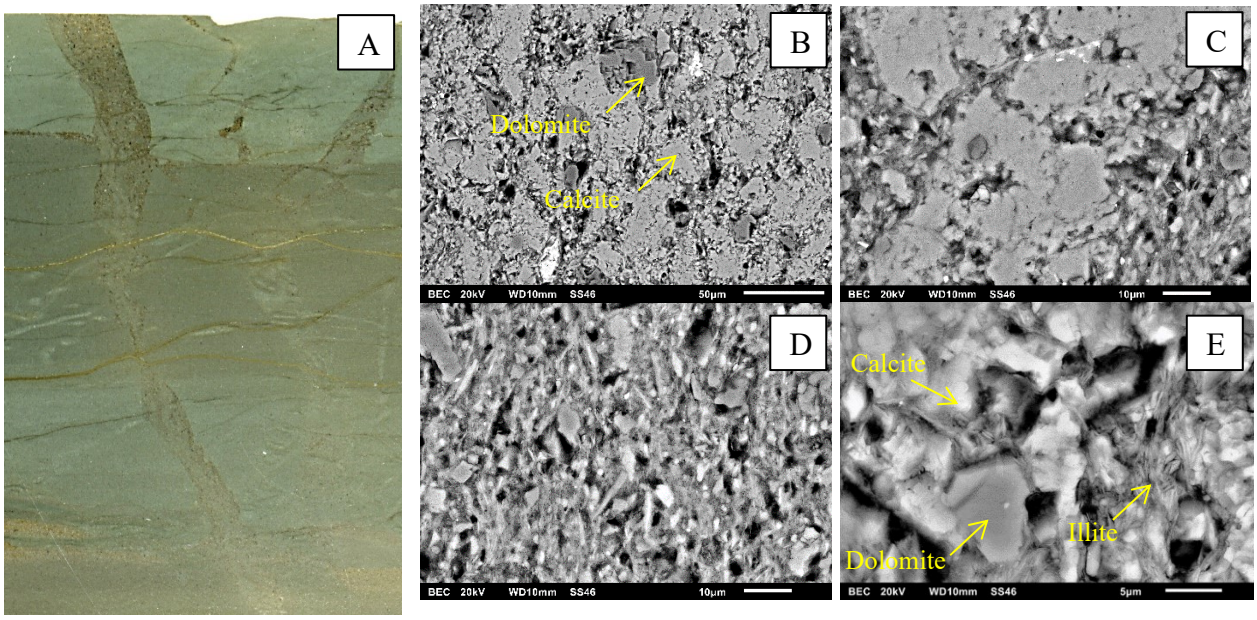

Fig. 3.3. Polished section of Queenston shale – [A] Optical image of the thin section (16.5 mm wide, 25.0 mm high) [B] BSE image of coarse matrix [C] Coarse matrix (higher magnification) [D] Fine matrix [E] Fine matrix (higher magnification).

3.3.2. Porosity

The ϕ_w of the subsamples of Queenston shale ranges from 10.1 to 12.6% with an average of 11 ± 1% (Table 3.2).

Table 3.2. Results obtained from the porosity measurements.

Sample	ϕ_w (%)
1	10.3
2	12.6
3	10.1
Average	11 ± 1

3.3.3. Calibration and data Analysis

Examples of the spectral data are shown in Fig. 3.4. The spectra from the calibration standards (Figure 4A) display an increasing area under the curve for the I Kα and Cs Kα peaks in order of increasing tracer content. The area under the curve for the I and Cs peaks in standard 1 (lowest concentration) are not noticeably above the blank spectrum (pellet without tracer),

indicating that the mass of tracer is at or below the limit of detection in these conditions. The diffusion sample data (B) also show a defined increase between each acquisition time, which corresponds to an increasing tracer mass 7 mm from the influx boundary, suggesting that the tracers are migrating through the sample. The I peaks in the standards are consistently smaller compared to the Cs peaks, which is expected because the concentration of I added to the standards is lower. In the diffusion sample, the overall I peaks are also smaller, but the difference in size between the I and Cs peaks appear to be increasing with each acquisition time, implying that the I concentration in the sample is increasing slower than Cs at that distance from the influx boundary.

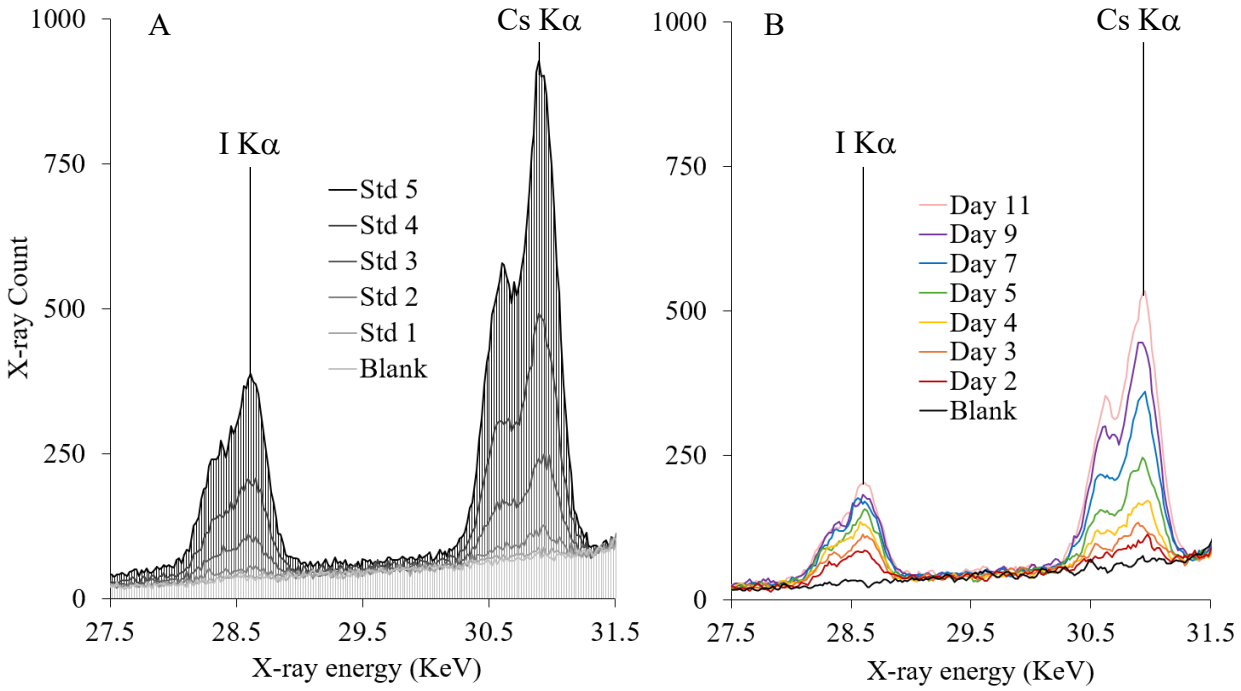

Fig. 3.4. Spectral data in the energy region encompassing the I Kα and Cs Kα peaks for [A] the pressed pellet standards (each spectrum an average of three repeat measurements) and [B] in sample QS1 at a 7-mm distance from the influx boundary (plotted as 3-point moving averages).

Calibration curves relating tracer-specific X-ray peak intensities (in CPS) to C_{pw} and C_t in the standards and samples, respectively are shown in Fig. 3.5. The calibration data yield very good linear regression fit ($R^2 > 99.3\%$) with intercepts corresponding to the constant background X-ray signal.

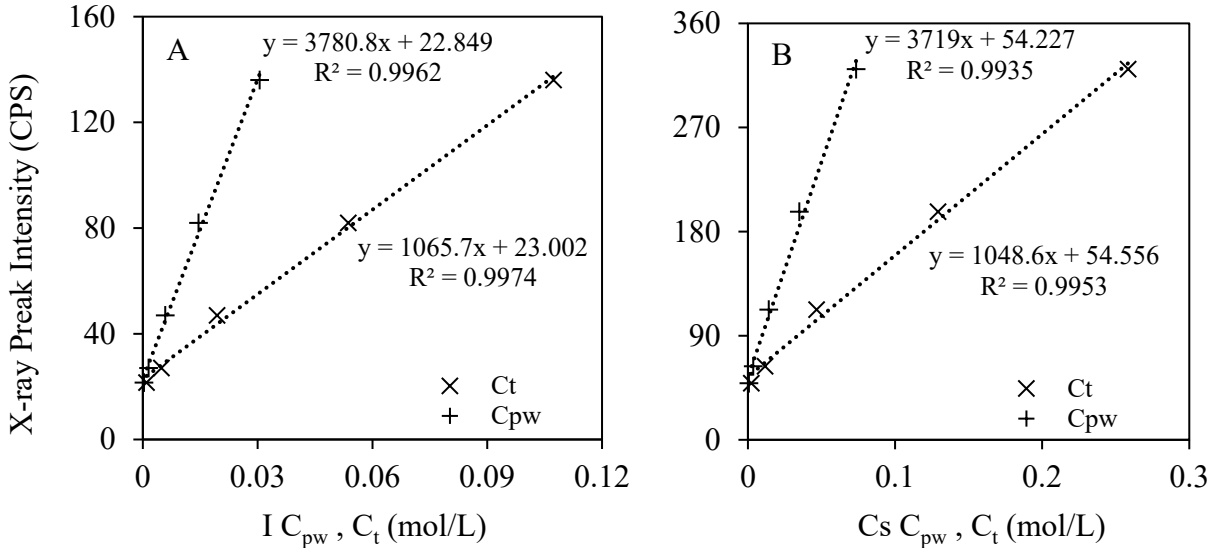

Fig. 3.5. Calibration curves for I [A] and Cs [B] in pressed pellet standards relating X-ray intensity to the C_{pw} in the standards (+ symbols) and the scaled C_t in the samples (× symbols).

X-ray fluorescence spectra were acquired during the transient phase of the diffusion experiment with a multi-element tracer containing I and Cs (Table 3.1). Relative concentration profiles derived from the calibrated spectra are presented in Fig. 3.6, with the diffusion direction from left to right, and the left side of each plot (distance = 0) corresponding to the tracer-influx boundary. Data for the first 5 mm of the sample domain which includes the earliest acquisition times (day 1 for I and days 1-4 for Cs) were not used for the modelling because of partial masking by the stainless-steel ring and potential for artifacts caused by secondary X-rays from I and Cs in the tracer reservoir. The symbols represent the experimental data, and the solid lines

are modelled curves. The data for I and Cs show consistent penetration of tracers with time and the I profiles fit well to the solution (Eq. 3.9) for one-dimensional diffusion of a non-reactive tracer. The curves for Cs display distinct deviations from the non-reactive diffusion profiles, with C/C_0 values at the influx boundary well above 1.0 (4.0), indicating accumulation of Cs in the rock. The diffusion rate for Cs is also slower than for I, with no breakthrough after 18 days whereas I reaches the top boundary after about 11 days. The best-fit values for D_p, $\log k_{Na\_Cs}$, and CEC are listed for the three samples (Table 3.3). The $D_{p\text{-}I}$ ranges from 5.7×10^{-11} to 6.5×10^{-11} $m^2\cdot s^{-1}$ (average ± 1σ = $6.1 \pm 0.4\times10^{-11}$ $m^2\cdot s^{-1}$), lower than the $D_{p\text{-}Cs}$, which ranges from 8.4×10^{-11} to 1.1×10^{-10} $m^2\cdot s^{-1}$ ($9.5 \pm 1.3\times10^{-11}$ $m^2\cdot s^{-1}$). The CEC values are within a range of 1.2 to 2.5 meq/100g (1.8 ± 0.7 meq/100g) and the $\log k_{Na\_Cs}$ values range from 2.2 to 2.5 (2.3 ± 0.2).

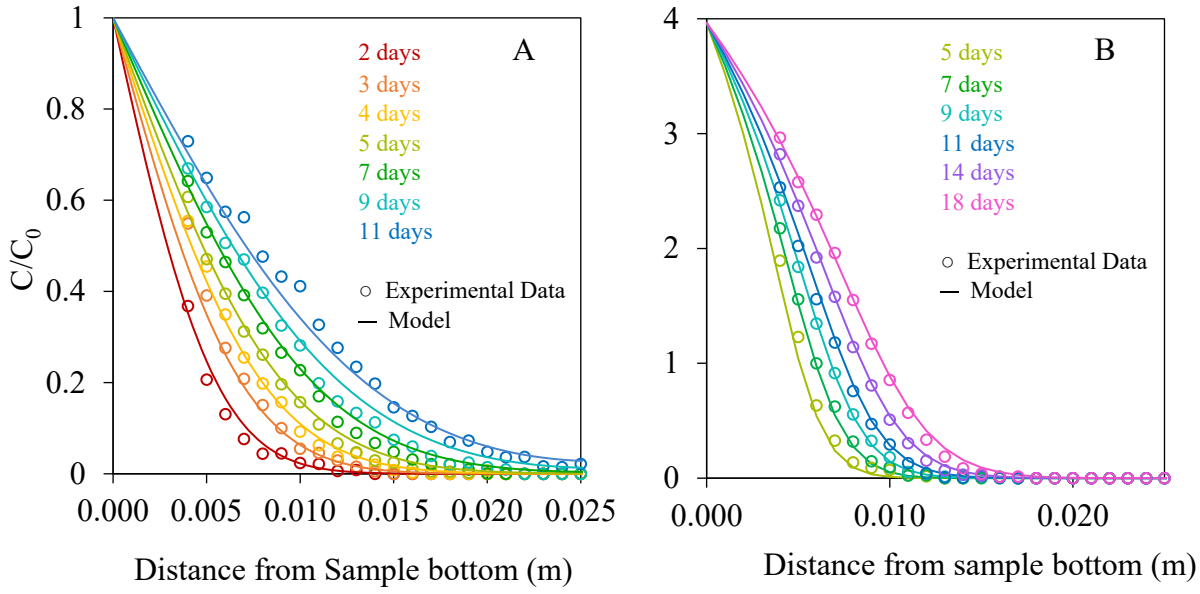

Fig. 3.6. Example diffusion profiles for I (A) and Cs (B) for sample QS1 at different measurement times after injection of the tracer solution.

Table 3.3. Summary of D_{p_I} , D_{p_Cs}, CEC and $logk_{Na\_Cs}$ in Queenston shale

Sample	D_{p_I} ($m^2 \cdot s^{-1}$)	D_{p_Cs} ($m^2 \cdot s^{-1}$)	CEC (meq/100g)	$logk_{Na\_Cs}$
QS1	6.5×10^{-11}	8.4×10^{-11}	1.7	2.3
QS2	5.7×10^{-11}	9.1×10^{-11}	2.5	2.2
QS3	6.1×10^{-11}	1.1×10^{-10}	1.2	2.5
Average ± 1σ	$6.1 \pm 0.4\times10^{-11}$	$9.5 \pm 1.3\times10^{-11}$	1.8 ± 0.7	2.3 ± 0.2

3.4. Discussion

The ϕ_w of the Queenston shale varies spatially within the formation. Xiang et al. (2013) report ϕ_w values from different depths and borehole locations ranging from 5.8 to 10.9 % (mean = 8.6 %, σ = 1.6 % , n = 13). Data for ϕ_w from other studies include 6.2 % (Cavé et al., 2009), 6.6 % (Vilks et al., 2007), 10 to10.3 % (Nunn et al., 2018) and 10.8 % (Barone et al., 1989). The ϕ_w values determined in this study (mean 11 ± 1 %; Table 2) are consistent with, but at the upper end of the range of values reported in the literature.

In clay-rich rocks such as shales, the accessible porosity for anionic solutes is generally lower than ϕ_w due to anion-exclusion effects (Melkior et al., 2004; Van Loon et al., 2003). Xiang et al. (2013) report iodide-accessible porosity (ϕ_I) values for the 13 samples of Queenston shale noted above and the values range from 4.2 to 9.4 % (mean = 5.7 %, σ = 1.5 % , n = 13). The corresponding ratios of iodide- to water-accessible porosity range from 0.54 to 1.04 (mean = 0.66), similar to 0.44 reported by Al et al. (2010) 0.52 (Vilks et al., 2007), 0.55 (Nunn et al., 2018) and 0.70 (Loomer et al., 2013a) (Table 3.5). Cavé et al. (2009) determined ϕ_I for Queenston Formation shale using X-ray radiography imaging of iodide-saturated samples. They found values of 6 % for ϕ_I compared to 6.2 % for ϕ_w, equating to an iodide accessible ratio of 0.97. In this study, we followed a similar method to that of Cavé et al. (2009) except XRF was used instead of X-ray radiography. The XRF data were acquired when the pore fluid was fully

saturated with I (concentration in the pores = C_0), and collecting data in the same manner as for the spatially resolved diffusion profiles, the fluorescence intensities (Int_x; CPS) were acquired at incremental points along the sample length. Spatially resolved values for ϕ_I were then calculated (Eq. 3.11.1) from the ratio of the intensities from the saturated sample to the intensity at C_t = 0.1M (Int_{100}) obtained from the regression equation of the calibration data (Fig. 3.5A), which represents fully iodide-saturated pores with a porosity equal to ϕ_w.

$$\frac{\phi_I}{\phi_w} = \frac{\mathrm{Int_x}}{\mathrm{Int_{100}}} \qquad [3.11]$$

so

$$\phi_I = \frac{\mathrm{Int_x}}{\mathrm{Int_{100}}} \cdot \phi_w \qquad [3.11.1]$$

The ϕ_I values vary slightly along the length of the samples and an increase is observed toward the top of all samples (Fig. 3.7). All three sub cores were drilled from a single disk of drill core, and all are oriented with the sub core axis perpendicular to bedding, so these data provide an indication of the natural variability in ϕ_I laterally and across the bedding planes. Bedding is evident in the thin-section image (Fig. 3.3) and it's likely that the trend to higher ϕ_I values at the top of the sample correspond to higher porosity in the light grey-green unit observed in the image. The values of ϕ_I in the profiles (Fig. 3.7) vary from 10.6-11.4 %, with an average of 10.9 % (Table 3.4), essentially the same as the average of the measured values for ϕ_w (Table 3.2). Similar to the results reported by Cavé et al. (2009), this suggests that there is little or no anion exclusion in these samples of Queenston shale, however this is inconsistent with results from other studies (Table 3.5).

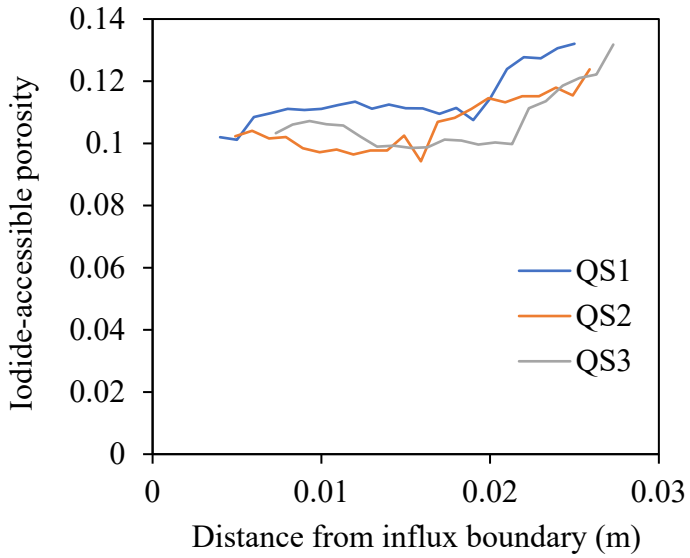

Fig. 3.7. Spatial variations in ϕ_I for Queenston shale samples.

Table 3.4. Average ϕ_I in Queenston shale samples.

Sample	Average ϕ_I
QS1	0.114
QS2	0.106
QS3	0.107
Average ± 1σ	0.109 ± 0.004

The D_{p_I} estimates (Table 3.3) are consistent with the range of values reported in literature for the Queenston shale (Nunn et al., 2018; Xiang et al., 2013; Cavé et al., 2009), but they are slightly higher than some estimates (Loomer et al., 2013a; Vilks et al.; 2007) (Table 5). The D_{p_Cs} values are also similar, but higher than the range of values reported by Loomer et al. (2013a). The estimated D_p for Cs is also higher than for I, with a D_{pI}/D_{pCs} ratio of 0.64. Typically, diffusivity is inversely proportional to solute mass. However, the opposite is observed here, likely due to hindered diffusion of I caused by the large quantity of clays in the shale (Fig. 3.3). Although this is not supported by the ϕ_I results (Fig. 3.7; Table 3.4), negatively charged

clay particles, which are abundant in shale, would typically contribute to a decreased anion-accessible porosity, and thereby, diffusivity, whereas the entire pore volume is accessible for cation diffusion. Loomer et al. (2013a) also report a higher D_p for Cs (7.6×10^{-11} m^2/s), with a slightly lower $D_{p\text{-}I}/D_{p\text{-}Cs}$ ratio of 0.5.

Despite the difference in $D_{p\text{-}I}$ and $D_{p\text{-}Cs}$ suggesting that Cs travels faster than I in the samples, overall Cs transport is retarded by its adsorption onto clay particles. The mineralogy of the Queenston formation shale is known to comprise of 50-60% clays (mostly illite), with the rest consisting of carbonates and quartz (Xiang et al., 2016; Koroleva et al., 2009; Barone et al., 1989). Observations from the SEM analysis (Fig. 3.3) of the present samples are consistent with these previous studies and show that clays are present virtually everywhere between detrital grains and authigenic carbonates, suggesting that sites for Cs sorption are uniformly distributed. Bradbury and Beayens (2000) suggested that the presence of illite is mainly responsible for the sorption capacity of argillaceous rocks. Sorption of cations on illite and other minerals has since been studied extensively using batch sorption experiments (Bostick et al., 2002; Van Loon et al., 2005; Fuller et al., 2015; Muuri et al., 2016). Loomer et al. (2013a) studied the sorption of Cs^+ in Queenston shale using a radiography technique and found an average CEC and $\log K_{Cs+/Na+}$ of 8.4 meq/100 g and 1.5, respectively. In comparison, the average CEC found here (1.8 ± 0.7 meq/100g; Table 3.3) is unexpectedly over four times lower, but the average $\log K_{Cs+/Na+}$ (2.3 ± 0.2; Table 3.3) is similar although slightly higher to that found by Loomer et al. (2013a).

Table 3.5. Compilation of ϕ_w , ϕ_I , ϕ_I/ϕ_w and $D_{p\text{-}I}$ values reported in the literature

	ϕ_w	ϕ_I	ϕ_I/ϕ_w (%)	$D_{p\text{-}I}$ (m^2/s)
Vilks et al. (2007)	0.066±0.005	0.034±0.011	51±17	$3.5\pm0.5\times10^{-11}$
Loomer et al. (2013a)	(0.109)	0.072-0.078 (0.076)	(70)	2.6×10^{-11} - 4.5×10^{-11} (3.8×10^{-11})
Nunn et al. (2018)	0.101-0.103	0.054-0.059	53-58	4.8×10^{-11}-5.8×10^{-11}
Xiang et al. (2013)	0.058-0.109 (0.085)	0.044-0.06 (0.051)	53-83 (61)	2.2×10^{-11} - 5.7×10^{-11} (4.0×10^{-11})
Cavé et al. (2009) (Radiography)	(0.062)	(0.06)	(97)	2.0×10^{-11} - 9.0×10^{-11} (4.8×10^{-11})
Cavé et al. (2009 (Through-diffusion)	(0.062)	0.023-0.049 (0.035)	(56)	2.1×10^{-11} - 8.2×10^{-11} (4.6×10^{-11})
This Study	0.101-0.126 (0.11)	0.106-0.114 (0.109)	(99)	5.7×10^{-11} - 6.5×10^{-11} (6.1×10^{-11})

*Values reported as average ± 1 σ or min-max (average)

3.5. Conclusion

A customized EDXRF technique that can be used for non-destructive diffusion studies was developed to monitor the evolution of tracer-concentration profiles in intact low-permeability geologic media. One of the advantages of this method is that it can be used to estimate diffusion coefficients and obtain in-situ estimates of ion-exchange properties for multiple tracers simultaneously. The sensitivity of EDXRF to detect low tracer concentrations is also good compared to other non-destructive techniques such as X-ray radiography, allowing for tracer concentrations that are more relevant to DGR conditions. The technique was tested by applying it in a dual-tracer (I and Cs) diffusion experiment with the Queenston Formation shale (borehole DGR4, Bruce nuclear site, Ontario, Canada). The method produced coherent I and Cs concentration profiles through the transient stage of diffusion and allowed for the successful

estimation of a $D_{p\text{-}I}$ of 6.1 ± 0.4 × 10^{-11} m^2/s and $D_{p\text{-}Cs}$ of 9.5 ± 1.3 × 10^{-11} m^2/s as well as a CEC of 1.8 ± 0.7 meq/100g and a $\log k_{Na\_Cs}$ of 2.3 ± 0.2 for the shale. The estimated values for D_p for both tracers and the $\log k_{Na\_Cs}$ are comparable to the range of values reported in literature for the Queenston Formation but the CEC estimate is lower than expected. Future work could expand the use of this technique to study different tracers, such as highly sorptive elements which diffuse slowly or low-atomic number tracers that are hard to detect with other X-ray techniques. Study of competitive ion-exchange of two or more reactive tracers simultaneously is also a potential application.

3.6. Acknowledgments

This research was supported by NWMO/NSERC Collaborative Research and Development Grant CRDPJ/ 477852-2014.

3.7. References

Agbogun, H. M. D., Hussein, E. M., & Al, T. A. (2013). Assessment of x-ray micro-CT measurements of porosity and solute concentration distributions during diffusion in porous geologic media. *Journal of Porous Media*, *16*(8). https://doi.org/10.1615/JPorMedia.v16.i8.10

Al, T. A., Clark, I. D., Kennell, L., Jensen, M., & Raven, K. G. (2015). Geochemical evolution and residence time of porewater in low-permeability rocks of the Michigan Basin, Southwest Ontario. *Chemical Geology*, *404*, 1-17. https://doi.org/10.1016/j.chemgeo.2015.03.005

Al, T., Xiang, Y., Cavé, L., & Loomer, D. (2010). *Measurement of diffusion properties by X-ray radiography and by through-diffusion techniques using iodide and tritium tracers: core samples from OS-1 and DGR-2*. In Technical report TR-07-17 Revision 3, May 2010. Prepared by University of New Brunswick for Intera Engineering Ltd.

Altman, S. J., Uchida, M., Tidwell, V. C., Boney, C. M., & Chambers, B. P. (2004). Use of X-ray absorption imaging to examine heterogeneous diffusion in fractured crystalline rocks. *Journal of contaminant hydrology*, *69*(1-2), 1-26. https://doi.org/10.1016/S0169-7722(03)00153-0

Barone, F. S., Rowe, R. K., & Quigley, R. M. (1990). Laboratory determination of chloride diffusion coefficient in an intact shale. *Canadian Geotechnical Journal*, *27*(2), 177-184. https://doi.org/10.1139/t90-021

Bea Jofré, S. A., Mayer, K. U., & MacQuarrie, K. T. B. (2011). *Modelling Reactive Transport in Sedimentary Rock Environments-Phase II MIN3P code enhancements and illustrative simulations for a glaciation scenario*. Nuclear Waste Management Organization (NWMO). Technical report NWMO TR-2011-13. Available at <www.nwmo.ca>.

Beauheim, R.L., Roberts, R.M., Avis, J.D., 2014. Hydraulic testing of low-permeability Silurian and Ordovician strata, Michigan Basin, southwestern Ontario. J. Hydrol. 509, 163–178. https://doi.org/10.1016/j.jhydrol.2013.11.033

Blum, P. (1997). Physical properties handbook: a guide to the shipboard measurement of physical properties of deep-sea cores. ODP Tech Note 26

Bostick, B. C., Vairavamurthy, M. A., Karthikeyan, K. G., & Chorover, J. (2002). Cesium adsorption on clay minerals: An EXAFS spectroscopic investigation. *Environmental Science & Technology*, *36*(12), 2670-2676. https://doi.org/10.1021/es0156892

Boving, T. B., & Grathwohl, P. (2001). Tracer diffusion coefficients in sedimentary rocks: correlation to porosity and hydraulic conductivity. *Journal of Contaminant Hydrology*, *53*(1-2), 85-100. https://doi.org/10.1016/S0169-7722(01)00138-3

Bradbury, M. H., & Baeyens, B. (2000). A generalised sorption model for the concentration dependent uptake of caesium by argillaceous rocks. *Journal of Contaminant Hydrology*, *42*(2-4), 141-163. https://doi.org/10.1016/S0169-7722(99)00094-7

Brennan, S. T., & Lowenstein, T. K. (2002). The major-ion composition of Silurian seawater. *Geochimica et Cosmochimica Acta*, *66*(15), 2683-2700. https://doi.org/10.1016/S0016-7037(02)00870-0

Cavé, L., Al, T., Xiang, Y., & Vilks, P. (2009). A technique for estimating one-dimensional diffusion coefficients in low-permeability sedimentary rock using X-ray radiography: Comparison with through-diffusion measurements. *Journal of contaminant hydrology*, *103*(1-2), 1-12. https://doi.org/10.1016/j.jconhyd.2008.08.001

Clark, I. D., Al, T., Jensen, M., Kennell, L., Mazurek, M., Mohapatra, R., & Raven, K. G. (2013). Paleozoic-aged brine and authigenic helium preserved in an Ordovician shale aquiclude. *Geology*, *41*(9), 951-954. https://doi.org/10.1130/G34372.1

Descostes, M., Blin, V., Bazer-Bachi, F., Meier, P., Grenut, B., Radwan, J., ... & Tevissen, E. (2008). Diffusion of anionic species in callovo-oxfordian argillites and oxfordian limestones (Meuse/Haute–Marne, France). *Applied Geochemistry*, *23*(4), 655-677. https://doi.org/10.1016/j.apgeochem.2007.11.003

Doherty, J., 2010. Open-source model-independent parameter estimation and uncertainty analysis software – PEST. Version 12.2. Available at <http://www.pesthomepage.org/>.

Emerson, D.W. (1990). Notes on mass properties of rocks – density, porosity, permeability. *Exploration Geophysics*, *21*, 209-216. https://doi.org/10.1071/EG990209

Fuller, A. J., Shaw, S., Ward, M. B., Haigh, S. J., Mosselmans, J. F. W., Peacock, C. L., ... & Burke, I. T. (2015). Caesium incorporation and retention in illite interlayers. *Applied Clay Science*, *108*, 128-134. https://doi.org/10.1016/j.clay.2015.02.008

Henrion, P. N., Monsecour, M., Fonteyne, A., Put, M., & De Regge, P. (1985). Migration of radionuclides in Boom Clay. *Radioact. Waste Manage. Nucl. Fuel Cycle*, *6*(3-4), 313-359.

Intera, 2011. *Descriptive geosphere site model*. Intera Engineering Ltd. report for the Nuclear Waste Management Organization (NWMO). Technical report NWMO DGR-TR-2011-24 R000. Available at <www.nwmo.ca>.

Jackson, R., 2009. *Organic Geochemistry and Clay Mineralogy of DGR-3 and DGR-4 Core*, Revision 0. TR-08-29. Report prepared for Intera Engineering Ltd., November, 2009. Available at <www.nwmo.ca>.

Jakob, A., Pfingsten, W., & Van Loon, L. (2009). Effects of sorption competition on caesium diffusion through compacted argillaceous rock. *Geochimica et Cosmochimica Acta*, *73*(9), 2441-2456. https://doi.org/10.1016/j.gca.2009.01.028

Koroleva, M., de Haller, A., Mäder, U., Waber, H.N., and Mazurek, M. (2009). *Borehole DGR-2: Pore-water investigations*. Rock-Water Interaction (RWI), Institute of Geological Sciences, University of Bern, Switzerland, Technical report TR-08-02.

Muuri, E., Ikonen, J., Matara-Aho, M., Lindberg, A., Holgersson, S., Voutilainen, M., Siitari-Kauppi, M., Martin, A., (2016). Behavior of Cs in Grimsel granodiorite: sorption on main minerals and crushed rock. *Radiochimica Acta*, *104*(8), 575-582. https://doi.org/10.1515/ract-2016-2574

Loomer, D. B., Scott, L., Al, T. A., Mayer, K. U., & Bea, S. (2013). Diffusion–reaction studies in low permeability shale using X-ray radiography with cesium. *Applied geochemistry*, *39*, 49-58. https://doi.org/10.1016/j.apgeochem.2013.09.019

Loomer, D., Xiang, Y., & Al, T. (2013). *Investigations of Methods for Quantifying Diffusive Transport Processes in Sedimentary Rock*. Nuclear Waste Management Organization (NWMO).Technical report NWMO TR-2013-18. Available at <www.nwmo.ca>.

Lowenstein, T. K., Hardie, L. A., Timofeeff, M. N., & Demicco, R. V. (2003). Secular variation in seawater chemistry and the origin of calcium chloride basinal brines. *Geology*, *31*(10), 857-860. https://doi.org/10.1130/G19728R.1

Mayer, K. U., Frind, E. O., & Blowes, D. W. (2002). Multicomponent reactive transport modeling in variably saturated porous media using a generalized formulation for kinetically controlled reactions. *Water Resources Research*, *38*(9), 13-1. https://doi.org/10.1029/2001WR000862

Melkior, T., Mourzagh, D., Yahiaoui, S., Thoby, D., Alberto, J. C., Brouard, C., & Michau, N. (2004). Diffusion of an alkaline fluid through clayey barriers and its effect on the diffusion properties of some chemical species. *Applied Clay Science*, *26*(1-4), 99-107. https://doi.org/10.1016/j.clay.2003.10.006

Nakashima, Y. (2000). The use of X-ray CT to measure diffusion coefficients of heavy ions in water-saturated porous media. *Engineering Geology*, *56*(1-2), 11-17. https://doi.org/10.1016/S0013-7952(99)00130-1

Nunn, J. A., Xiang, Y., & Al, T. A. (2018). Investigation of partial water saturation effects on diffusion in shale. *Applied Geochemistry*, *97*, 93-101. https://doi.org/10.1016/j.apgeochem.2018.08.004

Parkhurst, D.L., and Appelo, C.A.J., 2013, Description of input and examples for PHREEQC version 3—A computer program for speciation, batch-reaction, one-dimensional transport, and inverse geochemical calculations: U.S. Geological Survey Techniques and Methods, book 6, chap. A43, 497 p., available only at http://pubs.usgs.gov/tm/06/a43/

Poinssot, C., Baeyens, B., & Bradbury, M. H. (1999). Experimental and modelling studies of caesium sorption on illite. *Geochimica et cosmochimica Acta*, *63*(19-20), 3217-3227. https://doi.org/10.1016/S0016-7037(99)00246-X

Rançon, D. (1988). Comparative study of radioactive iodine behavior in soils under various experimental and natural conditions. *Radiochimica Acta*, *44*(1), 187-194. https://doi.org/10.1524/ract.1988.4445.1.187

Shackelford, C. D. (1991). Laboratory diffusion testing for waste disposal—A review. *Journal of Contaminant Hydrology*, *7*(3), 177-217. https://doi.org/10.1016/0169-7722(91)90028-Y

Truesdale, V. W. (2007). On the feasibility of some photochemical reactions of iodide in seawater. *Marine Chemistry*, *104*(3-4), 266-281. https://doi.org/10.1016/j.marchem.2006.12.003

Van Loon, L. R., Baeyens, B., & Bradbury, M. H. (2005). Diffusion and retention of sodium and strontium in Opalinus clay: Comparison of sorption data from diffusion and batch sorption measurements, and geochemical calculations. *Applied Geochemistry*, *20*(12), 2351-2363. https://doi.org/10.1016/j.apgeochem.2005.08.008

Van Loon, L. R., Soler, J. M., & Bradbury, M. H. (2003). Diffusion of HTO, 36Cl− and 125I− in Opalinus Clay samples from Mont Terri: Effect of confining pressure. *Journal of Contaminant Hydrology*, *61*(1-4), 73-83. https://doi.org/10.1016/S0169-7722(02)00114-6

Vilks, P. Miller, N. H. (2007). *Evaluation of Experimental Protocols for Characterizing Diffusion in Sedimentary Rocks.* Nuclear Waste Management Organization (NWMO). Technical report NWMO-TR-2007-11. Available at <www.nwmo.ca>.

Wersin, P., Van Loon, L. R., Soler, J. M., Yllera, A., Eikenberg, J., Gimmi, T., ... & Boisson, J. Y. (2004). Long-term diffusion experiment at Mont Terri: first results from field and laboratory data. *Applied Clay Science*, *26*(1-4), 123-135. https://doi.org/10.1016/j.clay.2003.09.007

Xiang, Y., Al, T., & Mazurek, M. (2016). Effect of confining pressure on diffusion coefficients in clay-rich, low-permeability sedimentary rocks. *Journal of contaminant hydrology*, *195*, 1-10. https://doi.org/10.1016/j.jconhyd.2016.10.004

Xiang, Y., Al, T., Scott, L., & Loomer, D. (2013). Diffusive anisotropy in low-permeability Ordovician sedimentary rocks from the Michigan Basin in southwest Ontario. *Journal of contaminant hydrology*, *155*, 31-45. https://doi.org/10.1016/j.jconhyd.2013.09.002

CHAPTER 4

CONCLUSION

In recent decades, proposals for long-term storage of nuclear waste into geological formations have sparked interest in solute migration through low-permeability materials. Diffusion and ion-exchange are key mechanisms that govern transport through rocks in which porewater is immobile, but there are challenges associated with studying these processes efficiently and accurately with existing methods at the laboratory scale.

The purpose of this research was to develop non-destructive, laboratory-based techniques to study diffusion and ion-exchange in low-permeability rocks of relevance to deep geological repositories (DGR). One of the objectives was to modify an existing radiography technique to study the diffusion of iodide in a low-porosity, heterogeneous granite and compare the results to more traditional through-diffusion (TD) measurements. The other study was focused on developing a new energy-dispersive X-ray fluorescence (EDXRF) technique that can be used in diffusion and ion-exchange experiments with a multi-element (I and Cs) tracer solution.

The X-ray radiography technique (Cavé et al., 2009) was modified to include rotation of the cylindrical samples on the vertical axis during image acquisition, providing horizontally integrated images that eliminate the need for horizontal registration and reduce the error associated with difference imaging. This modification allowed for the measurement of diffusion in heterogenous rocks, which would otherwise be challenging to study with the radiography techniques due to the complexity of image registration. The modified technique was tested by applying it in an iodide diffusion experiment with the Lac du Bonnet granite (Manitoba, Canada). The method produced coherent iodide concentration profiles through the transient stage of diffusion and allowed for the successful estimation of am effective diffusion coefficient (D_e)

of 3.1×10^{-14} m^2/s. This radiography estimate is 64 % lower than the average D_e obtained form TD measurements (8.7×10^{-14} m^2/s) on a different rock with similar mineralogical and textural characteristics. This difference in D_e values is relatively small compared to the range of values reported in the literature for similar rock types, thus lending confidence to the X-ray radiography method and its application for estimating diffusion in low-porosity crystalline rocks.

A customized EDXRF technique that can be used for non-destructive diffusion studies was developed to monitor the evolution of tracer-concentration in intact low-permeability geologic media. One of the advantages of this method is that it can be used to estimate diffusion coefficients and obtain in-situ estimates of ion-exchange properties for multiple tracers simultaneously. The sensitivity of EDXRF to detect low tracer concentrations is also good compared to other non-destructive techniques such as X-ray radiography, allowing for tracer concentrations that are more relevant to DGR conditions. The technique was tested by applying it in a dual-tracer (I and Cs) diffusion experiment with the Queenston Formation shale (borehole DGR4, Bruce nuclear site, Ontario, Canada). The method produced coherent I and Cs concentration profiles through the transient stage of diffusion and allowed for the successful estimation of a $D_{p\text{-}I}$ of $6.1 \pm 0.4 \times 10^{-11}$ m^2/s and $D_{p\text{-}Cs}$ of $9.5 \pm 1.3 \times 10^{-11}$ m^2/s as well as a cation exchange capacity (CEC) of 1.8 ± 0.7 and a selectivity coefficient ($\log k_{Na\_Cs}$) of 2.3 ± 0.2 for the shale. The estimated values for D_p for both tracers and the $\log k_{Na\_Cs}$ are comparable to the range of values reported in literature for the Queenston Formation but the CEC estimate is lower than expected.

Future studies could aim at expanding the use of the modified radiography method to study the diffusion of other tracers in heterogeneous rocks or low-porosity materials. The use of this method to study ion-exchange with reactive tracers is also promising, but additional work

remains to be done with regards to data calibration and parameter independence, as shown in Appendix B. Additionally, future work could expand the use of the EDXRF technique to study highly reactive elements which diffuse slowly, or low-atomic number tracers that are hard to detect with other X-ray techniques. Study of competitive ion-exchange of two or more reactive tracers simultaneously is also a potential application. This technique is also promising for other non-destructive analysis applications, including production of high-resolution elemental concentration profiles in large samples such as mine tailings cores.

4.1. References

Cavé, L., Al, T., Xiang, Y., & Vilks, P. (2009). A technique for estimating one-dimensional diffusion coefficients in low-permeability sedimentary rock using X-ray radiography: Comparison with through-diffusion measurements. *Journal of contaminant hydrology*, *103*(1-2), 1-12. https://doi.org/10.1016/j.jconhyd.2008.08.001

APPENDIX A

X-RAY RADIOGRAPHY DATA PROCESSING

A.1. Introduction

In X-ray radiography, raw data consist of grayscale images (16 bit, 1024x1024 pixels). The gray scale value (GSV) of each pixel is proportional to the intensity of X-rays (I) received at the detector. The grayscale images were analyzed in ImageJ (Rasband, 2018) using the method described by Cavé et al. (2009). This section provides details on the processing steps for the radiography data presented in Chapter 2.

A.2. Data processing

Data processing was done in multiple steps using ImageJ software to process the images and extract the data from the regions of interest (ROI) shown in Fig. A1, and Excel for the analysis of the extracted data.

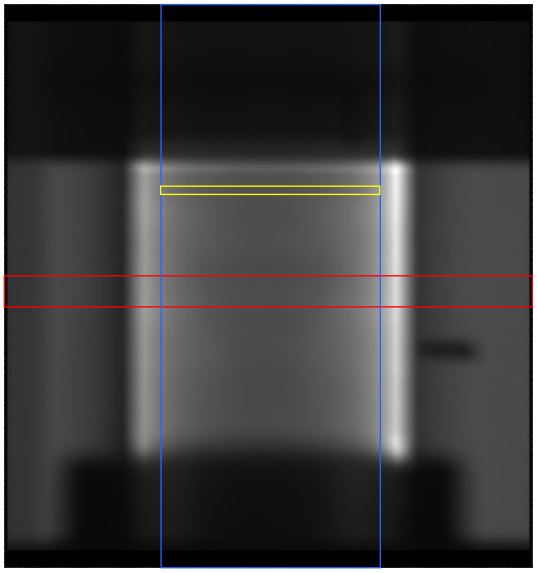

Fig. A1. Approximate location of the three regions of interest used for data processing on an example radiograph.

The first step in processing the data is to identify the middle of the sample on the horizontal axis, which is used as a reference point in the next step. It is assumed that rotation of the sample during acquisition eliminates heterogeneity horizontally and that diffusion of tracer in the sample is one-dimensional. Based on these assumptions, the only factor that causes horizontal variation in X-ray intensity in the sample area is the thickness of the sample. The longest path length, and thus lowest X-ray intensity, is in the middle of the sample because of its cylindrical shape. The average of each pixel columns in the red ROI (Fig. A1) was used to identify the pixel corresponding to the middle of the sample by locating the minimum GSV value of the profile in the sample area, ignoring local minima that result from noise.

To trace a vertical GSV profile along the diffusion path, the middle of the blue ROI (Fig. A1) was aligned with middle of the sample identified previously. The average of each pixel row in the ROI was then used to trace a GSV profile representing the X-ray intensity along the diffusion path (Fig. A2). A profile was traced for the reference radiograph and each timeseries radiographs based on data from three images.

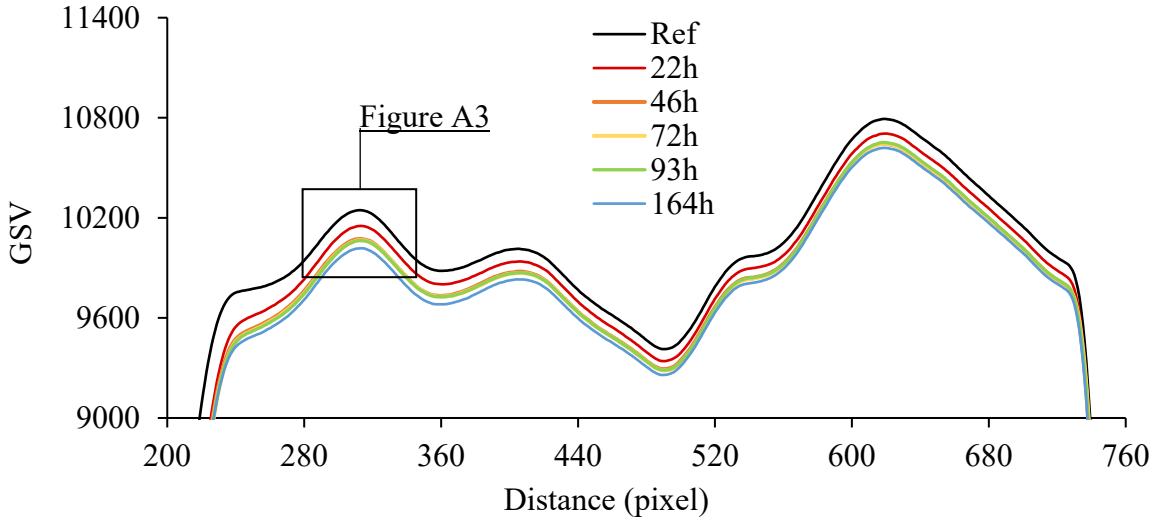

Fig. A2. Radiograph GSV profile (average from 3 radiographs) along the diffusion path at 5 times following iodide diffusion in sample CS2 and at time t = 0 (Ref).

Small variations in measured X-ray intensity between images are caused by changes in external conditions such as source and detector temperature, current intensity received from the power grid and time elapsed since the last detector calibration. To control for these unpredictable variations which can mask the signal from the tracer, the data should be normalised. It was found that comparing the intensity of X-rays between the reference and timeseries images in an area of the sample that is not impacted by diffusion (upper part of the sample) worked best to normalise the data. The yellow ROI (Fig. A1) shows the approximate location of the area used for normalisation. The ROI was placed in a zone where there is a peak in GSV caused by sample heterogeneity (Fig. A3). The average of each pixel row in the ROI was used to calculate a normalisation factor (N_f) for each timeseries radiograph using the maximum value of the vertical GSV profile in the ROI in the timeseries (Max_{ts}) and the reference (Max_{ref}) radiographs (Eq. A1). The GSV profiles from step 2 were then multiplied by the N_f.

$$N_f = \frac{ln(Max_{ref})}{ln(Max_{ts})} \quad [A1]$$

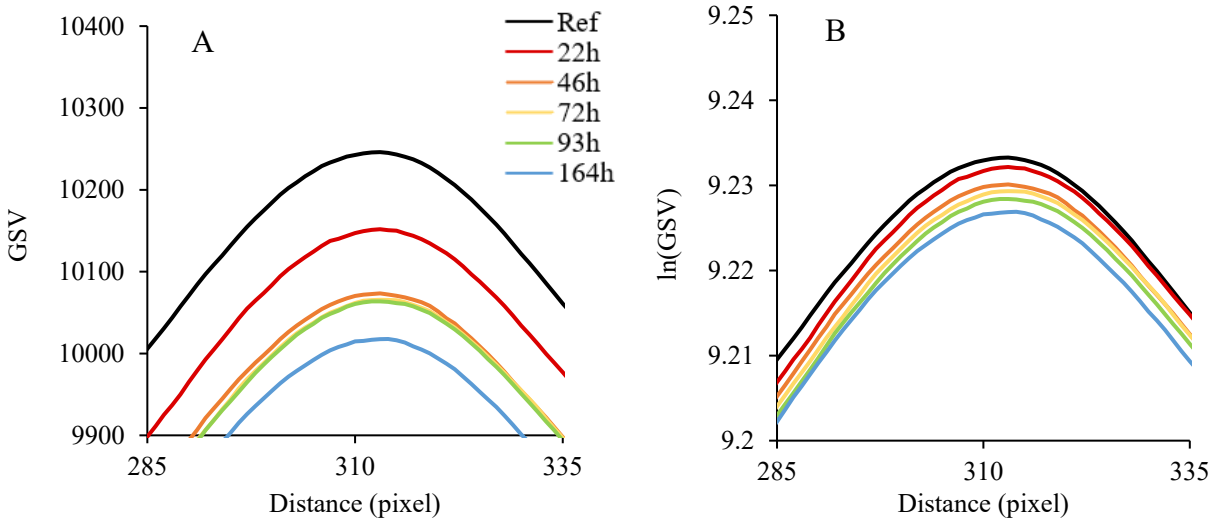

Fig. A3. X-ray intensity (GSV) peak located in normalisation ROI [A] before normalisation and [B] after normalisation and log transformation.

The change in X-ray attenuation (Δμ) was calculated by subtracting the normalised log-transformed GSV profile of each timeseries radiograph from the reference profiles. These profiles are proportional to the concentration of tracer in the sample. The process by which a Δμ profile is obtained from the GSV profiles is illustrated in Fig. A4. The green profile represents the change in attenuation caused by the tracer and suggests that the tracer concentration decreases with distance in the sample. Scaling of the pixel axis to units of distance (m) was done as a last step based on the known length of the sample and by identifying the pixels corresponding to the bottom and top of the sample in the GSV profile (inflection points of the two sharp drops in GSV observed in Fig. A4).

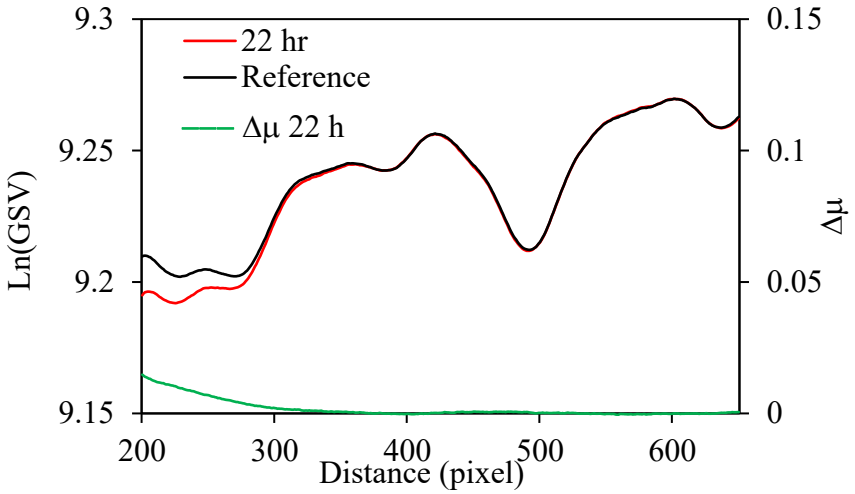

Fig. A4. Example illustrating how a Δμ profile (in green) is obtained by subtracting the X-ray intensity (ln(GSV)) profile of a time-series (here 22h, in red) from a reference profile (in black)

It was not possible to conduct a calibration that could accurately account for beam hardening in the sample (see Appendix B). Therefore, a least squares fitting approach with an analytical solution to Fick's second law (Chapter 2, Eq. 2.4) was used instead. The Δμ value corresponding to the position of the tracer influx boundary where $C/C_0 = 1$ ($\Delta\mu_0$) was calculated for each data point based on the change in attenuation at every distance x in the sample ($\Delta\mu_x$) and

the value of the best-fit modelled relative iodide concentration at the same distance x ($C_{m,x}/C_0$) using Eq. A2.1:

$$\frac{C_{m,x}}{C_0} = \frac{\Delta\mu_x}{\Delta\mu_0} \quad [A2]$$

so

$$\Delta\mu_0 = \frac{\Delta\mu_x \cdot C_0}{C_{m,x}} \quad [A2.1]$$

The $\Delta\mu_0$ calculated for each data point is shown in Fig. A5 for the 11-day time-series data. The $\Delta\mu_0$ is quite stable in the region after the first decrease close to the boundary and before the concentration gets too close to 0 (~0.011 m), owing to the good fit between the modelled curves and the measured diffusion profile.

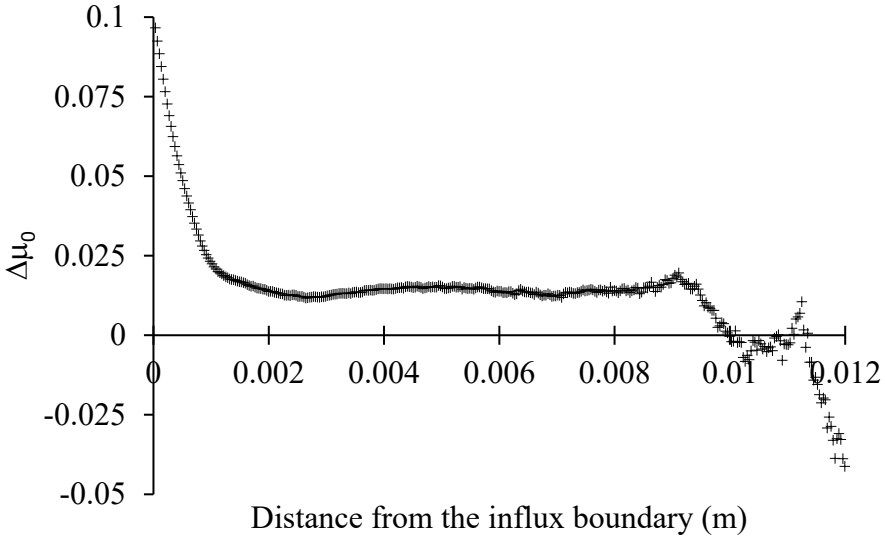

Fig. A5: Optimized $\Delta\mu_0$ across the bottom part of the sample domain

A single value for $\Delta\mu_0$ was determined for each time-series dataset by calculating the average $\Delta\mu_0$ in the distance interval in which the concentration was above 0 and the data were

not impacted by blurring (0.002 – 0.011 m in the 11-day time-series dataset example). Relative tracer concentrations in the sample (C_x/C_0) corresponding to each $\Delta\mu_x$ were then determined based on the optimized $\Delta\mu_0$ value (Eq. A3) in order to trace the diffusion profiles in relative concentration units shown in Chapter 2.

$$\frac{C_x}{C_0} = \frac{\Delta\mu_x}{\Delta\mu_0} \quad [A3]$$

A.3. References

Cavé, L., Al, T., Xiang, Y., & Vilks, P. (2009). A technique for estimating one-dimensional diffusion coefficients in low-permeability sedimentary rock using X-ray radiography: Comparison with through-diffusion measurements. *Journal of contaminant hydrology*, *103*(1-2), 1-12. https://doi.org/10.1016/j.jconhyd.2008.08.001

Rasband, W.S., 2018. ImageJ, U. S. National Institutes of Health, Bethesda, Maryland, USA, Available online at <https://imagej.net>.

APPENDIX B

STUDY OF DIFFUSION AND ION-EXCHANGE OF CESIUM IN GRANITE USING THE X-RAY RADIOGRAPHY METHOD

Abstract

Deep geological repositories for radioactive waste disposal are key for the long-term viability of nuclear energy. Granites are of interest because they provide a low-permeability and low-diffusivity barrier against solute migration via advection and diffusion. They also provide sorption capacity, although the in-situ sorption capacity of granitic rocks is not well characterized. A modified X-ray radiography method used to study diffusion of iodide in granite weas presented in Chapter 2. Here, an attempt to use this method to study diffusion and sorption of a reactive tracer, Cs, is presented. Two different calibration methods were tests, one using a cup filled with a silica sand matrix and tracer solutions and another using pressed pellet made up of crushed granite and tracer salts. Results show that the first method produces plausible diffusion profiles for Cs but not for I, and that the second method yields calibration curves that do not have a null intercept for an unknown reason. Therefore, more work is needed before the modified radiography technique can be used with reactive tracers in heterogeneous material.

B.1. Introduction

Diffusion in crystalline rocks has been studied using HTO and anionic tracers with the through-diffusion technique (Skagius & Neretnieks 1986; Vilks et al., 2003) but laboratory-based data on cation diffusion in intact crystalline rocks is relatively sparse. Experiments with cations are possible (Ruiyuan et al., 1997) but typically need to be conducted on samples that are extremely thin (Yamaguchi et al., 1992; Okuyama et al., 2007 & 2008) to avoid experimental durations longer than one year (Park & Baik, 2009). Some studies have used electrodes to

accelerate cation diffusion in a technique called electromigration (André et al., 2008 & 2009; Puukko et al., 2018; Li et al., 2020) while others have used more established out- and in-diffusion methods, as mentioned above (Waber et al., 2011; Johansson et al., 1998; Lee et al., 2012; Widestrand et al., 2007; Muuri et al., 2018), which can also last several years.

The study of ion-exchange properties of intact crystalline rocks is also challenging, yet crucial to evaluate retardation potential of reactive solutes. The most common methods to study ion-exchange are for disaggregated or unconsolidated rocks. Batch sorption experiments in which samples are mixed with tracer solutions and the adsorbed mass of reactive solutes is measured are typical of studies done on clays (Bradbury & Beayens, 2000; Poinssot et al., 1999; Bostick et al., 2002; Fuller et al., 2015; Muuri et al., 2016). For crystalline rocks, batch sorption experiments are often used to validate or compare the results of column experiments (Maes et al., 2008; Lee et al., 2012; Wu et al., 2015) or intact rock sorption studies using in-diffusion with autoradiography (Widestrand et al., 2007; Muuri et al., 2017; Johansson et al., 1998), electromigration (André et al., 2008 & 2009; Jukka et al., 2019) or through-diffusion (Lee et al., 2012; Wu et al., 2015; Fujikawa et al., 1993).

The fast and non-destructive nature of X-ray-based techniques, as well as their high spatial and temporal resolution makes them advantageous in studying the behaviour of tracers in porous media, particularly during the transient stage of diffusion (Tidwell & Glass, 1994; Nakashima, 2000). X-ray radiography has been used previously to study conservative tracer diffusion in shale (Cavé et al., 2009). Loomer et al. (2013) adapted this method to study diffusion and sorption of non-conservative tracer cesium in shale with the use of a calibration and multi-component reactive transport modelling.

[See Chapter 2, section 1.1, for theoretical principles of the X-ray radiography method]

This study also aims to provide an in-situ measurement of ion-exchange properties and the diffusion coefficient of a reactive tracer (Cs) in intact granite using the modified X-ray radiography method demonstrated in Chapter 2.

B.2. Methods

B.2.1. Sample description

[See Chapter 2, section 2.1, for sample description]

B.2.2. Sample preparation and characterization

[See Chapter 2, section 2.2, for sample preparation and characterization]

B.2.3. Synthetic porewater and tracer solutions

A synthetic porewater (SPW) designed to represent saline water in rocks of the Canadian Shield was used to saturate the samples. The cesium tracer solution was derived from the SPW matrix, replacing NaCl in the SPW with a higher CsCl concentration (1 mol/kgw) (Table B1).

Table B1. Composition of synthetic porewater and cesium tracer solution (mmol/kgw).

Ions	SPW	Cs tracer
Cs	0	1000
Na	147.5	0
Ca	100	100
Mg	2.5	2.50
K	0.57	0.57
Cl	341.27	1193.77
SO4	5.9	5.9

B.2.4. Water-accessible porosity measurement

[See Chapter 2, section 2.4, for porosity measurement details]

B.2.5. Diffusion cell design

[See Chapter 2, section 2.5, for diffusion cell design]

B.2.6. Data acquisition

[See Chapter 2, section 2.6, for experimental set-up and data acquisition parameters and processing details]

B.2.7. Calibration

The Δμ profiles were converted into Cs relative concentration (C/C_0) profiles through a calibration. When calibrating X-ray radiography data, systematic errors caused by differences in X-ray beam hardening between the standards and the samples need to be avoided or accounted for. Loomer et al. (2013) did that empirically by calibrating with standard solutions in three different materials of varying attenuation coefficients. Here, we propose two different calibration methods that account for beam hardening effects by using (1) standard tracer solutions in a plastic cup containing a silica sand matrix and (2) tracer salts held into a pressed pellet made from a crushed granite matrix.

The non-adsorbing matrix used for the first calibration consists of coarse silica sand packed into a cylindrical sleeve and held between two pieces of Porex®, a porous polyethylene material that allows for replacement of the standards without disturbing the silica sand matrix. The calibration cell is illustrated in Figure B1. The standard solutions used consist of diluted SPW with dissolved CsCl with concentrations ranging from 0 to 13 mmol/kg H_2O. These concentrations, lower than those of the tracer solutions, were chosen to account for the increased volume of solution in the X-ray path compared to the samples due to the higher porosity (33%) and bigger diameter (26 mm) of the calibration matrix. The corresponding tracer concentration in the diffusion

samples (C_t) was calculated with Equation B1 by applying correction factors to account for the porosity and diameter differences between the standards and the rock samples:

$$c_t = c_{pw} \cdot \frac{d_s}{d_r} \cdot \frac{\phi_s}{\phi_r} \quad \text{(B1)}$$

Where d_s and d_r are the diameters of the standards and the samples, respectively, and ϕ_s and ϕ_r are the porosities of the standards and the samples, respectively.

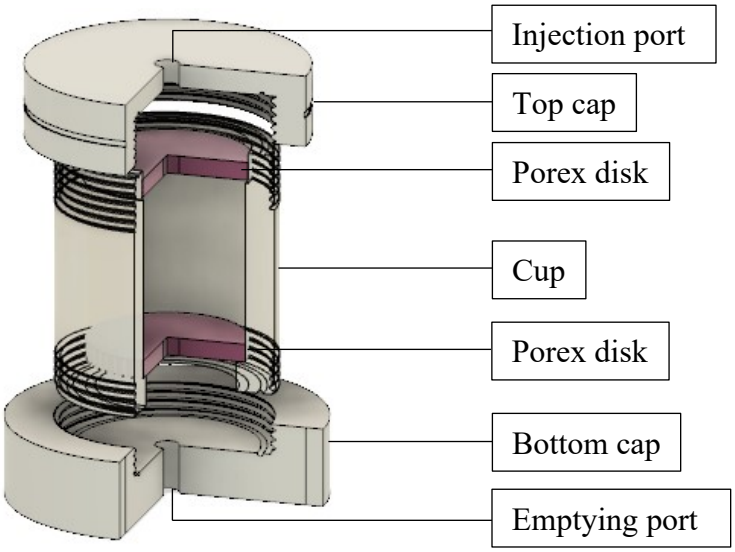

Fig. B1. Cross-section of the "cup" calibration cell

For the second calibration method, the standards were prepared using a conventional pressed-pellet approach that is described in Chapter 3, section 2.5 for XRF calibration. Lac du Bonnet granite was crushed and dried in the oven at 105 °C before being pulverized in a ball mill. Salt containing the diffusion tracers Cs (CsCl) was mixed quantitatively with pulverized granite, paraffin binder was added (10% w/w) and then compacted into solid pellets using a 25-tonne hydraulic press to make standards of variable, known concentrations. The standards were analyzed using the same instrument parameters and geometry used for the diffusion experiment described in Chapter 2, section 2.6, to produce calibration curves relating change in attenuation ($\Delta\mu$) to porewater equivalent tracer concentration (C_{pw}) in the standards, which can be calculated

with the same equations detailed in Chapter 3, section 2.8. The density correction factor ($\frac{\rho_r}{\rho_s}$) is not required for radiography because the difference in linear attenuation (μ) is accounted for with the porosity correction factor ($\frac{\phi_s}{\phi_r}$) alone to derive the corresponding tracer concentration in the intact diffusion samples (C_t) (Eq. B2):

$$C_t = C_{pw} \cdot \frac{\phi_s}{\phi_r} \quad \text{(B2)}$$

The multicomponent reactive transport code MIN3P (Mayer et al., 2002; Bea et al., 2011) was used to simulate the coupled processes of Cs diffusion and ion exchange following the method described by Loomer et al. (2013). Briefly, the parameter estimation code, PEST v.17 (Doherty, 2010) was used to iteratively change the reactive transport code's parameters to obtain the best fit between simulated and experimental Cs concentrations, as described in Chapter 3, section 2.9.

B.3. Results and discussion

B.3.1. Water-accessible porosity

[See Chapter 2, section 3.1, for porosity results]

B.3.2. Mineral characterization

[See Chapter 2, section 3.2, mineral characterization results]

B.3.3. Calibration

Calibration curves relating difference in attenuation (Δμ) to C_{pw} (A) and C_t (B) in the standards and samples, respectively are shown in Fig. B2 for the cup calibration method, and Figure B3 for the pellet calibration method. The calibration data yield very good linear

regression fit (R^2 = 99.84%) for the cup method, although the intercept is slightly higher than 0. The linear regression fit for the pellet calibration is also good (99.56%), however, the intercept is significantly higher than 0 despite the blank pellet being made using the same material and method as the Cs standards.

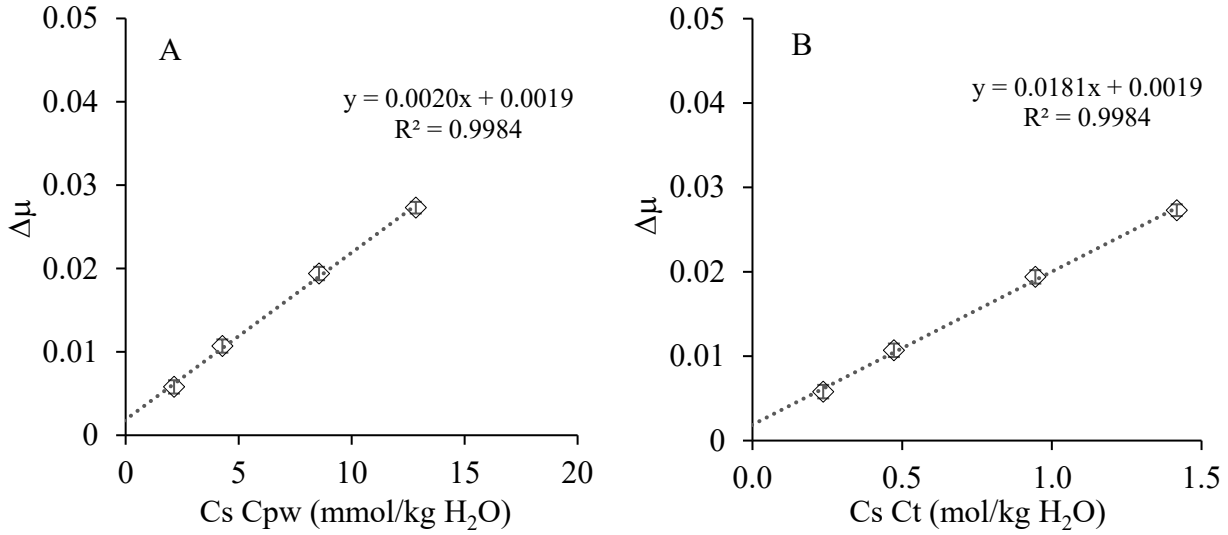

Fig. B2. Calibration with the cup method relating difference in attenuation (Δμ) to [A] Cs C_{pw} in the standards and [B] Cs C_t in the samples. Values are averages (n=3) ± 1 S.D. error bars.

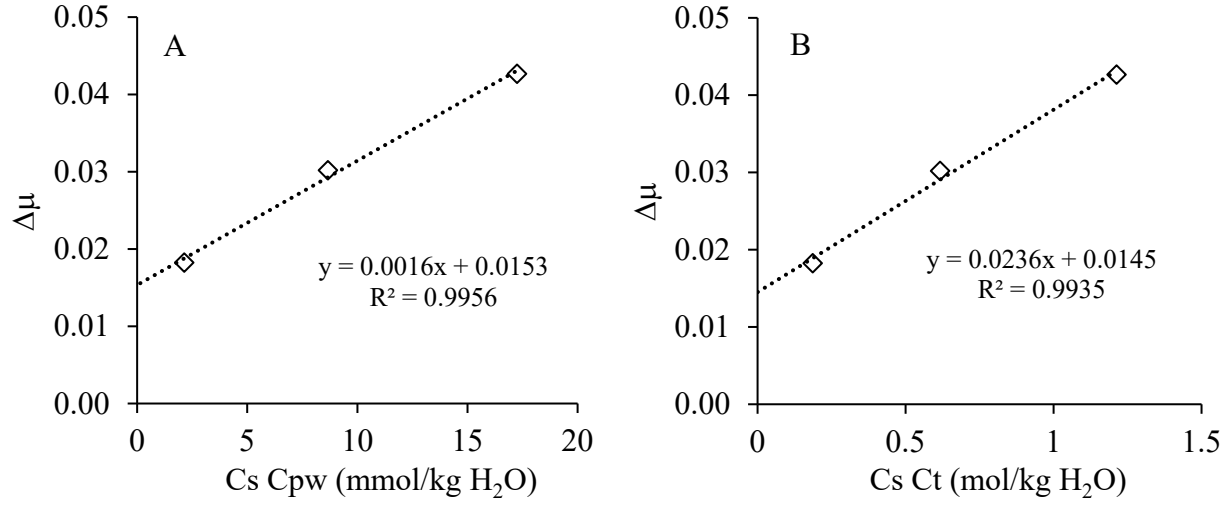

Fig. B3. Calibration with the pellet method relating difference in attenuation (Δμ) to [A] Cs C_{pw} in the standards and [B] Cs C_t in the samples.

To assess the validity of the cup calibration method, an iodide calibration was also performed the same way so that the results could be compared to the those from the fitting method described in Chapter 2, section 2.6. The iodide calibration curves relating difference in attenuation ($\Delta\mu$) to C_{pw} (A) and C_t (B) in the standards and samples, respectively, using the cup calibration method are shown in Fig. B4. The calibration data yield very good linear regression fit (R^2 = 99.99%), however, the intercept is also higher than 0.

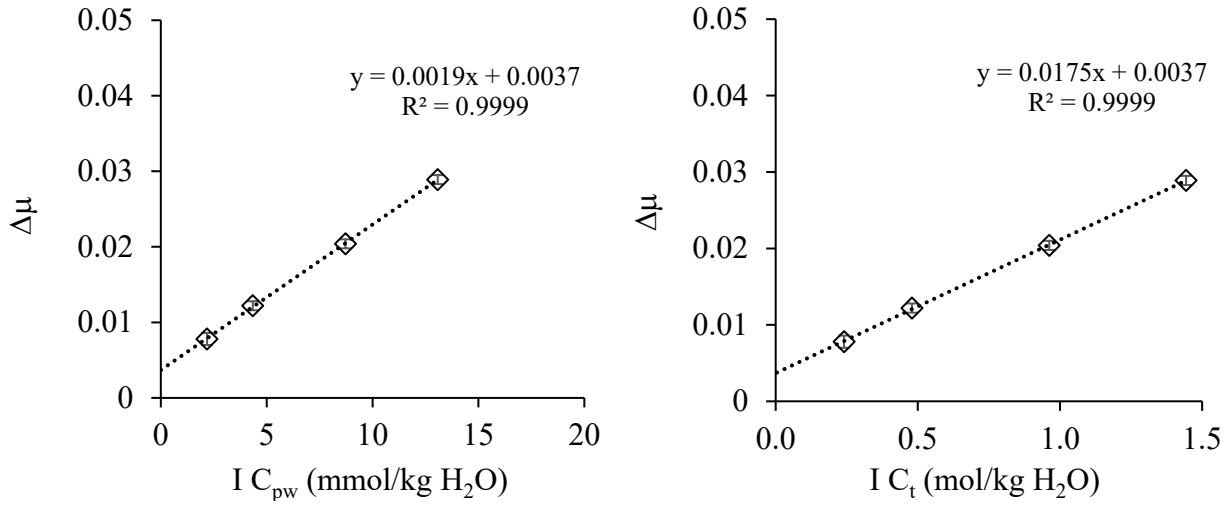

Fig. B4. Calibration with the cup method relating difference in attenuation ($\Delta\mu$) to [A] I C_{pw} in the standards and [B] I C_t in the samples. Values are averages (n=3) ± 1 S.D. error bars.

B.3.4. Cesium diffusion

X-ray radiographs of the granite sample were acquired during the transient phase of the diffusion experiment. Relative concentration profiles derived from the radiographs and the cup calibration curve are presented in Figure B5 for Cs, with the left side of the figure corresponding to the tracer-influx boundary which is in contact with the tracer solution. Data are not available for the first 2 mm of the sample domain because that region is affected by blurring due to the low spatial resolution of the X-ray beam. The dotted symbols represent the experimental relative Cs concentration data (C/C_0) at five different times after the start of the diffusion experiment. The solid lines represent the best-fit regression model from Fick's second law of diffusion for each of

the measurement times. The data generally reflect expectations for diffusive transport, but there are deviations from the model curves, especially in later acquisition times. The modelled value of C/C_0 at the influx boundary is higher than 1 (~1.2), indicating that there is likely some adsorption of Cs in the granite, despite the shape of the profiles not showing the characteristic inflexion point associated diffusion profiles of reactive tracers.

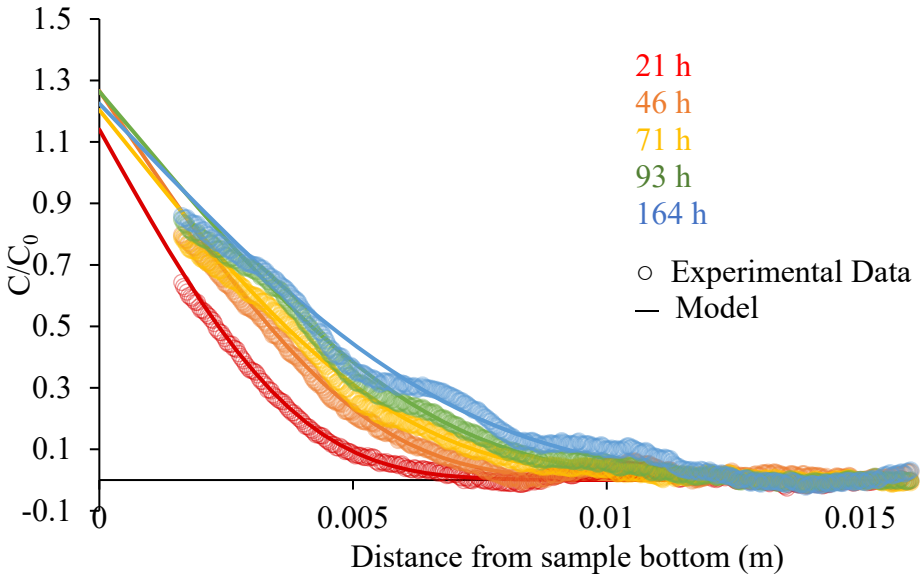

Fig. B5. Experimental (symbols) and modelled (lines) diffusion profiles for Cs at different measurement times after tracer injection based on the cup calibration.

The D_p values obtained by fitting the model to each time-series datasets individually are represented as a function of time (after the start of diffusion) in Fig. B6. A decrease and D_p and an increase in CEC through time are observed. The progression through time is indicative of how far the tracer has penetrated in the sample, suggesting that the cation exchange capacity is lower at the influx boundary compared to the inside of the sample, and that the diffusion (D_p) slows down as Cs migrates deeper in the sample.

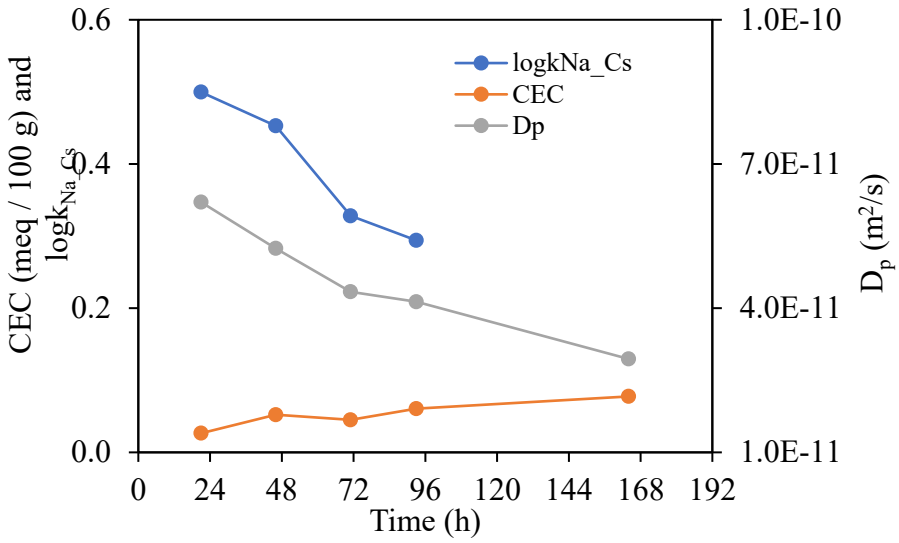

Fig. B6. Estimated parameters (D_p, CEC, $logk_{Na\_Cs}$) for Cs based on based-fit modelled diffusion profiles at different measurement times after tracer injection based on the cup calibration.

A summary of the estimates for the 3 parameters at different acquisition times is presented in Table B2. The average $D_{p\text{-}Cs}$ of 4.6 ± 1.2 $\times 10^{-11}$ $m^2 \cdot s^{-1}$ is higher than the estimated $D_{p\text{-}I}$ from Chapter 2 (2.4 ± 0.3 × 10^{-11} $m^2 \cdot s^{-1}$), which makes sense because the water-accessible porosity (ϕ_w) is generally also accessible to cations, whereas the anion-accessible porosity might be lower due to anion exclusion effects, impeding on diffusion. The estimated $D_{p\text{-}Cs}$ is comparable to that of HTO (3.96 ± 0.3 × 10^{-11} $m^2 \cdot s^{-1}$), which can also access the ϕ_w. The CEC value is quite low compared to clay rich rocks such as shales, indicating that ion-exchange in the granite is limited.

Table B2. Summary of estimated parameters (D_p, CEC, $logk_{Na\_Cs}$) for Cs based based on the cup calibration method.

	Dp	CEC	$logk_{Na\_Cs}$
21 h	6.2E-11	0.03	0.5
46 h	5.2E-11	0.05	0.5
71 h	4.3E-11	0.05	0.3
93 h	4.1E-11	0.06	0.3
164 h	2.9E-11	0.08	0.007*
Average ± 1σ	4.6 ± 1.2 E-11	0.05 ± 0.02	0.4 ± 0.1

*Anomalous value not included in the average and standard deviation calculations

Relative tracer concentration profiles derived from the radiographs and the pellet calibration curve regression equation are presented in Fig. B7 for Cs. These profiles also generally reflect expectations for diffusive transport, but the C/C_0 value throughout the profiles is lower than what the profiles from the cup calibration method show in Fig. B5, indicating that there would be less or no adsorption of cesium in the granite. A model was not fit to these data because the validity of the calibration curve is questionable due to the high intercept.

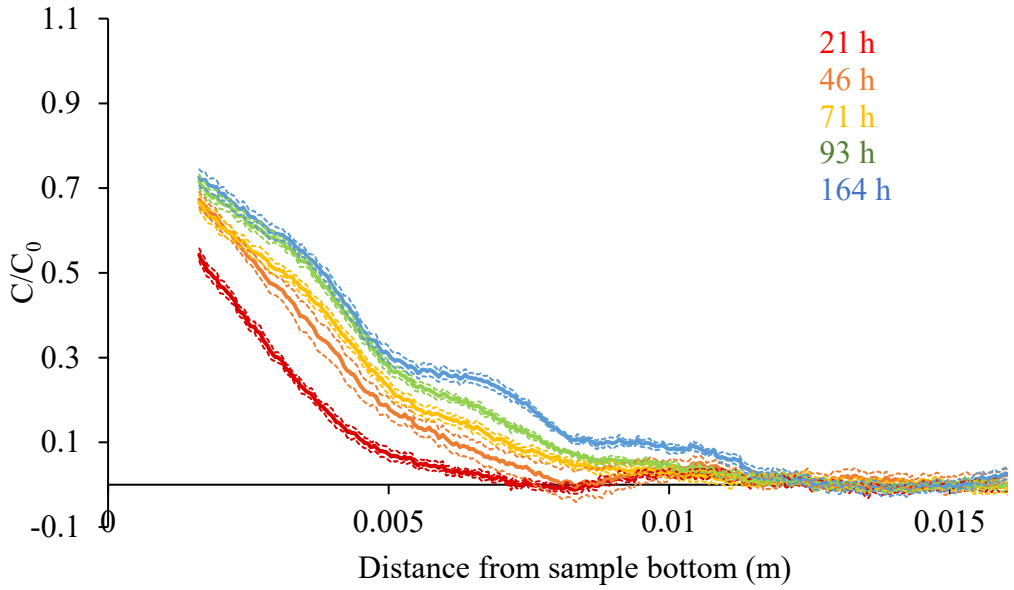

Fig. B7. Experimental diffusion profiles for Cs at different measurement times after tracer injection based on the pellet calibration. Profiles are an average (n=3) and dashed lines represent ± 1σ.

In order assess the validity of the cup calibration method, an iodide calibration was also performed so that the results could be compared to the those from the fitting method described in Chapter 2, section 2.6. Experimental diffusion profiles for I at different measurement times after tracer injection based on the cup calibration are shown in Fig. B8. The lines represent the best-fit modelled curves discussed in Chapter 2. The very poor fit between the data and the modelled curves indicate that the cup calibration method is not equivalent to the fitting method. The $C_x/C0$

value at the influx boundary should be close to 1 since it is in contact with the tracer reservoir. Data is missing at the influx boundary, but the experimental data close to the boundary (~2mm) indicates that it is unlikely that a relative concentration of 1 would be found at the boundary. Based on this, the validity of the cup calibration method is also questionable in this case.

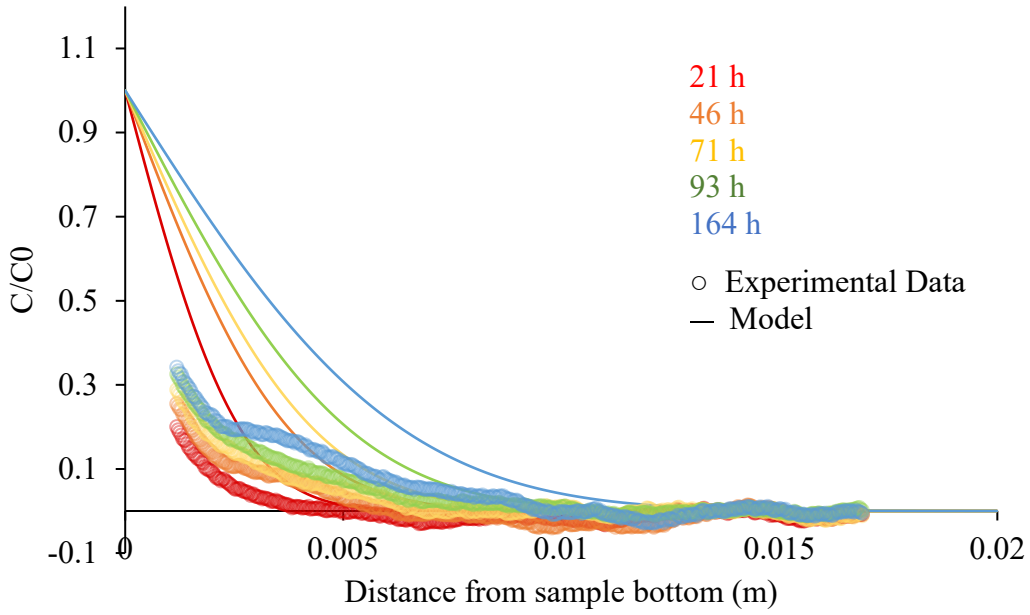

Fig. B8. Experimental diffusion profiles for I at different measurement times after tracer injection based on the cup calibration with previous best-fit modelled curves from Chapter 2.

B.4. Conclusion

The modified radiography method described in Chapter 2 was employed with a reactive tracer (Cs) with the objective of studying diffusion and ion-exchange in granite. Results from two different calibration methods show that the use of a plastic cup containing a non-sorbing silica sand and tracer solutions of different concentrations is promising. However, tests using iodide tracer show that the results obtained with the calibration do not fit well with an analytical solution to Fick's second law of diffusion. More work remains to be done to improve the

radiography data calibration method for reactive tracer diffusion in low-porosity, heterogenous material .

B.5. References

André, M., Malmström, M. E., & Neretnieks, I. (2009). Determination of sorption properties of intact rock samples: New methods based on electromigration. *Journal of contaminant hydrology*, *103*(3-4), 71-81. https://doi.org/10.1016/j.jconhyd.2008.09.006

André, M., Neretnieks, I., & Malmström, M. E. (2008). Measuring sorption coefficients and BET surface areas on intact drillcore and crushed granite samples. *Radiochimica Acta*, *96*(9-11), 673-677. https://doi.org/10.1524/ract.2008.1552

Bradbury, M. H., & Baeyens, B. (2000). A generalised sorption model for the concentration dependent uptake of caesium by argillaceous rocks. *Journal of Contaminant Hydrology*, *42*(2-4), 141-163. https://doi.org/10.1016/S0169-7722(99)00094-7

Bostick, B. C., Vairavamurthy, M. A., Karthikeyan, K. G., & Chorover, J. (2002). Cesium adsorption on clay minerals: An EXAFS spectroscopic investigation. *Environmental Science & Technology*, *36*(12), 2670-2676. https://doi.org/10.1021/es0156892

Cavé, L., Al, T., Xiang, Y., & Vilks, P. (2009). A technique for estimating one-dimensional diffusion coefficients in low-permeability sedimentary rock using X-ray radiography: Comparison with through-diffusion measurements. *Journal of contaminant hydrology*, *103*(1-2), 1-12. https://doi.org/10.1016/j.jconhyd.2008.08.001

Doherty, J., 2010. Open-source model-independent parameter estimation and uncertainty analysis software – PEST. Version 12.2. Available at < http://www.pesthomepage.org/>.

Fuller, A. J., Shaw, S., Ward, M. B., Haigh, S. J., Mosselmans, J. F. W., Peacock, C. L., ... & Burke, I. T. (2015). Caesium incorporation and retention in illite interlayers. *Applied Clay Science*, *108*, 128-134. https://doi.org/10.1016/j.clay.2015.02.008

Fujikawa, Y., Fukui, M., Drew, D. J., & Vandergraaf, T. T. (1993). Analysis of the migration of instantaneously injected cesium in artificial fractures of Lac du Bonnet granite, Manitoba, Canada. *Journal of contaminant hydrology*, *14*(3-4), 207-232. https://doi.org/10.1016/0169-7722(93)90025-N

Johansson, H., Siitari-Kauppi, M., Skålberg, M., & Tullborg, E. L. (1998). Diffusion pathways in crystalline rock—examples from Äspö-diorite and fine-grained granite. *Journal of Contaminant Hydrology*, *35*(1-3), 41-53. https://doi.org/10.1016/S0169-7722(98)00114-4

Lehto, J., Puukko, E., Lindberg, A., & Voutilainen, M. (2019). Batch sorption experiments of cesium and strontium on crushed rock and biotite for the estimation of distribution coefficients on intact crystalline rock. *Heliyon*, *5*(8). https://doi.org/10.1016/j.heliyon.2019.e02296

Lee, C. P., Wu, M. C., Tsai, T. L., Wei, H. J., Men, L. C., & Lin, T. Y. (2012). Comparative study on retardation behavior of Cs in crushed and intact rocks: two potential repository host rocks in the Taiwan area. *Journal of Radioanalytical and Nuclear Chemistry*, *293*(2), 579-586. https://doi.org/10.1007/s10967-012-1684-3

Li, X., Meng, S., Puhakka, E., Ikonen, J., Liu, L., & Siitari-Kauppi, M. (2020). A modification of the electromigration device and modelling methods for diffusion and sorption studies of radionuclides in intact crystalline rocks. *Journal of contaminant hydrology*, *231*, 103585. https://doi.org/10.1016/j.jconhyd.2019.103585

Loomer, D. B., Scott, L., Al, T. A., Mayer, K. U., & Bea, S. (2013). Diffusion–reaction studies in low permeability shale using X-ray radiography with cesium. *Applied geochemistry*, *39*, 49-58. https://doi.org/10.1016/j.apgeochem.2013.09.019

Muuri, E., Ikonen, J., Matara-Aho, M., Lindberg, A., Holgersson, S., Voutilainen, M., Siitari-Kauppi, M., Martin, A., (2016). Behavior of Cs in Grimsel granodiorite: sorption on main minerals and crushed rock. *Radiochimica Acta*, *104*(8), 575-582. https://doi.org/10.1515/ract-2016-2574

Muuri, E., Matara-aho, M., Puhakka, E., Ikonen, J., Martin, A., Koskinen, L., & Siitari-Kauppi, M. (2018). The sorption and diffusion of 133Ba in crushed and intact granitic rocks from the Olkiluoto and Grimsel in-situ test sites. *Applied Geochemistry*, *89*, 138-149. https://doi.org/10.1016/j.apgeochem.2017.12.004

Muuri, E., Siitari-Kauppi, M., Matara-aho, M., Ikonen, J., Lindberg, A., Qian, L., & Koskinen, L. (2017). Cesium sorption and diffusion on crystalline rock: Olkiluoto case study. *Journal of Radioanalytical and Nuclear Chemistry*, *311*, 439-446. https://doi.org/10.1007/s10967-016-5087-8

Nakashima, Y. (2000). The use of X-ray CT to measure diffusion coefficients of heavy ions in water-saturated porous media. *Engineering Geology*, *56*(1-2), 11-17. https://doi.org/10.1016/S0013-7952(99)00130-1

Okuyama, K., Sasahira, A., Noshita, K., & Ohe, T. (2008). A method for determining both diffusion and sorption coefficients of rock medium within a few days by adopting a micro-reactor technique. *Applied Geochemistry*, *23*(8), 2130-2136. https://doi.org/10.1016/j.apgeochem.2008.03.017

Okuyama, K., Sasahira, A., Noshita, K., Yoshida, T., Kato, K., Nagasaki, S., & Ohe, T. (2007). A fast and sensitive method for evaluating nuclides migration characteristics in rock medium by using micro-channel reactor concept. *Physics and Chemistry of the Earth, Parts A/B/C*, *32*(1-7), 463-468. https://doi.org/10.1016/j.pce.2005.12.007

Park, C. K., & Baik, M. H. (2009). Diffusion of some chemical species through a granite considering their geochemical properties. *Korean journal of chemical engineering*, *26*, 1279-1285. Diffusion of some chemical species through a granite considering their geochemical properties

Poinssot, C., Baeyens, B., & Bradbury, M. H. (1999). Experimental and modelling studies of caesium sorption on illite. *Geochimica et cosmochimica Acta*, *63*(19-20), 3217-3227. https://doi.org/10.1016/S0016-7037(99)00246-X

Puukko, E., Lehto, J., Lindberg, A., & Voutilainen, M. (2018). Electromigration experiments for studying transport parameters and sorption of cesium and strontium on intact crystalline rock. *Journal of contaminant hydrology*, *217*, 1-7. https://doi.org/10.1016/j.jconhyd.2018.08.010

Ruiyuan, W., Hongcheng, G., Xiangyun, W., & Yuanfang, L. (1997). Diffusion of fission fragment nuclides in granite. *Radiochimica Acta*, *76*(3), 137-142. https://doi.org/10.1524/ract.1997.76.3.137

Skagius, K., & Neretnieks, I. (1986). Porosities and diffusivities of some nonsorbing species in crystalline rocks. *Water Resources Research*, *22*(3), 389-398. https://doi.org/10.1029/WR022i003p00389

Tidwell, V. C., & Glass, R. J. (1994). X ray and visible light transmission for laboratory measurement of two-dimensional saturation fields in thin-slab systems. *Water Resources Research*, *30*(11), 2873-2882. https://doi.org/10.1029/94WR00953

Vilks, P., Cramer, J. J., Jensen, M., Miller, N. H., Miller, H. G., & Stanchell, F. W. (2003). In situ diffusion experiment in granite: phase I. *Journal of contaminant hydrology*, *61*(1-4), 191-202. https://doi.org/10.1016/S0169-7722(02)00135-3

Waber, H. N., Gimmi, T., & Smellie, J. A. T. (2011). Effects of drilling and stress release on transport properties and porewater chemistry of crystalline rocks. Journal of hydrology, 405(3-4), 316-332. https://doi.org/10.1016/j.jhydrol.2011.05.029

Widestrand, H., Byegård, J., Cvetkovic, V., Tullborg, E. L., Winberg, A., Andersson, P., & Siitari-Kauppi, M. (2007). Sorbing tracer experiments in a crystalline rock fracture at Äspö (Sweden): 1. Experimental setup and microscale characterization of retention properties. *Water Resources Research*, *43*(10). https://doi.org/10.1029/2006WR005277

Wu, M. C., Lee, C. P., Tsai, S. C., Liu, C. Y., Pan, C. H., Tsai, T. L., ... & Men, L. C. (2015). Study on sorption and diffusion of Sr in crushed and intact basalt and granite investigated in through-diffusion experiments. *Journal of Radioanalytical and Nuclear Chemistry*, *304*, 435-441. https://doi.org/10.1007/s10967-014-3889-0

Yamaguchi, T., Sakamoto, Y., & Senoo, M. (1993). Consideration on effective diffusivity of strontium in granite. *Journal of Nuclear Science and Technology*, *30*(8), 796-803. https://doi.org/10.1080/18811248.1993.9734550

APPENDIX C

EDXRF INSTRUMENT PARAMETER OPTIMISATION

C.1. Introduction

Energy dispersive X-ray fluorescence spectroscopy (EDXRF) is a technique that makes use of a semiconductor radiation detector to measure the number and energy of the fluorescence X-rays produced when photons from an X-ray beam interact with a sample. There are multitudes of parameters to consider when doing EDXRF, all of which can work together or against each other to affect the measurements. In the X-ray tube, a cathode is heated to generate electrons by thermionic emission, which are directed to a target anode, producing X-rays as they slow down in the target (Poludniowski et al., 2022). Increasing the electric potential difference (voltage) between the cathode and the anode increases the kinetic energy of the electrons, resulting in photons of higher maximum energy, whereas a higher current (more electrons) results in a higher X-ray beam intensity as more photons are being produced. The X-ray beam can be "hardened" by filtering with materials such as aluminium or copper to remove low-energy X-rays from the beam before it hits the samples. This can help reduce the total count of lower energy X-rays which are not of interest for the measurements, as well as decrease the background X-rays in the energy range of interest. Materials used in the sample preparation can also influence the measurements by interacting with the X-ray beam. In semi-conductor detectors, build up of electric charge is converted to a digital signal and counted to produce a spectrum of the total number of X-ray events recorded as a function of their energy. Characteristic X-ray energy peaks appear progressively above the background during the detection period based on the elemental composition of the target. Several factors can affect the detection stage of EDXRF measurements, such as signal collimation, acquisition time, rise-time discrimination and detector

dead time. The objective of this section is to determine the optimal parameters for EDXRF diffusion data acquisition for the method developed in Chapter 3.

C.2. Results and discussion

In order to evaluate the effect of the source voltage on the measurements, the acquisition time and the source current were kept constant (180 seconds, 25 mA, respectively), and the source voltage was increased between each acquisition. The change in peak intensity and relative error on the intensity as a function of voltage is presented in Figure C1 for Cs and I. The peak intensity increases sharply with an increase in the tube source voltage for both Cs and I, indicating that higher-energy X-rays interact more readily with these elements, resulting in more fluorescence emission. As the intensity of the peaks increase, a decrease in the relative error on the calculated peak intensity is observed, although it appears to slow down towards higher voltages, despite the peak intensities rising at the same rate. This phenomenon is better observed in Fig. C2, which shows the decline in relative error slowing down quickly as a function of X-ray intensity for Cs and I, indicating that the improvement in the X-ray intensity calculation has limitations that cannot be corrected solely by increasing the count rate. Therefore, although increasing the voltage is optimal to reduce error in the intensity calculation, the benefits become less significant at higher voltages.

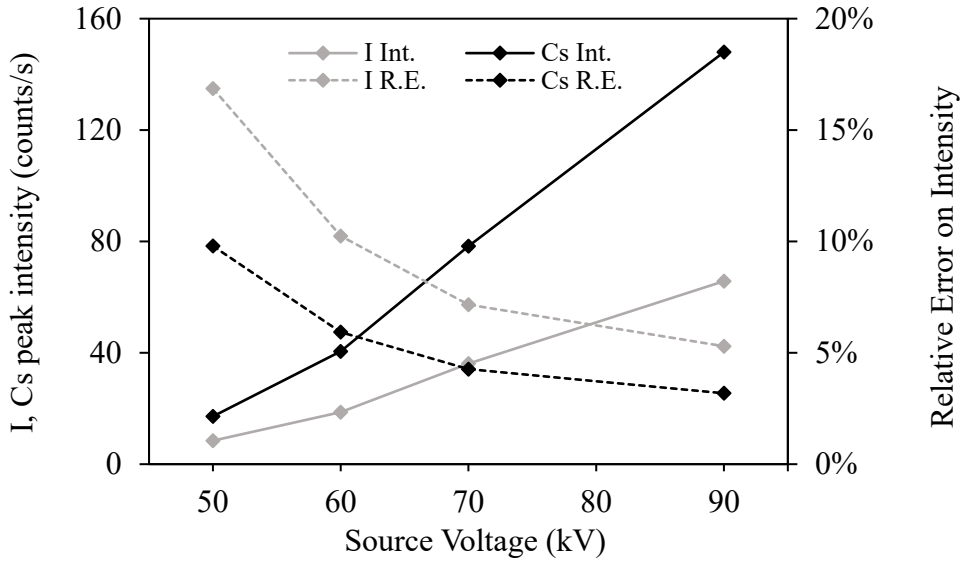

Fig. C1. Change in I-Kα and Cs-Kα peak intensity and relative error on the intensity with voltage.

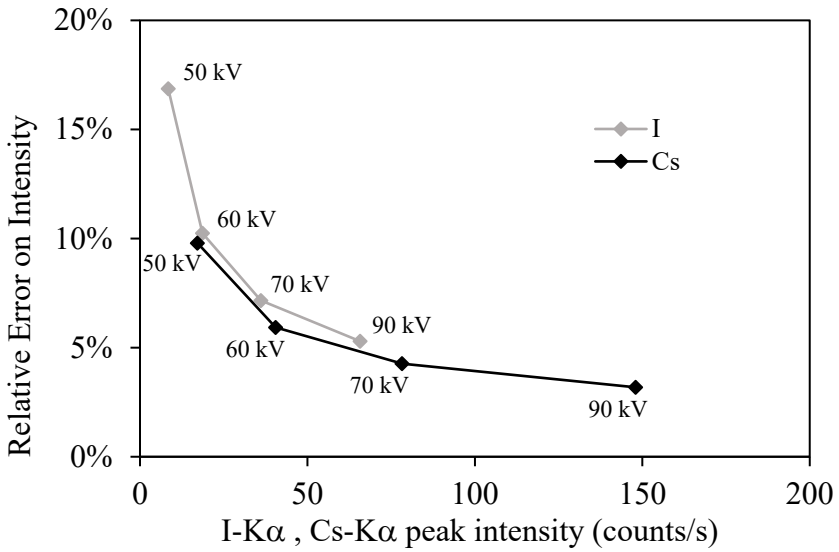

Fig. C2. Relative error on intensity as a function of peak intensity for Cs and I.

To evaluate the effect of the source current on the measurements, the acquisition time and the source voltage were kept constant (180 seconds, 80 kV, respectively), and the source voltage was increased between each acquisition. The change in X-ray intensity and relative error on the intensity as a function of current is presented in Fig. C3 for the Cs-Kα peak. Overall, the

increase in current results in an increase in X-ray intensity, which corresponds to a general decrease in the relative error on the intensity. The rise in X-ray intensity with current is somewhat maintained even at higher currents. However, the curve has an irregular shape and the effect on the relative error appears to stop somewhere between 25 mA and 27.5 mA.

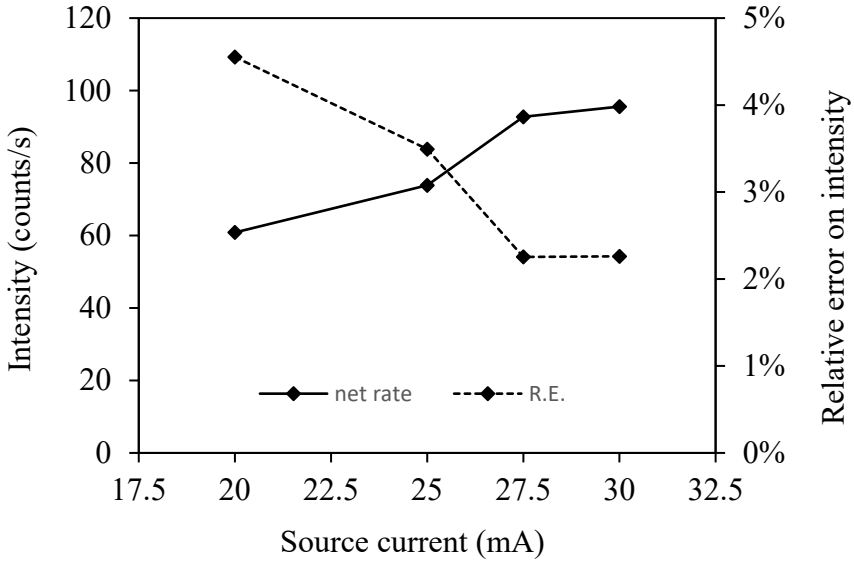

Fig. C3. Cs-Kα peak intensity and relative error on the intensity as a function of source current.

The power of the X-ray source can be calculated with Equation C1:

$$P = V * I \tag{C1}$$

Where P is the power (W), V is the voltage (V) and I is the current intensity (A). The power of the X-ray source used in this experimented is limited to 3000 W, and it was decided to keep the power usage at 80% (2400 W) to prevent overworking the generator. Therefore, a voltage of 80kV and a current of 30 mA (2400 W power) were picked as an optimal combination for the experiment based on the tests.

The acquisition time is another important parameter in X-ray detection. In order to evaluate the effect of the acquisition time on the measurements, the source voltage and current were maintained constant (80 kV, 25 mA, respectively) while the acquisition time was increased between each acquisition. The change in net peak area (background-subtracted peak area) and relative error on net count rate as a function of acquisition time is presented in Fig. C4 for the Cs-Kα peak. Because the detector works by counting the total number of photons reaching it over time, increasing the acquisition time results in larger peaks (high net area) in the spectra, and a relative error that decreases accordingly. Although increasing the acquisition time to 300 seconds or more appears to be ideal, a lower acquisition time of 180 seconds was decided to limit the total acquisition duration and allow the 3 samples (up to 30 slices each) to be analyzed in a single day.

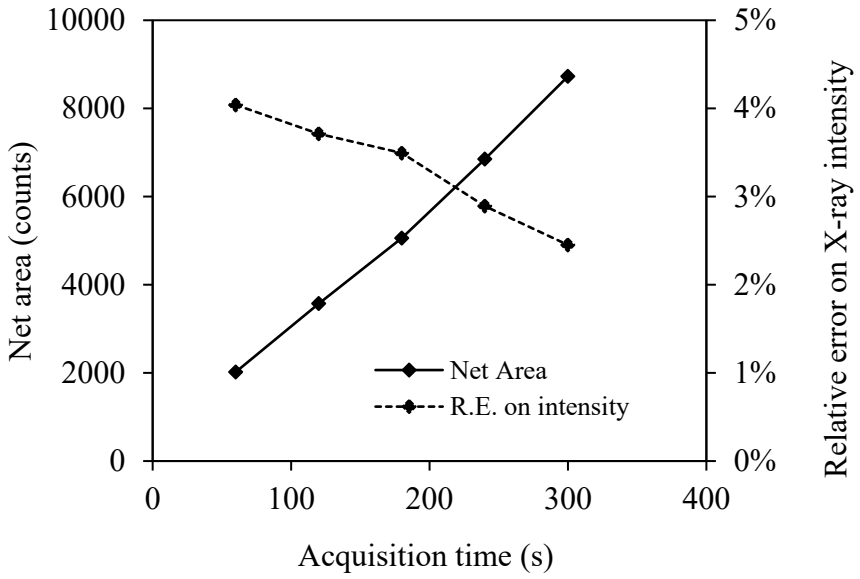

Fig. C4. Cs-Kα net peak area and relative error on intensity as a function of acquisition time.

The position of the X-ray source, detector and sample relative to each other has a very important effect on the signal produced and detected from the sample. An example of the geometry of the different components is shown in Figure (C5A). The relative position of the different components was optimized by trial and error to maximize the count rate. It was found that placing the source further from the sample and out of the field of view of the detector is necessary to prevent incident X-rays scattered from the filter from making their way into the detector. The geometry is optimal when the source and detector's axes cross each other on the edge of the sample, on a tangent that is perpendicular to the mid-line between the source and the detector's axes. This results in a take-off angle (from the sample to the detector) that is aligned with the detector's axis, maximizing the count rate (Fig. C5B). Extra collimation on the detector using a 25 mm^2 external multilayer collimator (eMLC2 from Amptek®) limits scattering inside of the detector by narrowing the angle at which X-rays can enter the detector's window.

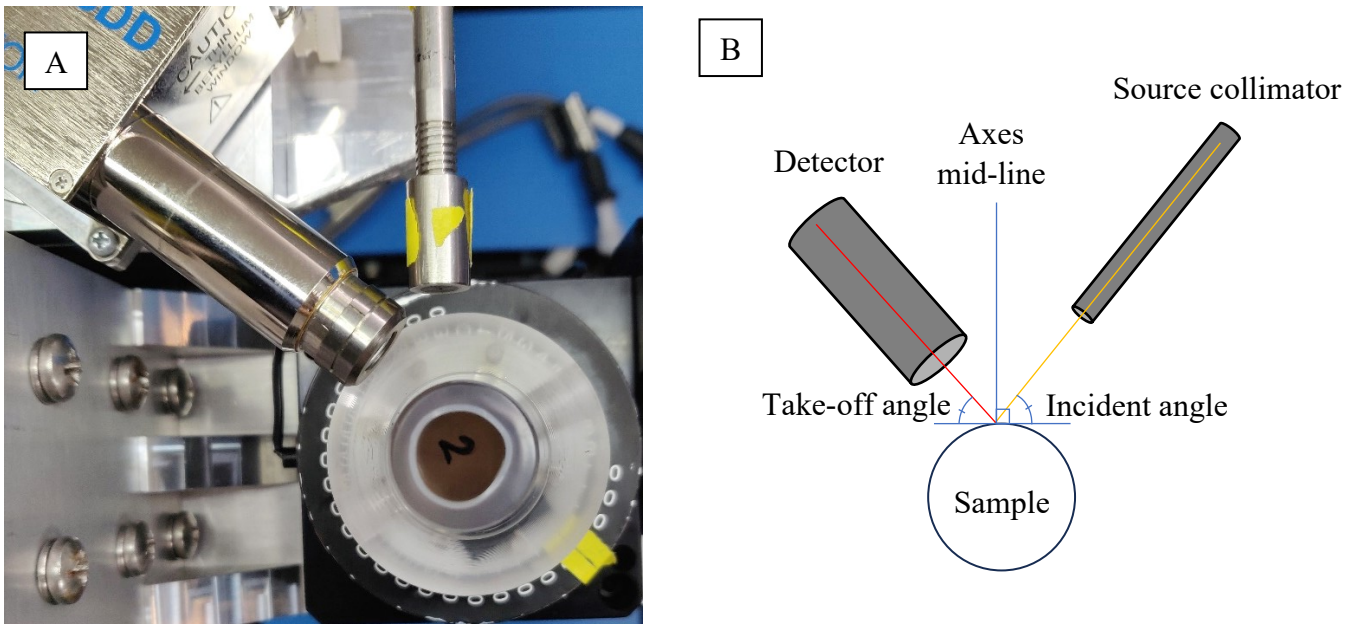

Fig. C5. [A] Real and [B] schematic view of the relative position of the sample, detector and collimator used in the XRF diffusion experiments.

The output of X-rays from the source is affected by its temperature. The stability of the source after an initial 10-minute warm-up (first 10 data points) was tested by acquiring data every 40 seconds for 73 minutes while keeping the source on. The repeated measurements of the total count of the Cs-Kα peak are shown in Fig. C6. Overall, the source stability after the warm-up period was found to be satisfactory, with a Cs-Ka peak area within a 5256 to 5630 counts range, with an average of 5442 ± 70 counts, corresponding to an RSD of 1.3%.

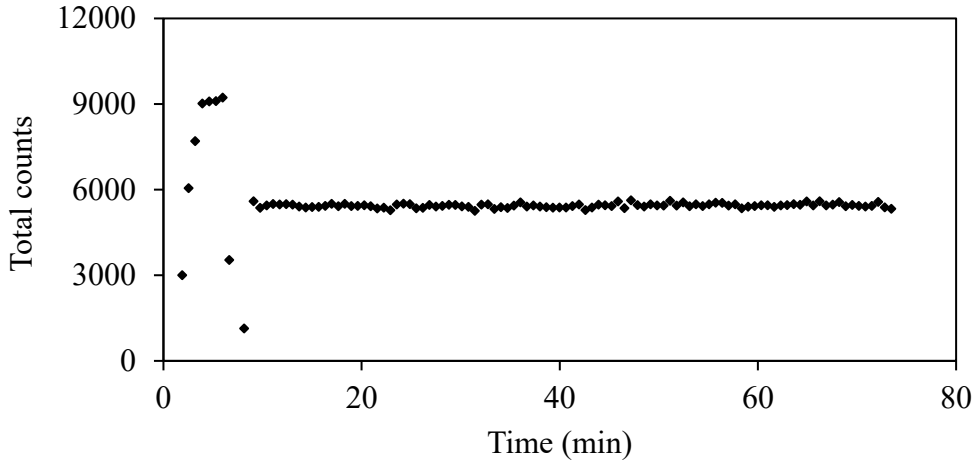

Fig. C6. Cs-Kα peak total count measured at 40-second intervals to evaluate source stability

Beam filtration is another important parameter to consider. Filtration of the incident beam with metals such as aluminum and copper reduces the intensity of the beam in the lower energy range. The overall X-ray count and background signal also decrease with filtration. Increasing the density or thickness of the filter material increases the filtration effect. Filtration at the signal processing step is also possible. Rise-time discrimination (RTD) is a digital pulse processing (DPP) step that filters out the X-ray events that have a slower peaking time in the detector. Because X-ray events that constitute the background signal typically have a slower peaking time, the implementation of an RTD step in the DPP reduces the background signal, which decreases the uncertainty of the calculated characteristic X-ray intensities. Figure C7 shows the comparison

between spectra acquired from the same standard sample while using two different Cu filter thicknesses, as well as with and without RTD. The 0.85 mm Cu filter reduces more of the background, but also decreases the characteristic X-ray peaks the most. The spectrum acquired with the 0.63 mm Cu filter and with RTD was found to be optimal, reducing some of the background while maintaining high characteristic X-ray peaks, thus minimizing the uncertainty.

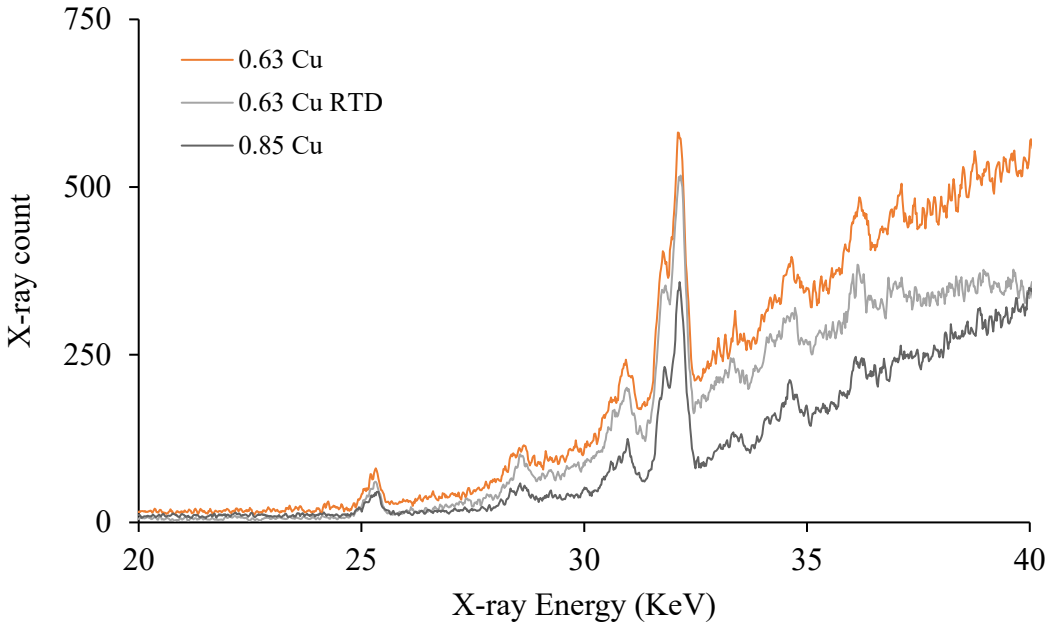

Fig. C7. Spectral data in the energy region encompassing the I-Kα and Cs-Kα peaks acquired while using different Cu filter thicknesses and signal processing methods (plotted as 3-point moving averages).

Beam collimation is an important parameter to consider because it defines the spatial resolution for the measurements and has an important effect on the total XRF induced in the sample from the beam. A 1 mm collimator and a 0.5 mm collimator were tested, and it was found that the 0.5 mm collimator reduced the total count by 75% compared to the 1 mm collimator, so the latter was used for experiments in order to maximize the signal. The effective spatial resolution (ESR) for the measurements with the 1 mm collimator was determined using

an edge response (ER) technique as outlined by Agbogun et al. (2013). The technique involves acquiring data in a line profile across the boundary of a sharp discontinuity. In this study, a copper (Cu) strip placed on the sample served as the contrasting material, and data were acquired every 25-100 vertical motor position units across the sample-copper boundary. The net area of the Cu-Kα peak as a function of vertical distance is shown in Fig. C9. The average net area of the first 3three points (positions -900 to -700, average count of 951) in the figure is considered the background value, and the last three points (positions 400 to 600, average count of 178284) is considered the maximum Cu-Kα peak net area. The slow initial rise (up to -75 position) is thought to be due to secondary X-rays from the rock interacting with the Cu even while the beam is fully within the rock. Most of the ER (92.8%) occurs between the -75 and 100 position (9974 to 174952 counts). The resolution of the motor position is 0.00635 mm / motor unit. Therefore, the ESR was found to be 1.1 mm, corresponding to an ER rise from 5.1% to 97.9% of the maximum Cu fluorescence signal.

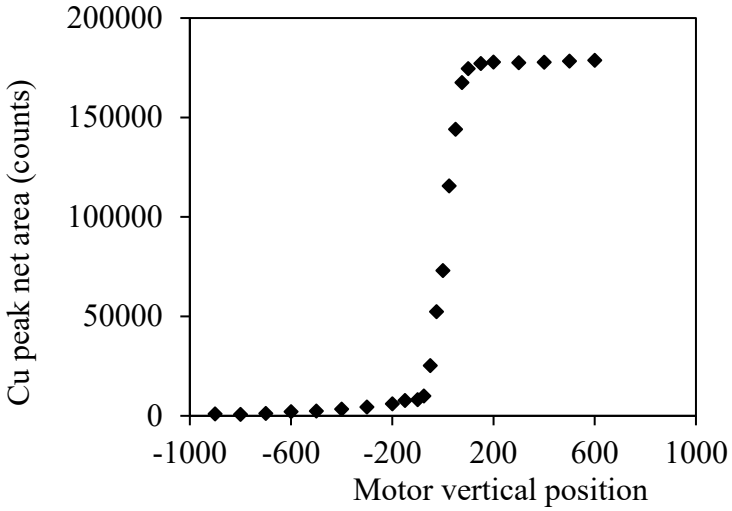

Fig. C8. Net area of Cu-kα peak across the edge of a strip of copper.

In order to identify the boundary between the sample and the stainless steel ring, data were acquired incrementally across the edge of the stainless steel ring. The intensity of the characteristic X-ray peak for Mo and Ba was determined at each point, and the position of the first data acquisition step for the diffusion experiments was selected as the location of the inflexion points of the Mo (present in the stainless steel) and Ba (present within the sample) peak intensity curves (Fig. C10).

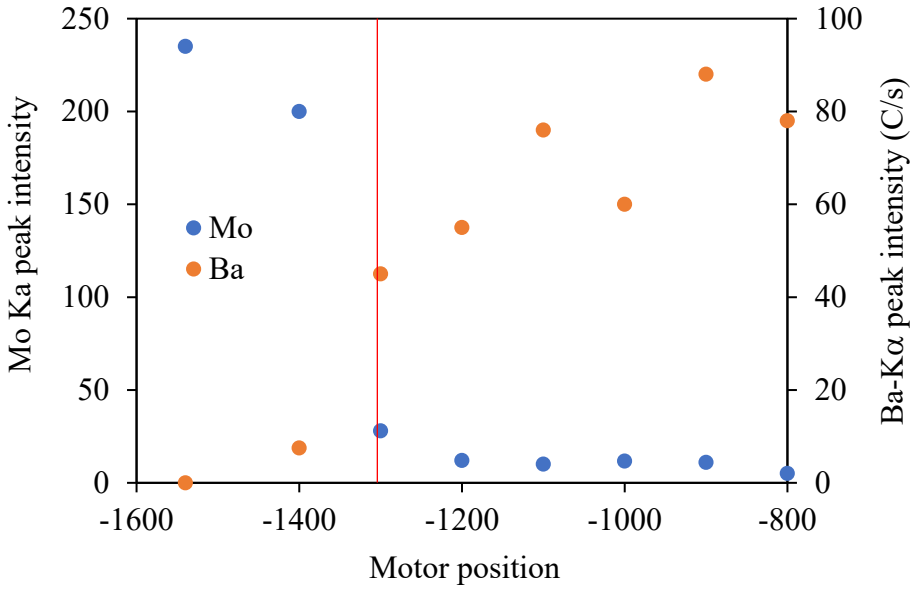

Fig. C9. Mo-Kα and Ba-Kα peak intensity across the edge of the stainless steel ring placed at the bottom of the sample. The chosen first step for diffusion data acquisition is indicated by the red bar.

Because the stainless steel was masking the influx boundary in some of the samples, the position of the first data acquisition step does not necessarily correspond with the sample bottom (x = 0). In order to determine the corresponding distance from the sample bottom (x) for each data acquisition step, the iodide tracer was assumed to display standard non-reactive diffusion behaviour in the samples, and a least squares fitting approach of an analytical solution to Fick's second law (Chapter 3, Eq. 3.9) to the iodide diffusion data was used, where the $D_{p\text{-}I}$ value and the x value were both optimized. An example is shown in Fig. C11 for QS2, for the 5-day

dataset, where the change in the sum of the square of the residuals ($\Sigma(e_i^2)$) as a function of the corresponding x value at step 1 (x_1) is shown for three different D_p values. It was found that there is a unique combination of D_p and x_1 values that results in a minimized $\Sigma(e_i^2)$ (the lowest parabola minimum in Fig. C11). A single value for x_1 was determined by calculating the average of the best fit x_1 values determined for individual time-series dataset.

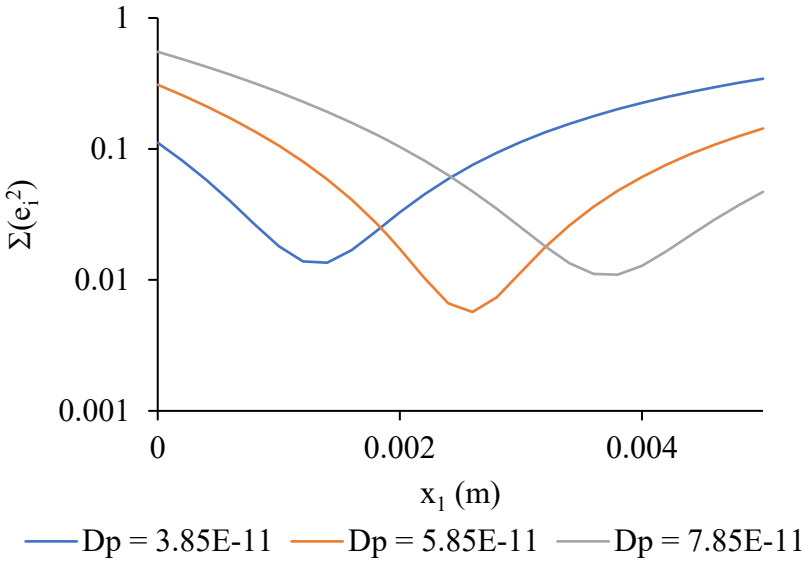

Fig. C10: Change in $\Sigma(e_i^2)$ as a function of x_1 value at three different D_p.

C.3. Conclusion

There are multitudes of parameters to consider when doing EDXRF analyses. The specific parameters listed for the method described in Chapter 3 were chosen based on the results from tests performed to optimize parameters such as source voltage and current, data acquisition time, relative position of the beam, detector and sample, beam and detector collimation, source warmup and filtration. The results from these tests showed that the following parameters were optimal for the diffusion experiments: source voltage and current of 80 kV and 30 mA,

respectively, acquisition time of 180 seconds per slice, 1 mm beam collimation, multi-layer collimation on the detector, beam filtration with 0.63 mm of Cu and a warm-up time of 10 minutes. These parameters should be tested, optimized and adjusted based on the specificities of different experiments.

C.4. References

Agbogun, H. M. D., Hussein, E. M., & Al, T. A. (2013). Assessment of x-ray micro-CT measurements of porosity and solute concentration distributions during diffusion in porous geologic media. *Journal of Porous Media*, *16*(8). https://doi.org/10.1615/JPorMedia.v16.i8.10

Poludniowski, G., Omar, A., & Andreo, P. (2022). *Calculating X-ray Tube Spectra: Analytical and Monte Carlo Approaches*. CRC Press. https://doi.org/10.1201/9781003058168